# Charged Currents, Color Dipoles, and $xF_3$ at Small $x$¶

## R. Fiore[a, b] and V. R. Zoller[c]

*[a] Dipartimento di Fisica, Universitá della Calabria, Rende, 87036 Italy*
*[b] Institute Nazionale di Fisica Nucleare, Gruppo collegato di Cosenza, Italy*
*[c] Institute for Theoretical and Experimental Physics, Moscow, 117218 Russia*
*e-mail: fiore@cs.infn.it, zoller@itep.ru*
Received August 18, 2005

We develop the light-cone color dipole description of highly asymmetric diffractive interactions of left-handed and right-handed electroweak bosons. We identify the origin and estimate the strength of the left–right asymmetry effect in terms of the light-cone wave functions. We report an evaluation of the small-$x$ neutrino–nucleon deep inelastic scattering structure functions $xF_3$ and $2xF_1$ and present a comparison with experimental data. © 2005 Pleiades Publishing, Inc.

PACS numbers: 12.15.Ji, 12.38.–t

At small Bjorken $x$, the driving term of the inclusive/diffractive excitation of charmed and (anti)strange quarks in the charged current (CC) neutrino deep inelastic scattering (DIS) is the $W^+$-gluon/pomeron fusion,

$$W^+ g \longrightarrow c\bar{s} \quad (1)$$

and

$$W^+ \mathbf{IP} \longrightarrow c\bar{s}. \quad (2)$$

Different aspects of the CC inclusive and diffractive DIS have been discussed in [1, 2].

In the color dipole approach [3, 4] (for the review, see [5]), the small-$x$ DIS is treated in terms of the interaction of the $c\bar{s}$ color dipole of size $\mathbf{r}$ with the target proton which is described by the beam- and flavor-independent color dipole cross section $\sigma(x, r)$. Once the light-cone wave function (LCWF) of a color dipole state is specified, the evaluation of observable quantities becomes a routine quantum mechanical procedure. In this communication, we extend the color dipole analysis to the CC DIS, with particular emphasis on the left–right asymmetry of diffractive interactions of electroweak bosons of different helicity. We derive the relevant LCWF and evaluate the structure functions $xF_3$, $\Delta xF_3$, and $2xF_1$. We focus on the vacuum-exchange-dominated leading $\log(1/x)$ region of $x \lesssim 0.01$.

At small $x$, the contribution of excitation of open charm/strangeness to the absorption cross section for scalar, ($\lambda = 0$), left-handed, ($\lambda = -1$), and right-handed,

($\lambda = +1$), $W$ boson of virtuality $Q^2$ is given by the color dipole factorization formula [6, 7]

$$\sigma_\lambda(x, Q^2) = \int dz d^2\mathbf{r} \sum_{\lambda_1, \lambda_2} \left| \Psi_\lambda^{\lambda_1, \lambda_2}(z, \mathbf{r}) \right|^2 \sigma(x, r). \quad (3)$$

In Eq. (3), $\Psi_\lambda^{\lambda_1, \lambda_2}(z, \mathbf{r})$ is the LCWF of the $|c\bar{s}\rangle$ state with the $c$ quark carrying fraction $z$ of the $W^+$ light-cone momentum and $\bar{s}$ with momentum fraction $1-z$. The $c$- and $\bar{s}$-quark helicities are $\lambda_1 = \pm 1/2$ and $\lambda_2 = \pm 1/2$, respectively. The $W^+ \longrightarrow c\bar{s}$-transition vertex is specified as follows:

$$g U_{cs} \bar{c} \gamma_\mu (1 - \gamma_5) s,$$

where $U_{cs}$ is an element of the CKM matrix and the weak charge $g$ is related to the Fermi coupling constant $G_F$,

$$G_F / \sqrt{2} = g^2 / m_W^2. \quad (4)$$

The polarization states of the $W$ boson carrying the laboratory frame four-momentum

$$q = (\nu, 0, 0, \sqrt{\nu^2 + Q^2}) \quad (5)$$

are described by the four-vectors $e_\lambda$,

$$e_0 = \frac{1}{Q}(\sqrt{\nu^2 + Q^2}, 0, 0, \nu),$$

$$e_\pm = \mp \frac{1}{\sqrt{2}}(0, 1, \mp i, 0), \quad (6)$$

with unit vectors $\mathbf{e}_x$ and $\mathbf{e}_y$ in the $q_x$ and $q_y$ directions, respectively. We find it convenient to use the basis of

---

¶ The text was submitted by the authors in English.

helicity spinors of [8]. Then, the vector ($V$) and axial-vector ($A$) components of the LCWF

$$\Psi_\lambda^{\lambda_1,\lambda_2}(z,\mathbf{r}) = V_\lambda^{\lambda_1,\lambda_2}(z,\mathbf{r}) - A_\lambda^{\lambda_1,\lambda_2}(z,\mathbf{r}), \qquad (7)$$

are as follows:

$$V_0^{\lambda_1,\lambda_2}(z,\mathbf{r}) = \frac{\sqrt{\alpha_W N_c}}{2\pi Q}\{\delta_{\lambda_1,-\lambda_2}[2Q^2 z(1-z)$$

$$+ (m-\mu)[(1-z)m - z\mu]]K_0(\varepsilon r) \qquad (8)$$

$$- i\delta_{\lambda_1,\lambda_2}(2\lambda_1)e^{-i2\lambda_1\phi}(m-\mu)\varepsilon K_1(\varepsilon r)\},$$

$$A_0^{\lambda_1,\lambda_2}(z,\mathbf{r}) = \frac{\sqrt{\alpha_W N_c}}{2\pi Q}\{\delta_{\lambda_1,-\lambda_2}(2\lambda_1)[2Q^2 z(1-z)$$

$$+ (m+\mu)[(1-z)m + z\mu]]K_0(\varepsilon r) \qquad (9)$$

$$+ i\delta_{\lambda_1,\lambda_2}e^{-i2\lambda_1\phi}(m+\mu)\varepsilon K_1(\varepsilon r)\}.$$

If $\lambda = \pm 1$,

$$V_\lambda^{\lambda_1,\lambda_2}(z,\mathbf{r}) = -\frac{\sqrt{2\alpha_W N_c}}{2\pi}$$

$$\times\{\delta_{\lambda_1,\lambda_2}\delta_{\lambda,2\lambda_1}[(1-z)m + z\mu]K_0(\varepsilon r) \qquad (10)$$

$$- i(2\lambda_1)\delta_{\lambda_1,-\lambda_2}e^{i\lambda\phi}$$

$$\times[(1-z)\delta_{\lambda,-2\lambda_1} + z\delta_{\lambda,2\lambda_1}]\varepsilon K_1(\varepsilon r)\},$$

$$A_\lambda^{\lambda_1,\lambda_2}(z,\mathbf{r}) = \frac{\sqrt{2\alpha_W N_c}}{2\pi}$$

$$\times\{\delta_{\lambda_1,\lambda_2}\delta_{\lambda,2\lambda_1}(2\lambda_1)[(1-z)m - z\mu]K_0(\varepsilon r) \qquad (11)$$

$$+ i\delta_{\lambda_1,-\lambda_2}e^{i\lambda\phi}[(1-z)\delta_{\lambda,-2\lambda_1} + z\delta_{\lambda,2\lambda_1}]\varepsilon K_1(\varepsilon r)\},$$

where

$$\varepsilon^2 = z(1-z)Q^2 + (1-z)m^2 + z\mu^2 \qquad (12)$$

and $K_\nu(x)$ is the modified Bessel function. We do not consider Cabibbo suppressed transitions and

$$\alpha_W = g^2/4\pi.$$

The quark and antiquark masses are $m$ and $\mu$, respectively. The azimuthal angle $\mathbf{r}$ is denoted by $\phi$. To switch $W^+ \longrightarrow W^-$ one should replace $m \longleftrightarrow \mu$ in the equations above.

The diagonal elements of density matrix

$$\rho_{\lambda\lambda'} = \sum_{\lambda_1,\lambda_2} \Psi_\lambda^{\lambda_1,\lambda_2}(\Psi_{\lambda'}^{\lambda_1,\lambda_2})^* \qquad (13)$$

entering into Eq. (3) are as follows:

$$\rho_{00}(z,\mathbf{r}) = \sum_{\lambda_1,\lambda_2}(|V_0^{\lambda_1,\lambda_2}|^2 + |A_0^{\lambda_1,\lambda_2}|^2) = \frac{2\alpha_W N_c}{(2\pi)^2 Q^2}$$

$$\times\{[[2Q^2 z(1-z) + (m-\mu)[(1-z)m - z\mu]]^2 \qquad (14)$$

$$+ [2Q^2 z(1-z) + (m+\mu)[(1-z)m + z\mu]]^2]$$

$$\times K_0(\varepsilon r)^2 + [(m-\mu)^2 + (m+\mu)^2]\varepsilon^2 K_1(\varepsilon r)^2\}$$

and for $\lambda = \lambda' = \pm 1$

$$\rho_{+1+1}(z,\mathbf{r}) = |\Psi_{+1}^{+1/2+1/2}|^2 + |\Psi_{+1}^{-1/2+1/2}|^2$$

$$= \frac{8\alpha_W N_c}{(2\pi)^2}(1-z)^2[m^2 K_0(\varepsilon r)^2 + \varepsilon^2 K_1(\varepsilon r)^2], \qquad (15)$$

$$\rho_{-1-1}(z,\mathbf{r}) = |\Psi_{-1}^{-1/2-1/2}|^2 + |\Psi_{-1}^{-1/2+1/2}|^2$$

$$= \frac{8\alpha_W N_c}{(2\pi)^2}z^2[\mu^2 K_0(\varepsilon r)^2 + \varepsilon^2 K_1(\varepsilon r)^2]. \qquad (16)$$

At $Q^2 \longrightarrow 0$ the terms $\sim m^2/Q^2$, $\mu^2/Q^2$ in (14) remind us that $W$ interacts with the current, which is not conserved, while the $S$-wave terms in Eqs. (15) and (16) proportional to $m^2$ and $\mu^2$ remind us that this current is the parity-violating ($V - A$) current.

The density of quark–antiquark $c\bar{s}$ states in the transversely polarized $W^+$-boson is

$$\rho_{TT} = \frac{1}{2}(\rho_{+1+1} + \rho_{-1-1})$$

$$= \frac{4\alpha_W N_c}{(2\pi)^2}\{[(1-z)^2 m^2 + z^2\mu^2]K_0(\varepsilon r)^2 \qquad (17)$$

$$+ [(1-z)^2 + z^2]\varepsilon^2 K_1(\varepsilon r)^2\}.$$

One can see that our $\rho_{00}$ and $\rho_{TT}$ coincide with the probability densities $|\Psi_L|^2$ and $|\Psi_T|^2$ of [1] (see also [9], where the $z$ dependence of transverse and longitudinal CC cross sections is discussed).

The momentum partition asymmetry of both $\rho_{-1-1}$ and $\rho_{+1+1}$ is striking: the left-handed quark in the decay of the left-handed $W^+$ gets the lion's share of the $W^+$ light-cone momentum. The nature of this phenomenon is very close to the nature of well-known spin–spin correlations in neutron $\beta$ decay. An observable which is strongly affected by this left–right asymmetry is the structure function of the neutrino–nucleon DIS called $F_3$. Its definition in terms of $\sigma_R$ and $\sigma_L$ of Eq. (3) is as follows:

$$2xF_3(x,Q^2) = \frac{Q^2}{4\pi^2\alpha_W}[\sigma_L(x,Q^2) - \sigma_R(x,Q^2)]. \qquad (18)$$

To estimate the consequences of the left–right asymmetry for $F_3$ at high $Q^2$ such that

$$\frac{m^2}{Q^2} \ll 1, \quad \frac{\mu^2}{Q^2} \ll 1 \qquad (19)$$

one should take into account that the dipole cross-section $\sigma(x, r)$ in Eq. (3) is related to the unintegrated gluon structure function $\mathcal{F}(x, \kappa^2) = \partial G(x, \kappa^2)/\partial \log \kappa^2$, as [10]

$$\sigma(x, r) = \frac{\pi^2}{N_c} r^2 \alpha_S(r^2)$$
$$\times \int \frac{d\kappa^2 \kappa^2}{(\kappa^2 + \mu_G^2)^2} \frac{4[1 - J_0(\kappa r)]}{\kappa^2 r^2} \mathcal{F}(x_g, \kappa^2) \tag{20}$$

and to the Double Leading-Log the Approximation (DLLA), i.e., for small dipoles,

$$\sigma(x, r) \approx \frac{\pi^2}{N_c} r^2 \alpha_S(r^2) G(x_g, A/r^2), \tag{21}$$

where $\mu_G = 1/R_c$ is the inverse correlation radius of perturbative gluons and $A \simeq 10$ comes from the properties of the Bessel function $J_0(y)$. Because of the scaling violation, $G(x, Q^2)$ rises with $Q^2$ but the product $\alpha_S(r^2)G(x, A/r^2)$ is approximately flat in $r^2$. At large $Q^2$, the leading contribution to $\sigma_\lambda(x, Q^2)$ comes from the $P$-wave term, $\varepsilon^2 K_1(\varepsilon r)^2$, in Eqs. (15) and (16). The asymptotic behavior of the Bessel function, $K_1(x) \simeq \exp(-x)/\sqrt{2\pi/x}$, makes the **r**-integration rapidly convergent at $\varepsilon r > 1$. Integrating over **r** in Eq. (3) yields

$$\sigma_L \propto \int_0^1 dz \frac{z^2}{\varepsilon^2} \alpha_S G \sim \frac{\alpha_S G}{Q^2} \log \frac{Q^2}{\mu^2} \tag{22}$$

and similarly

$$\sigma_R \propto \int_0^1 dz \frac{(1-z)^2}{\varepsilon^2} \alpha_S G \sim \frac{\alpha_S G}{Q^2} \log \frac{Q^2}{m^2}. \tag{23}$$

The left–right asymmetry certainly also affects the slowly varying product $\alpha_S G$, which for the purpose of crude estimate is taken at some rescaled virtuality $\sim Q^2$, which is approximately/logarithmically the same for $\sigma_L$ and $\sigma_R$. Hence,

$$\sigma_L - \sigma_R \propto \frac{\alpha_S G}{Q^2} \log \frac{m^2}{\mu^2}. \tag{24}$$

Notice that, in spite of the apparent asymmetry of the $z$ distribution, both $\sigma_L$ and $\sigma_R$ get equal scaling contributions from the integration domains near the peaks $z = 1$ and $z = 0$, respectively. Therefore, $xF_3$ is free of endpoint contributions.

At $Q^2 \longrightarrow 0$ and $\mu^2/m^2 \ll 1$, the cross-sections $\sigma_L$ and $\sigma_R$ are as follows:

$$\sigma_L \propto \frac{\alpha_S G}{m^2}\left(\log \frac{m^2}{\mu^2} - \frac{3}{2}\right), \quad \sigma_R \propto \frac{\alpha_S G}{2m^2}. \tag{25}$$

We evaluate $xF_3(x, Q^2)$ making use of Eqs. (3) and (20) with the differential gluon density function $\mathcal{F}(x_g, \kappa^2)$ determined in [11]. As reported in [11], the approach developed works very well in the perturbative region of high $Q^2$ and small $x \lesssim 0.01$. In addition, a realistic extrapolation of $\mathcal{F}(x_g, \kappa^2)$ into the soft region also allows calculations at lowest $Q^2$ [11]. In our calculations for $Q^2 \lesssim M^2 = 2(m^2 + \mu^2)$, the gluon density $\mathcal{F}(x_g, \kappa^2)$ enters (20) at the gluon momentum fraction $x_g = x(1 + M^2/Q^2)$. For large virtualities, $Q^2 \gtrsim M^2$, we put $x_g = 2x$. Direct evaluation of the proton DIS structure function $F_{2p}(x, Q^2)$ shows that this prescription corresponding to the collinear DLLA ensures a good description of experimental data on light and heavy flavor electro-production in a wide range of photon virtualities down to $Q^2 \sim 1$ GeV$^2$. The constituent quark masses are as follows: $m_u = m_d = 0.2$ GeV, $m_s = 0.35$ GeV and $m_c = 1.3$ GeV.

The $xF_3$ data reported by the CCFR Collaboration are presented in Fig. 1. Shown is the $Q^2$ dependence of $xF_3$ for several of the smallest values of $x$ [12]. It should be emphasized that we focus on the vacuum exchange contribution to $xF_3$ corresponding to the excitation of the $c\bar{s}$ state in process (1). Therefore, the structure function $xF_3$ differs from zero only due to the strong left–right asymmetry of the light-cone $|c\bar{s}\rangle$ Fock state. Shown by the solid line in Fig. 1 is the pomeron exchange contribution to $xF_3$. The latter can be interpreted in terms of parton densities as the sea-quark component of $xF_3$.

Looking at Fig. 1, one should bear in mind that the smallest available values of $x$ are in fact only moderately small and there is also quite a significant valence contribution to $xF_3$. The valence term, $xV$, is the same for both the $\nu N$ and $\bar{\nu} N$ structure functions of an isoscalar nucleon. The sea-quark term in the $xF_3^{\nu N}$ denoted by $xS(x, Q^2)$ has the opposite sign for $xF_3^{\bar{\nu} N}$; the substitution $m \longleftrightarrow \mu$ in Eqs. (15) and (16) entails $\sigma_L \longleftrightarrow \sigma_R$. Therefore,
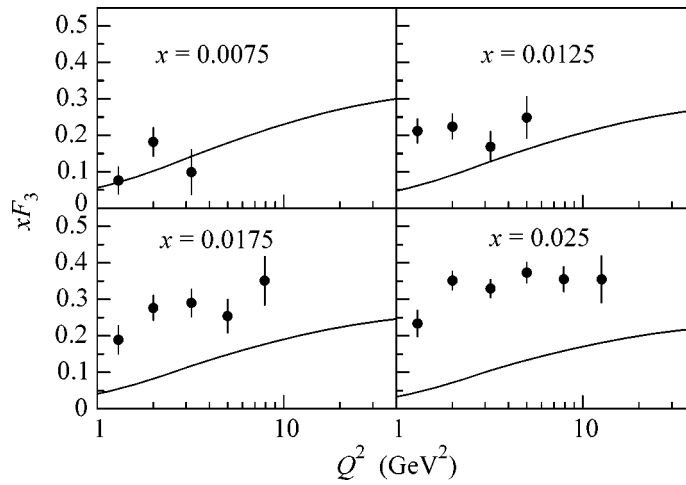
$$xF_3^{\nu N} = xV + xS, \tag{26}$$

and

$$xF_3^{\bar{\nu} N} = xV - xS. \tag{27}$$

One can combine the $\nu N$ and $\bar{\nu} N$ structure functions to isolate the pomeron exchange term:

$$\Delta xF_3 = xF_3^{\nu N} - xF_3^{\bar{\nu} N} = 2xS. \tag{28}$$

The extraction of $\Delta xF_3$ from CCFR $\nu_\mu Fe$ and $\bar{\nu}_\mu Fe$ differential cross section in a model-independent way has been reported in [13]. Figure 2 shows the extracted val-

**Fig. 1.** Data points are CCFR measurements of $xF_3(x, Q^2)$ [12]. Curves show the vacuum exchange contribution to $xF_3(x, Q^2)$.

ues of $\Delta xF_3$ as a function of $Q^2$ for the two smallest values of $x$. Also shown are the results of our calculations.

After evaluating the difference of the left and right cross sections, let us turn to their sum and, as a consistency check, evaluate the structure function

$$2xF_1(x, Q^2) = \frac{Q^2}{4\pi^2\alpha_W}\sigma_T(x, Q^2), \qquad (29)$$

where

$$\sigma_T = \frac{1}{2}[\sigma_L(x, Q^2) + \sigma_R(x, Q^2)]. \qquad (30)$$

The CCFR Collaboration measurements [14] of the structure function $2xF_1$ as a function of $Q^2$ for three values of $x$ are shown in Fig. 3. Theory and experiment here are in qualitatively the same relations as in Fig. 1. In the small-$x$ region, $x < 0.01$, dominated by the pomeron exchange, our estimates are in agreement with the data. For larger $x$, nonvacuum contributions enter the game and a certain divergence shows up. This divergence will increase if we take into account nuclear effects. Indeed, the CCFR/NuTeV structure functions $xF_3^{\nu N}$ and $xF_3^{\bar\nu N}$ are extracted from the $\nu Fe$ and $\bar\nu Fe$ data. The nuclear thickness factor, $T(b) = \int dz n(\sqrt{z^2 + b^2})$, where $b$ is the impact parameter and $n(r)$ is the nuclear matter density, $\int d^3 r n(r) = A$, makes the nuclear cross section
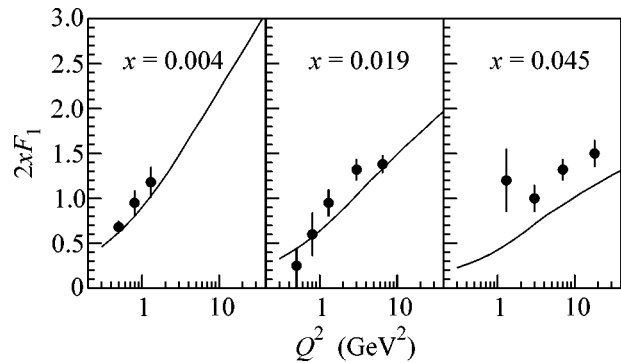
$$\sigma_\lambda^A = A\langle\sigma_\lambda\rangle - \delta\sigma_\lambda^A, \qquad (31)$$

with the nuclear shadowing term

$$\delta\sigma_\lambda^A \simeq \frac{\pi}{4}\langle\sigma_\lambda^2\rangle\int db^2 T(b)^2 \qquad (32)$$
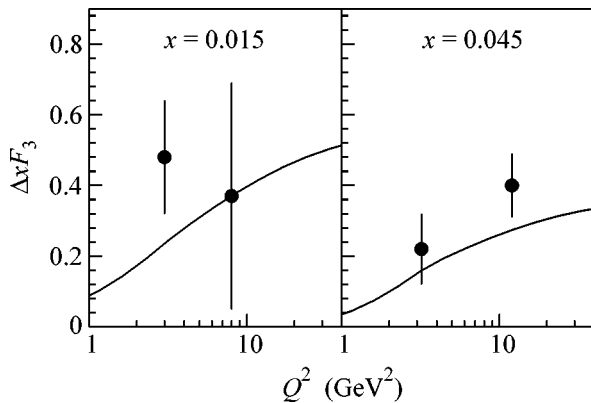


**Fig. 2.** $\Delta xF_3$ data as a function of $Q^2$ [13]. The results of color dipole description are shown by solid lines.



**Fig. 3.** CCFR measurements of $2xF_1(x, Q^2)$ [14] compared with our estimates. The lines are the vacuum exchange contributions to $2xF_1(x, Q^2)$.

very sensitive to the left–right asymmetry of the $\nu$-nucleon cross-sections. In Eqs. (31) and (32), $\langle\sigma_\lambda\rangle = \langle\Psi_\lambda|\sigma(x, r)|\Psi_\lambda\rangle$ and $\langle\sigma_\lambda^2\rangle = \langle\Psi_\lambda|\sigma(x, r)^2|\Psi_\lambda\rangle$. Hence, the nuclear shadowing correction is

$$\delta xF_3 \simeq \frac{Q^2}{4\pi^2\alpha_W}\frac{\pi\langle\sigma_L^2 - \sigma_R^2\rangle}{8A}\int db^2 T(b)^2, \qquad (33)$$

which should be added to $xF_3$ extracted from the $\nu Fe$ data to get the "genuine" $xF_3$. Since $\langle\sigma_L^2\rangle \propto 1/\mu^2$ and $\langle\sigma_R^2\rangle \propto 1/m^2$, this correction is large and positive-valued and increases $xF_3$ of the impulse approximation.

Summarizing, we developed the light-cone color dipole description of the left–right asymmetry effect in charged current DIS at small Bjorken $x$. We compared our results with experimental data and found a considerable vacuum exchange contribution to the structure functions $xF_3^{\nu N}$. This contribution is found to dominate the structure function $\Delta xF_3 = xF_3^\nu - xF_3^{\bar\nu}$ of an isoscalar nucleon extracted from nuclear data. The theory is in reasonable agreement with the data, but it is shown that nuclear effects make this comparison a somewhat more complicated procedure. The color dipole analysis of nuclear effects in the CC DIS will be published elsewhere.

## REFERENCES

1. V. Barone, M. Genovese, N. N. Nikolaev, *et al.*, Phys. Lett. B **292**, 181 (1992).

2. V. Barone, U. D'Alesio, and M. Genovese, Phys. Lett. B **357**, 435 (1995); M. Bertini, M. Genovese, N. N. Nikolaev, and B. G. Zakharov, Phys. Lett. B **442**, 398 (1998); V. Barone, M. Genovese, N. N. Nikolaev, *et al.*, Phys. Lett. B **317**, 433 (1993); Phys. Lett. B **328**, 143 (1994).

3. N. N. Nikolaev and B. G. Zakharov, Z. Phys. C **49**, 607 (1991); Z. Phys. C **53**, 331 (1992); Z. Phys. C **64**, 631 (1994).

4. A. H. Mueller, Nucl. Phys. B **415**, 373 (1994); A. H. Mueller and B. Patel, Nucl. Phys. B **425**, 471 (1994).

5. A. Hebecker, Phys. Rep. **331**, 1 (2000).

6. A. B. Zamolodchikov, B. Z. Kopeliovich, and L. I. Lapidus, JETP Lett. **33**, 595 (1981).

7. G. Bertsch, S. J. Brodsky, A. S. Goldhaber, and J. R. Gunion, Phys. Rev. Lett. **47**, 297 (1981).

8. G. P. Lepage and S. J. Brodsky, Phys. Rev. D **22**, 2157 (1980); S. Brodsky, H.-Ch. Pauli, and S. Pinsky, Phys. Rep. **301**, 299 (1998).

9. V. Barone, M. Genovese, N. N. Nikolaev, *et al.*, Phys. Lett. B **328**, 143 (1994).

10. N. N. Nikolaev and B. G. Zakharov, Phys. Lett. B **332**, 184 (1994).

11. I. P. Ivanov and N. N. Nikolaev, Phys. At. Nucl. **64**, 753 (2001).

12. W. G. Seligman, C. G. Arroyo, L. de Barbaro, *et al.*, Phys. Rev. Lett. **79**, 1213 (1997).

13. U. K. Yang, T. Adama, A. Alton, *et al.*, Phys. Rev. Lett. **86**, 2742 (2001).

14. U. K. Yang, T. Adama, A. Alton, *et al.*, Phys. Rev. Lett. **87**, 251 802 (2001).

# Does the Coherent Bremsstrahlung of Fission Fragments Exist?

## V. A. Varlachev, G. N. Dudkin, and V. N. Padalko

*Research Institute of Nuclear Physics, Tomsk, 634050 Russia*
*e-mail: dudkin@npi.tpu.ru*
Received July 25, 2005

The spectrum of $\gamma$ rays from the neutron-induced fission of $^{235}$U nuclei has been studied in a range of 10–90 MeV. The experiment has been carried out in the horizontal experimental channel of a nuclear reactor. The energy spectrum was measured using a single-crystal NaI(T1) spectrometer. The data on the energy dependence of the yield of $\gamma$ rays have been obtained in a range of 12–38 MeV. The upper limit on the probability of the emission of $\gamma$ rays has been determined for a range of 38–90 MeV. It has been shown that the experimental data are inconsistent with available models attributing the yield of $\gamma$ rays in this energy range to the coherent bremsstrahlung of fission fragments in the Coulomb field. © 2005 Pleiades Publishing, Inc.

PACS numbers: 24.75.+i, 25.85.Ec

One of the fundamental problems of nuclear fission physics concerns the characteristics of the energy spectrum of $\gamma$ rays accompanying the fission process for energies above > 10 MeV. Experimental data on the energy spectrum of $\gamma$ rays in a range of 10–20 MeV were obtained only with the source of spontaneously fissioning nuclei $^{252}$Cf and $^{238}$U [1–7]. The spectra are characterized by an exponential dependence with an inverse slope of $E_0 = 1.4$–2.2 MeV. The shapes of the spectra quite closely coincide with each other, but they differ in intensity by several times. The yield of $\gamma$ rays in this energy range is associated with the presence of the highly excited states of daughter nuclei arising in the fission process and, in particular, with the direct excitation of the giant dipole resonance.

For energies above 20 MeV, both experimental data and theoretical calculations are contradictory. In three experiments, the yield of $\gamma$ rays with such a high energy was not detected, and only an upper bound was determined [4, 8, 9]. In three other experiments, the energy spectrum was measured [3, 5, 7]. The yield of $\gamma$ rays with energies 20–120 MeV is theoretically attributed to the coherent bremsstrahlung of fission fragments in the Coulomb field and depends on the fundamental characteristics of nuclear fission such as the fission neck length [7], acceleration mechanism (instantaneous, pure Coulomb [3]), quantum-mechanical corrections for the effect of the tunneling of fragments through the potential barrier [4]. The calculations in different models differ by several orders of magnitude.

At the same time, in nuclear fusion reactions actively studied in recent time, the yield of $\gamma$ rays due to the coherent bremsstrahlung of nuclei is proved experimentally and justified theoretically [10–14].

The inconsistency of experimental and theoretical situations in nuclear fission requires further investigations. For this reason, the aim of this work is to analyze the spectrum of $\gamma$ rays arising in the neutron-induced fission of $^{235}$U nuclei for energies above 10 MeV.

The experiment was carried out in the horizontal experimental channel of the nuclear reactor at the Research Institute of Nuclear Physics, Tomsk, Russia. The energy spectrum was measured by a single-crystal NaI(T1) spectrometer with the crystal 20 cm in diameter and 20 cm in length (7.7 radiation length). To protect the detector from the neutron flux and to reduce the $\gamma$-ray flux density to an acceptable level, a distilled-water filter 300 cm in length was placed between the spectrometer and reactor core. Two lead collimators *1* and *2*, which were placed after the filter, specified the solid angle of the detector. The distance between the input of lead collimator *1* and the output of collimator *2* is equal to 150 cm. The diameter of both apertures is equal to 2 cm and their lengths are equal to 15 cm. As a result, for the reactor power $W = 6$ MW, a $\gamma$-ray flux with an intensity of $I = 5 \times 10^4$ photons/s is incident onto the detector.

To protect the detector from the cosmic-ray background, we used the passive protection (lead and heavy concrete) and active protection—scintillation detectors that surrounded the NaI spectrometer and operates in the anticoincidence mode. For the efficiency of detecting $\gamma$ rays by the NaI(T1) spectrometer to be energy-independent (due to the escape of electrons and $\gamma$ rays from the crystal and their inhibition by anticoincidence counters), the spectrometer was first surrounded from the lateral sides by the lead protection 5 cm in thickness and then by anticoincidence counters.

The signal from the anode of a FEU-49B photomultiplier that is in optical contact with the NaI(T1) crystal was fed to the charge-to-digital converter with a charge-integration window of 300 ns. The energy calibration of the spectrometer was performed as follows. The lower part of the energy scale was calibrated by means of the γ lines of the $^{60}$Co source. To calibrate the middle part of the energy scale of the spectrometer, we used the γ-radiation lines arising in the radiative capture of neutrons on Al and Fe ($E_\gamma = 7.72$ and 7.64 MeV, respectively) contained in the plug of the horizontal channel and fuel elements [15]. For calibration in an energy range of 30–100 MeV, the monoenergetic secondary electron beam of the SIRIUS synchrotron is used.

The resolution was equal to $\delta = 11$ and 7.7% at the $^{60}$Co ($E_\gamma = 1.33$ MeV) line and the 7.72-MeV and 7.64-MeV lines (unseparated lines), respectively. With a further increase in energy, the resolution depends on energy only slightly, remaining at a level of $\simeq 8\%$. For energies >10 MeV, the efficiency of the detection of γ radiation by the NaI spectrometer is equal to ~85% (calculated value [16]).

Figure 1 shows the apparatus energy spectrum of γ rays that are emitted from the reactor core and passed through 300 cm of water. The lines of captured γ radiation are identified using the data taken from [17]. The numbers in the figure indicate the γ lines associated with various processes: (1, 2) the lines of the $^{60}$Co source ($E_\gamma = 1.17$, 1.33 MeV, respectively); (3) the unseparated lines of capture radiation on Cr (stainless steel component, $E_\gamma = 1.78$, 1.89 MeV); (4) capture radiation on water hydrogen ($E_\gamma = 2.2$ MeV); (5) the sum peak from the $^{60}$Co source ($E_\gamma = 2.5$ MeV); (6) the unseparated lines of capture radiation on Be (core reflector, $E_\gamma = 6.8$ MeV) and Ti (stainless steel component, $E_\gamma = 6.76$ MeV); (7) the unseparated lines of capture radiation on Al (fuel element matrix, extractant, $E_\gamma = 7.72$ MeV) and Fe (plug of the experimental channel, $E_\gamma = 7.64$ MeV); (8) the unseparated lines of capture radiation on Cr and Ni (stainless steel components, $E_\gamma = 8.8$, 8.9 MeV, respectively); (9) capture radiation on Cr ($E_\gamma = 9.7$ MeV); and (10) $E_\gamma = 11.3$ MeV. The origin of the last line was not at first understood. For this reason, additional experiments were carried out, which enabled us to verify that the appearance of this line could not be attributed to the misoperation of the apparatus or the loading of the spectrometer. As a result, the most probable source of this line is found to be the radiative capture of thermal neutrons by $^{59}$Ni nuclei, which were accumulated in more than 20 years of exploitation of the reactor due to the $^{58}$Ni$(n, \gamma)^{59}$Ni reaction ($E_\gamma = 11.38$ MeV) on $^{58}$Ni contained in stainless steel [18]. Further, this line was used as a very convenient reference line for controlling the energy scale. In addition in Fig. 1, (11) is the energy range 10–20 MeV that is likely associated with the presence of highly excited states of daughter nuclei and, in particular, with the direct exci-
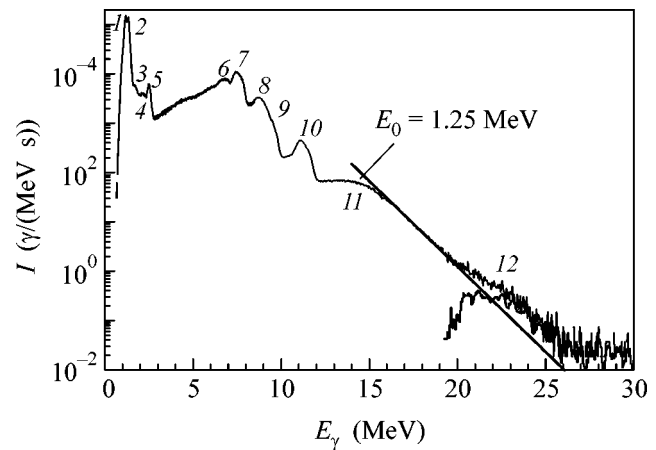


**Fig. 1.** Apparatus energy spectrum of γ rays emitted from the reactor core and passed through the water filter. For notation, see the text.

tation of the giant dipole resonance and (12) is the energy range 20–30 MeV, where the mechanism of the coherent bremsstrahlung of fission fragments in the Coulomb field can be manifested. The 16–20-MeV spectral section can be approximated by an exponential with the inverse slope parameter $E_0 = 1.25$ MeV. If the contribution of the experimental distribution is subtracted in this spectral section, the peak with the maximum at $E_\gamma = 22.5$ MeV is clearly seen.

In order to exclude the effect of the superposition of pulses, further measurements of the spectrum of γ rays were carried out with a Tektronix-TDS 2014 digital storage oscilloscope connected in parallel with the charge-to-digital converter in two separate runs with different apparatus thresholds 12 and 26 MeV. The spectral section for $E_\gamma > 26$ MeV was scanned in the 12-h measurement run (the channel was open for 6 h and was close for 6 h by a 20-cm lead filter). The correspondence between the amplitudes of the signals from the charge-to-digital converter and TDS was established by means of the 11.38-MeV line.

In order to correctly take into account dead time, the measuring system included a light emitting diode [illuminating NaI(T1) crystal] and a generator of calibrated-frequency pulses triggering the light emitting diode (generator frequency was taken from 1 to 0.01 Hz in dependence on the energy range where measurements were performed). The peak from the light emitting diode was detected with an energy of 60 MeV and the pulse shape was chosen such that it clearly differed from pulses generated by cosmic-ray muons.

The massive (off-line) processing of the oscillograms was performed with a criterion formed due to the individual analysis of each oscillogram in a test sample. The criterion, which is the ratio of the pulse area to its amplitude, is a quite sensitive indicator of the superposition of pulses and is independent of the pulse amplitude. Each oscillogram was preliminarily smoothed by
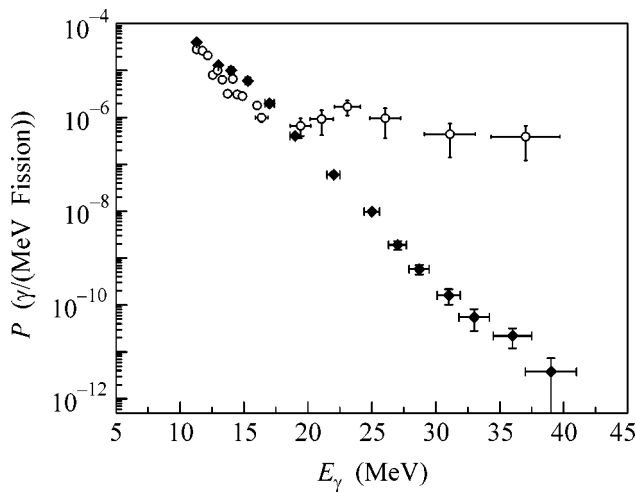
**Fig. 2.** Energy dependence of the probability of the emission of $\gamma$ rays per fission event per 1 MeV in an energy range of 12–40 MeV: ($\blacklozenge$) our result and ($\circ$) experimental data taken from [5].
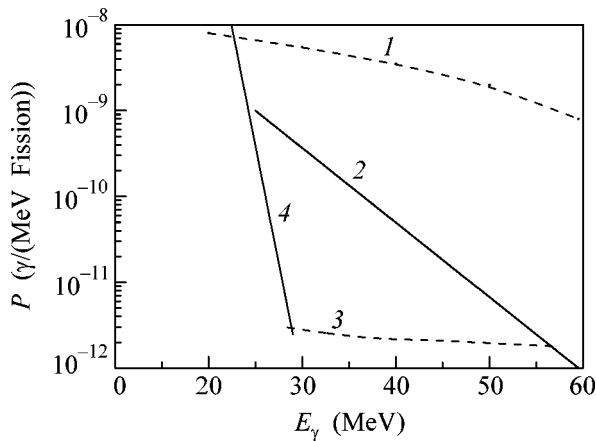


**Fig. 3.** Energy dependence of the probability of the emission of $\gamma$ rays per fission event per 1 MeV in an energy range of 20–100 MeV: (*1*) the experimental bound obtained in [9], (*2*) the exponential approximation of the theoretical calculation performed in [4] (inverse slope parameter $E_0 = 10$ MeV), (*3*) our experimental bound, (*4*) the exponential approximation of our experimental data for the probability of the emission of $\gamma$ rays in an energy range of 20–38 MeV (inverse slope parameter $E_0 = 1.6$ MeV).

a Gaussian filter in order to discriminate apparatus noise. The superposition effect is on average equal to 20% in an energy range of 12–20 MeV and reaches 40% in a range of 20–40 MeV.

Figure 2 shows the energy dependence of the probability $P$ of the emission of $\gamma$ rays per fission event per 1 MeV in an energy range of 12–40 MeV. The probability $P$ was estimated as

$$ P = \frac{4\pi N_\gamma}{I_f \Omega k_\gamma \varepsilon}. \tag{1} $$

Here, $\Omega = 1.26 \times 10^{-5}$ sr is the calculated solid angle of the detector; $I_f = 4.9 \times 10^{15}$ events/s is the calculated intensity of fissions in the core region scanned by the spectrometer; $k_\gamma = (1.1–4.4) \times 10^{-3}$ is the calculated coefficient taking into account the absorption of $\gamma$ rays in the water filter and the materials of the reactor core; $\varepsilon = 0.85$ is the efficiency of detecting $\gamma$ rays by the NaI(T1) spectrometer, which is assumed to be energy-independent; and $N_\gamma$ is the yield of $\gamma$ radiation at the corresponding energy that is detected by the NaI(T1) spectrometer and is averaged over the energy resolution of the spectrometer $\delta = 8\%$ (photons/(MeV s)). The real time of statistics accumulation in two energy ranges is $t_1 = 5 \times 10^3$ s and $t_2 = 1.86 \times 10^4$ s.

It is seen that the spectral irregularity at $E_\gamma = 22.5$ MeV (Fig. 1) is not observed. We have to state that this artifact is a result of the accidental superposition of pulses from the 7.6-MeV $\gamma$ rays and $\gamma$ rays from region *11* (average energy is equal to 14.5 MeV).

Experimental results obtained in [5] with a $^{252}$Cf source are also shown in Fig. 2. The authors of that work attributed the yield of $\gamma$ rays with energies above 20 MeV to the possible contribution from the coherent bremsstrahlung of fission fragments. Our results and results from [5] are in certain agreement in the region of the excitation of the giant dipole resonance (~15 MeV), whereas they are significantly inconsistent for $E_\gamma > 20$ MeV.

After the subtraction of the cosmic-ray background, eight events remain in the spectrum in a range of 38–125 MeV. The cosmic-ray background in this energy range is $N_b = 900$ events in $t_2 = 1.86 \times 10^4$ s. Using a Poisson statistical analysis of these data, one can obtain an upper bound $P(E_\gamma > 38 \text{ MeV}) \leq 1.2 \times 10^{-10}$ photon per fission event at a CL of 90%.

The most stringent theoretical bound on the probability of the emission of $\gamma$ rays due to the mechanism of the coherent bremsstrahlung of fission fragments of $^{252}$Cf was obtained in [4]. The authors of that work attempted to include the effect of the potential barrier on the probability of the emission of bremsstrahlung $\gamma$ rays by fission fragments. As a result, the probability of the emission of $\gamma$ rays that was calculated using this model is almost two orders of magnitude less than that calculated in the classical model of Coulomb acceleration.

Our results, the experimental data obtained in [9] for $^{252}$Cf, and theoretical calculations from [4] are shown in Fig. 3 for $\gamma$-ray energies 20–100 MeV. It is remarkable that the experimental spectrum that we obtained for $\gamma$ rays in an energy range of 20–38 MeV and the theoretical spectrum in an energy range of 30–100 MeV have different inverse slope parameters (1.6 and 10 MeV, respectively) of the exponential energy dependences. Therefore, the spectra are determined by different physical processes. For example, in an energy range of 10–20 MeV, the emission of $\gamma$ rays in nuclear fusion

reactions, as well as in nuclear fission reactions, is attributed to the excitation of the giant dipole resonance [19] and spectra are characterized by the exponential energy dependence with the inverse slope parameters $E_0 = 1.5$–$2.0$ MeV. For energies above 30 MeV, spectra are also characterized by the exponential dependence, but $E_0 = 10$ MeV and the spectra are not attributed to coherent nucleon–nucleon bremsstrahlung.

A question arises: Does the coherent bremsstrahlung of fission fragments in the Coulomb field exist? It seems to exist, because bremsstrahlung was experimentally observed [20, 21] and theoretically justified [22–24] even for the $\alpha$ decay of the $^{210,\,214}$Po, $^{226}$Ra, and $^{244}$Cm nuclei. If it exists, what is the energy spectrum of $\gamma$ rays from this process? If it does not exist, what is the mechanism of its suppression?

## REFERENCES

1. H. W. Sobel, A. A. Hruschka, W. R. Kropp, *et al.*, Phys. Rev. C **7**, 1564 (1973).

2. F. S. Dietrich, J. C. Browne, W. J. O'Connel, and J. Kay, Phys. Rev. C **10**, 795 (1974).

3. J. Kasagi, H. Hama, K. Yoschida, *et al.*, J. Phys. Soc. Jpn. Suppl. **58**, 620 (1989).

4. S. J. Luke, C. A. Gosset, and R. Vandenbosch, Phys. Rev. C **44**, 1548 (1991).

5. H. van der Ploeg, R. Postma, J. C. Bacelar, *et al.*, Phys. Rev. Lett. **68**, 3145 (1992).

6. H. van der Ploeg, J. C. Bacelar, A. Buda, *et al.*, Phys. Rev. C **52**, 1915 (1995).

7. N. V. Eremin, T. G. Klochko, M. G. Glotova, *et al.*, in *Proceedings of 14th Conference on Nuclear Fission* (Obninsk, Russia, 2000), p. 196.

8. V. G. Nikolenko, A. B. Popov, G. S. Samosvat, and Hvan Cher Gu, Pis'ma Zh. Éksp. Teor. Fiz. **27**, 65 (1978) [JETP Lett. **27**, 59 (1978)].

9. Yu. N. Pokotilovskiĭ, Yad. Fiz. **52**, 942 (1990) [Sov. J. Nucl. Phys. **52**, 599 (1990)].

10. K. Nakayuma and G. F. Bertsch, Phys. Rev. C **36**, 1848 (1987).

11. J. A. Behr, K. A. Snover, C. A. Gosset, *et al.*, Phys. Rev. C **53**, 1759 (1996).

12. U. Eichmann, C. Emst, L. M. Satarov, and W. Greiner, Phys. Rev. C **62**, 044902 (2000).

13. M. Hoefman, L. Aphecetche, J. C. S. Bacelar, *et al.*, Phys. Rev. Lett. **85**, 1404 (2000).

14. M. Volkerts, J. C. S. Bacelar, M. J. van Goethem, *et al.*, Phys. Rev. Lett. **90**, 062301 (2003).

15. V. N. Avaev, Yu. A. Egorov, I. Ya. Emel'yanov, *et al.*, in *Problems in Reactor Shielding Physics*, Ed. by D. L. Broder *et al.* (Gosatomizdat, Moscow, 1963; NASA, Washington, D.C., 1967).

16. M. Yu. Andreyashkin, V. N. Zabaev, B. N. Kalinin, *et al.*, Prib. Tekh. Éksp., No. 6, 55 (1989).

17. V. I. Gumma, A. M. Demidov, V. A. Ivanov, and V. V. Miller, *Neutron-Radiation Analysis* (Énergoatomizdat, Moscow, 1984) [in Russian].

18. V. A. Varlachev, G. N. Dudkin, and V. N. Padalko, Abstracts of Papers, *III International Conference on Physicotechnical Problems in Atomic Energetics and Industry* (TPU, Tomsk, 2005), p. 42; At. Energ. (in press).

19. D. Santonocito, P. Piattelli, Y. Blumenfeld, *et al.*, Phys. Rev. C **66**, 044619 (2002).

20. A. D. Arrigo, N. V. Eremin, G. Fazio, *et al.*, Phys. Lett. B **332**, 25 (1994).

21. J. Kasagi, H. Yamazaki, N. Kasajima, *et al.*, Phys. Rev. Lett. **79**, 371 (1997).

22. I. S. Batkin, I. V. Kopytin, and T. A. Churakova, Yad. Fiz. **44**, 1454 (1986) [Sov. J. Nucl. Phys. **44**, 946 (1986)].

23. E. V. Tkalya, Zh. Éksp. Teor. Fiz. **116**, 390 (1999) [JETP **89**, 208 (1999)].

24. S. D. Kurgalin, Yu. M. Chuvil'skiĭ, and T. A. Churakova, Izv. Ross. Akad. Nauk, Ser. Fiz. **65**, 666 (2001).

*Translated by R. Tyapaev*

# Condensate Preserving the Symmetry of the Lagrangian.
# Symmetry Breakdown

## V. V. Vladimirskiĭ

*Institute of Theoretical and Experimental Physics, Moscow, 117218 Russia*
Received April 21, 2005; in final form, August 1, 2005

A multicomponent scalar field may preserve the symmetry of the Lagrangian when the stability of the perturbation theory vacuum is lost. This leads to the appearance of a degenerate vacuum, whose excitation spectrum slightly differs from the spectrum observed in the case of spontaneous symmetry breaking. The possibility of the appearance of such a condensate in a QCD vacuum is discussed. © *2005 Pleiades Publishing, Inc.*

PACS numbers: 11.15.Ex

## 1. FORMULATION OF THE PROBLEM

Since the papers by Goldstone [1] and Higgs [2], the opinion that spontaneous symmetry breaking occurs when a trivial perturbation-theory vacuum loses its stability and that this effect is responsible for the appearance of the mass of gauge bosons has prevailed in the literature devoted to nonperturbative effects in quantum field theory. A more careful approach to symmetry breaking shows that symmetry is broken only in the presence of interactions facilitating this process. The masses of gauge bosons arise due to the formation of condensate. The condensate may break symmetry or may remain completely symmetric. In classical (not quantum) field theory, symmetry breaking necessarily occurs. The extension of this effect to quantum theory is not universally substantiated. However, the interaction of matter fields with gauge fields may itself facilitate symmetry breaking; consequently, in a situation when the Higgs mechanism is possible, symmetry breaking still occurs, but not quite in the same way as in the classical theory. Running ahead, we can state that if the word "spontaneous" is omitted from the conventional description of spontaneous symmetry breaking, we can preserve all formulas and results. However, this does not mean that the difference between the classical and quantum-mechanical approaches to symmetry breaking described below is insignificant. In our opinion, nontrivial verifiable effects may arise in complex problems of the field theory.

The difference between the classical and quantum-mechanical approaches can be illustrated using a simple example from atomic physics, in which no stability loss takes place in the system. Let us consider the motion of a spinless particle in the central field of attractive forces. The lowest bound state is characterized by zero angular momentum. In the classical approach, motion is possible only in the radial direction (rotational symmetry breaking). In quantum mechanics, an $S$ state possessing rotational symmetry is formed, whose wave function is independent of angular variables (symmetry is preserved).

An analogous difference must also be manifested in other cases of the degeneracy of the Lagrangian in certain (including generalized) coordinates. In the classical theory, a coordinate and its time derivative can be fixed simultaneously. In the quantum theory, this is forbidden by canonical commutation relations. This might permit symmetry conservation.

## 2. SIMPLEST MODEL

Let us consider an $n$-component real scalar field $\phi_j$ with the Lagrangian density

$$L = \frac{1}{2}(\partial_\mu \phi_j \partial_\mu \phi_j) - \frac{1}{2}\mu^2 \phi_j \phi_j - \frac{1}{4}\lambda(\phi_j \phi_j)^2 \qquad (1)$$

in the conventional Minkowski space. Such a theory is usually referred to as the linear sigma-model or the Ginzburg–Landau model (if the square of the mass is negative). The corresponding Hamiltonian (energy density) function is given by

$$
\begin{aligned}
H(\pi_j, \phi_j) = {} & \frac{1}{2}\pi_j \pi_j + \frac{1}{2}(\nabla \phi_j \nabla \phi_j) \\
& + \frac{1}{2}\mu^2 \phi_j \phi_j + \frac{\lambda}{4}(\phi_j \phi_j)^2.
\end{aligned}
\qquad (2)
$$

Here, $\pi_j = \partial L/\partial \dot{\phi}_j$ is the momentum conjugate to field $\phi_j$ and $\nabla_v$ are derivatives with respect to spatial coordinates. We can now carry out canonical quantization, introducing the commutation relations

$$[\phi_i(x, t), \phi_j(x', t)] = [\pi_i(x, t), \pi_j(x', t)] = 0, \quad (3)$$

$$[\pi_i(x, t), \phi_j(x', t)] = -i\delta_{ij}\delta^3(x - x'), \qquad (4)$$

and the wave function (functional) $\Psi(\phi_j, x_\mu)$. It is convenient to immediately perform the Fourier expansion in the coordinates of the functions $\phi_j(x_\mu)$:

$$\phi(x, t) = \int \frac{d^3 k}{(2\pi)^3} e^{ikx} \phi(k, t), \qquad (5)$$

$$H\Psi = \left( \frac{1}{2} \frac{\partial^2}{\partial \phi_j \partial \phi_j} + \frac{1}{2}(k_\mu k_\mu \phi_j \phi_j) \right.$$
$$\left. + \frac{1}{2}\mu^2 \phi_j \phi_j + \frac{\lambda}{4}(\phi_j \phi_j)^2 \right)\Psi, \qquad (6)$$

where index $\mu$ runs only over spatial values 1, 2, 3.

We will be interested in the situation associated with the loss of stability in this theory (in other words, for $\mu^2 < 0$). To simplify the formulas, we first consider the case of two fields

$$L = \frac{1}{2}(\partial_\mu \phi_1 \partial_\mu \phi_1 + \partial_\mu \phi_2 \partial_\mu \phi_2) - \frac{\lambda}{4}(\phi_1^2 + \phi_2^2 - v^2)^2, \quad (7)$$

where $v$ is a real-valued constant with the dimension of mass. Using the substitution

$$\varphi = \varphi_1 + i\varphi_2 = |\varphi| e^{i\theta}, \qquad (8)$$

we pass to polar coordinates in the field space. In these coordinates, the energy minimum is reached for $|\varphi| = v$. Angle $\vartheta$ may assume any value, i.e., $0 < \vartheta < 2\pi$. Obviously, the wave function $R(\varphi)$ that is independent of the angle $\vartheta$ and assumes values substantially differing from zero only in the vicinity of the energy minimum is a suitable vacuum solution for a coordinate-independent scalar. The spontaneous breaking of the $O(2)$ symmetry occurs in the classical theory: angle $\vartheta$ assumes any definite value and its time derivative is zero ($\partial \vartheta / \partial t = 0$). In the quantum theory, this is incompatible with commutation relation (4), in which the right-hand side can hardly be treated as zero. The correct quantum solution preserves the symmetry of the Lagrangian. Indeed, it follows from relation (4) that

$$\varphi[\dot{\vartheta}(\mathbf{x}), \vartheta(\mathbf{x'})] \propto -i\delta(\mathbf{x} - \mathbf{x'}); \qquad (9)$$

i.e., angle $\vartheta$ cannot be determined simultaneously with its time derivative. The advantage of the solution $\Psi = R(\varphi)$ over the formulas corresponding to spontaneous symmetry breaking is not quite obvious, because we are dealing with a system with indefinitely large volume and infinitely large number of degrees of freedom. However, one should take into account that it is an exact solution of the variational problem of determining the wave functional and spontaneous symmetry breaking does not correspond to any solution of the quantum-mechanical problem. Wavefunction $\Psi = R(\varphi)$ is normally not used, because it corresponds to infinitely large correlation radius. This is not admissible for many applications; to eliminate such a solution, the cluster decomposition $\langle 0|\varphi(x)\varphi(y)|0\rangle \longrightarrow \langle 0|\varphi(x)|0\rangle\langle 0|\varphi(y)|0\rangle$ for $|x - y| \longrightarrow \infty$ is employed. However, cluster decom-

position, which is natural in the physics of continuous media, is inapplicable to our model. It is much simpler to use the interaction with the gauge electromagnetic field, which is present in such problems.

## 3. INTERACTION WITH AN ABELIAN GAUGE FIELD

Let us consider the Lagrangian of a charged scalar field interacting with a gauge vector field:

$$L = -\frac{1}{4}(F_{\mu\nu})^2 + |D_\mu \phi|^2 - V(\phi),$$

$$F_{\mu\nu} = D_\mu A_\nu - D_\nu A_\mu, \quad D_\mu = \partial_\mu - ieA_\mu, \qquad (10)$$

$$V(\phi) = -\mu^2 \phi^* \phi + \frac{\lambda}{2}(\phi^* \phi)^2, \quad \mu^2 > 0.$$

The introduction of a nonzero charge $e \neq 0$ immediately leads to the sensitivity of the condensate to the choice of the azimuth angle $\vartheta$ (the condensate may be positive, negative, or neutral). The energy minimum is inherent in a neutral condensate. To analyze this situation, it is sufficient to define the annihilation operators for positive particles,

$$\phi_+ = \frac{\phi_1 - i\phi_2}{\sqrt{2}}, \qquad (11)$$

and for negative particles,

$$\phi_- = \frac{\phi_1 + i\phi_2}{\sqrt{2}}, \qquad (12)$$

as well as the corresponding current density vector,

$$j_\lambda = \frac{e}{2}[\phi^+ i\partial_\lambda \phi + (i\partial_\lambda \phi)^+ \phi].$$

The neutral condensate is formed if only one of the two components $\phi_1$ and $\varphi_2$ ($\vartheta = 0$ or $\vartheta = \pi/2$) remains in the operator of the condensate field as a result of interaction with the vector gauge field $A_\lambda$; such a symmetry breaking should not be referred to as spontaneous. However, this is a matter of terminology. After the introduction of interaction, the conditions for the fulfillment of the Goldstone theorem are violated and the quanta of azimuthal motion in the group space (variation of $\vartheta$) must at least acquire a mass.

The real situation is slightly more complicated. The structure of Lagrangian (10) does not require charge quantization. The commutation relations for scalar and vector fields do not impose such a requirement either; consequently, a certain arbitrariness appears in the analytical form of the interaction (in particular, complex notation of the charged field is not used in the original paper by Higgs [2] and the commutation of fields $\phi_1$, $\phi_2$ is employed instead of imaginary unity). In any version of the analytical representation, charge conjugation corresponds to the involution operator. The main phys-

ical result of analysis of the Higgs model is that a non-zero mass of the gauge field may appear. This result is independent of the above-mentioned features of the model and is preserved under forced charge quantization. Any new effects for models that are based on the Abelian symmetry group or are reducible to the $U(1)$ symmetry should not apparently be expected. However, new effects can be revealed by analyzing less studied non-Abelian symmetry groups.

## 4. COLOR GROUP

The model of quarks and gluons was developed long ago in hadron physics on the basis of the $SU(3)_{\text{col}}$ symmetry of the color group. No indication of symmetry breaking has been found. At the same time, according to some indications, the gluon field vacuum differs from trivial perturbation-theory vacuum in the presence of the vacuum condensate. Passage from the classical to quantum-mechanical interpretation of the concept of state makes it possible to replace the requirement that vacuum must be a singlet in color by a less stringent requirement that vacuum must possess the properties of the center of the color group (it must commute with any group generator). Moreover, the adjoint representation acquires a color-symmetric state (additional center). This state is a good candidate for the QCD vacuum.

Pagels and Tomboulis [3] noted that the asymptotic freedom of the quantized Yang–Mills equation leads to an indefinite increase in the effective coupling constant in the infrared region and ultimately to the appearance of the vacuum condensate. This concept was subsequently developed in [4–11]. On the basis of these studies, the following scenario of the formation of vacuum state can be formulated.

Quantum corrections are introduced into the initial Lagrangian

$$L = -F^2/4g^2. \tag{13}$$

The resulting effective Lagrangian has a maximum (energy minimum) for a certain value of $F^2$. This determines the value of the condensate.

The field strength in the Yang–Mills theory,

$$F_{\mu\nu}^a = \partial_\mu A_\nu^a - \partial_\nu A_\mu^a + c^{abc} A_\mu^b A_\nu^c, \tag{14}$$

includes terms with derivatives, which can be conventionally called geometrical terms ($F_{\text{geom}}$), and a term with a structural constant, which will be referred to as the algebraic term ($F_{\text{algebr}}$). Accordingly, the square of the field strength will contain geometric, algebraic, and mixed terms: $\langle F^2 \rangle = \langle F_{\text{geom}}^2 \rangle + \langle F_{\text{algebr}}^2 \rangle + 2\langle F_{\text{geom}} F_{\text{algebr}} \rangle$.

We assume that algebraic terms dominate in the vacuum condensate. This means that the vacuum field in spacetime varies not very rapidly and the interactions of noncommuting components of the potential, which are typical of non-Abelian theory, make the main contribution to the condensate.

The symmetry of vacuum requires that the state must remain unchanged upon a displacement in space-time, rotations, and global group transformations. In the quantum-mechanical approach, this is achieved when the vacuum vector in the Hilbert space (wavefunction) is independent of coordinates, rotations, and group transformations; only the dependence on $F^2$ and probably on other invariants of the symmetry group is admissible. The SU(3) group space is compact so that the wavefunction can be integrated over a seven-dimensional sphere in the eight-dimensional group space. In this case, only the angular variables of the group space vary (as in the nonlinear sigma model). We assume that the time component of the potential is small or zero, which corresponds to the Hamiltonian gauge. Three wavefunctions of the spatial components of the potential form a common wavefunction of the condensate. Such a condensate has the following properties:

$$\langle A_\mu^a \rangle = 0, \quad \langle F_{\mu\nu}^a \rangle = 0,$$
$$\langle F^2 \rangle = \langle F_{\mu\nu}^2 F_{\mu\nu}^a \rangle > 0. \tag{15}$$

These properties coincide with the expected phenomenological properties of the gluon condensate, which may serve as an argument in favor of the model considered here.

It is important for applications to find out whether the above procedure defines the state of vacuum unambiguously or several degenerate states exist. Apparently, degeneracy is present. This follows from analysis of supersymmetric theories [12]; in addition, structural constants have different magnitudes, which may lead to degeneracy in the case of complete symmetry in the fundamental representation.

## 5. CONCLUSIONS

In systems with infinitely large volume, the vacuum of a multicomponent scalar field may preserve the symmetry of the Lagrangian even when the loss of stability leads to the formation of condensate. As a rule, symmetry breaking occurs only under the action of asymmetric forces. Spontaneous symmetry breaking is absent in quantum theory. The presence of quantum effect facilitating the conservation of symmetry does not rule out quantum anomalies leading to the breaking of approximate (e.g., chiral) symmetry. In QCD, the condensate symmetric in the color group and corresponding to an additional discrete group center leads to the degeneracy of the vacuum (two or more phases) and probably to the appearance of additional hadron states.

## REFERENCES

1. J. Goldstone, Nuovo Cimento **9**, 154 (1961); S. Coleman, in *Aspects of Symmetry: Selected Erice Lectures of Sidney Coleman* (Cambridge Univ. Press, Cambridge, 1985).

2. P. W. Higgs, Phys. Rev. **145**, 1156 (1966).

3. H. Pagels and E. Tomboulis, Nucl. Phys. B **143**, 485 (1978).

4. G. K. Savvidy, Phys. Lett. B **71B**, 133 (1977).

5. S. G. Matinyan, Nucl. Phys. B **134**, 539 (1978).

6. I. A. Batalin, S. G. Matinyan, and G. K. Savvidi, Yad. Fiz. **26**, 407 (1977) [Sov. J. Nucl. Phys. **26**, 214 (1977)].

7. V. V. Vladimirskiĭ, Yad. Fiz. **58**, 197 (1995) [Phys. At. Nucl. **58**, 101 (1995)].

8. V. V. Vladimirskiĭ, Yad. Fiz. **59**, 2063 (1996) [Phys. At. Nucl. **59**, 1988 (1996)].

9. V. V. Vladimirskiĭ and D. V. Peregudov, Yad. Fiz. **61**, 573 (1998) [Phys. At. Nucl. **61**, 508 (1998)].

10. V. V. Vladimirskiĭ, Yad. Fiz. **65**, 330 (2002) [Phys. At. Nucl. **65**, 305 (2002)].

11. V. V. Vladimirskiĭ, Yad. Fiz. **66**, 2266 (2003) [Phys. At. Nucl. **66**, 2214 (2003)].

12. E. Witten, Nucl. Phys. B **202**, 253 (1982); M. A. Shifman and A. I. Vainshtein, hep-th/9902018.

*Translated by N. Wadhwa*

# On the Unique Possibility of Significantly Increasing the Contrast of Dark Resonances on the D1 Line of $^{87}$Rb[¶]

## A. V. Taichenachev[a, b], V. I. Yudin[a, b], V. L. Velichansky[c], and S. A. Zibrov[c]

*[a] Novosibirsk State University, Novosibirsk, 630090 Russia*
*[b] Institute of Laser Physics, Siberian Division, Russian Academy of Sciences, Novosibirsk, 630090 Russia*
*[c] Lebedev Physical Institute, Russian Academy of Sciences, Moscow, 117924 Russia*
*e-mail: llf@laser.nsc.ru*
Received July 26, 2005

We propose and study, theoretically and experimentally, a new scheme of excitation of a coherent population trapping resonance for the D1 line of alkali atoms with nuclear spin $I = 3/2$ by bichromatic linearly polarized light (lin‖lin field) under the conditions of spectral resolution of the excited state. The unique properties of this scheme result in a high contrast of dark resonance for the D1 line of $^{87}$Rb. © 2005 Pleiades Publishing, Inc.

PACS numbers: 32.70.Jz, 32.80.Bx, 33.70.Jg, 42.50.Gy

Great attention is drawn to the study of the coherent interaction of atoms with electromagnetic fields. Under specific experimental conditions, coherent atom–field interaction results in what is called the coherent population trapping effect (CPT) [1]. Narrow-width CPT resonances ("dark resonances") induced by this effect are used in atomic clocks [2–4], precise magnetometers [5, 6], laser cooling, spectroscopy, optical signal processing, etc. Most applications require CPT resonance with optimized parameters such as large amplitude, small spectral width, and small background simultaneously. In addition, minimized light shifts are needed in metrology.

Most theoretical and experimental studies of CPT phenomena are made for alkali atoms. CPT resonance is usually observed with a bichromatic field consisting of two resonant laser fields with the frequency difference changing in the vicinity of the hyperfine splitting of the ground state. At exact two-photon resonance, atoms are optically pumped into a coherent nonabsorbing superposition of the ground states, which is called a dark state. A variety of different excitation schemes of CPT resonances were proposed. They differ by the choice of the isotope, excitation line (D1 or D2), and the field characteristics (detuning, amplitude, and polarization of the field components). Different techniques for increasing the coherent atom–field interaction time also play an important role on the build up of ground state coherence. These techniques include the use of a mixture of an alkali vapor with different buffer gases and/or the use of wall-coated cells.

Experiments [7, 8] were carried out with a cell containing a mixture of Cs and a buffer gas and revealed a resonance with a linewidth as small as 50 Hz in the case of D2 line excitation. However, the contrast of the CPT resonance in these experiments was only a small fraction of a percent. In [9] it was shown that using the D1 line instead of D2 line for excitation significantly increases the contrast of the dark resonance. This fact was later confirmed by other authors [10]. In these experiments, resonances were produced by circularly polarized light fields ($\sigma$–$\sigma$) which induced two-photon transitions between magnetic sublevels with the same quantum number $m$ ($m$–$m$ resonances). In atomic clocks, the 0–0 transition is used, because it is first-order insensitive to the magnetic field. The D1 line provides better resonance than the D2 line, since at exact two-photon resonance in the D1 line a dark superposition state exists even when hyperfine components of the excited state are not spectrally resolved due to buffer gas collisional broadening (on the contrary, the D2 line in such a case destroys the dark state via cycling transitions, and the dark state is absent). When the atom–field interaction operator is applied to this state, it yields zero:

$$-(\hat{\mathbf{d}}\mathbf{E})|dark\rangle = 0. \qquad (1)$$

This $|dark\rangle$ state is a coherent superposition of wave functions of the Zeeman sublevels of the ground state. Atoms in this state neither absorb nor emit light.

However, the D1 line has its own limitations. In the case of $\sigma$–$\sigma$ laser fields, a state insensitive to two-photon detuning $|trap\rangle$ exists (in the extreme Zeeman sublevel). A fraction of atoms accumulates in this $|trap\rangle$ state due to optical pumping and does not contribute to the ground state coherence. This fact significantly limits the contrast of the resonance. Thus, to optimize the parameters of the dark resonance, one has to find excitation schemes that on the one hand have a $|dark\rangle$ state and on the other hand do not have a $|trap\rangle$ state.

---

[¶]The text was submitted by the authors in English.

Recently, this problem was solved for *m*–*m* resonances on the D1 line. Different approaches for optimizing the parameters of the dark resonance were proposed in [11–13] for the case of 0–0 resonance. A general case of arbitrary *m*–*m* resonance is investigated in [14].

In this paper, we propose an alternative method of forming high-contrast dark resonances by a bichromatic light field with arbitrary polarizations (in the general case, elliptical). This method works only in the special case when the total angular moments of the ground states are $F_g = 1, 2$ and the coupling occurs through an excited state with a total angular momentum of $F_e = 1$. Additionally, a key requirement here is a good spectral resolution of the excited hyperfine levels. Such a situation is realized for the D1 line of $^{87}$Rb, because hyperfine splitting of the excited state in this case is 812 MHz and is considerably larger than the Doppler width of the line (~400 MHz). A CPT resonance involves in this case two pairs of Zeeman sublevels whose magnetic quantum numbers differ by two: (–1)–(+1) and (+1)–(–1). At exact two-photon resonance, the dark superposition states exist, while the extra trapping state $|trap\rangle$ is absent. The same situation occurs with field-sensitive resonances (+1)–(+1) and (–1)–(–1), which also have high contrast in this case. Special attention is drawn to the case of the lin‖lin configuration of optical fields, in which the frequency components have the same linear polarizations. It should be noted that, due to the nuclear contribution of the *g* factor of different ground-state hyperfine components, the resonances (–1)–(+1) and (+1)–(–1) have a weak linear sensitivity to a magnetic field. However, for the lin‖lin light field configuration, owing to the symmetry, this effect manifests itself mostly in a small broadening of the resonance line shape. It is important that the center of the resonance has zero linear sensitivity to a magnetic field. Qualitative theoretical analysis is proved by experiments which demonstrate a very high contrast of the dark resonance in the case of a lin‖lin field. The influence of nuclear spin, which leads to the broadening and splitting of the resonance, is studied.

## QUALITATIVE THEORETICAL ANALYSIS

Let us consider the resonant interaction of atoms with a bichromatic field consisting of two copropagating (along the *z* axis) running waves

$$\mathbf{E}(z, t) = \mathbf{E}_1(z)e^{-i\omega_1 t} + \mathbf{E}_2(z)e^{-i\omega_2 t} + \text{c.c.} \quad (2)$$

The two components of this field have arbitrary amplitudes and polarizations (elliptical in the general case). The polarization can be represented as a linear combination of two orthogonal circular components ($\mathbf{e}_{\pm 1} = \mp(\mathbf{e}_x \pm i\mathbf{e}_y)/\sqrt{2}$) in the following way:

$$\mathbf{E}_j = E_{-1}^{(j)}\mathbf{e}_{-1} + E_{+1}^{(j)}\mathbf{e}_{+1} \quad (j = 1, 2). \quad (3)$$

A small static longitudinal magnetic field **B** is applied along the *z* axis of the coordinate system. When the frequency difference $(\omega_1 - \omega_2)$ of the bichromatic field components is equal to the hyperfine splitting of the ground state $\Delta_{hfs}$, this field induces a two-photon dark resonance of a $\Lambda$ type on two hyperfine levels of the ground state.

Let us take into account only the alkali atoms with a nuclear spin number $I = 3/2$ ($^7$Li, $^{23}$Na, $^{39, 41}$K and $^{87}$Rb). The total angular momenta of the hyperfine components of the ground state for these atoms are $F_g = 1, 2$. We consider the case when both frequency components of the bichromatic field are resonant with the common excited state with a total angular momentum $F_e = 1$. The excitation scheme for this case is shown in Fig. 1a.

Figure 1a shows that a two-photon resonance of a $\Lambda$ type is formed in two pairs of ground-state hyperfine sublevels with $|F_g = 1, m = -1\rangle$, $|F_g = 2, m = +1\rangle$ and $|F_g = 1, m = +1\rangle$, $|F_g = 2, m = -1\rangle$. Further in the paper, we will call them (–1)–(+1) and (+1)–(–1) resonances. Both of these $\Lambda$ schemes are excited through a common excited state $|F_e = 1, m = 0\rangle$. It is known that, for alkali atoms, the *g* factors of different hyperfine levels of the ground state have an equal absolute value and opposite signs (in our case, $g = \pm 1/2$). If the contribution of the nuclear spin to the Zeeman splitting is neglected, then two-photon resonance frequencies (both (–1)–(+1) and (+1)–(–1)) are equal to the frequency of the 0–0 resonance formed on $|F_g = 1, m = 0\rangle$ and $|F_g = 2, m = 0\rangle$ states. This fact means that at least two superposition dark states exist in the case of exact two-photon resonance for fields with arbitrary polarizations. These states are determined by the abovementioned $\Lambda$ schemes:

$$|dark(\pm)\rangle$$

$$= N_{\pm}\left\{|F_g = 1, m = \mp 1\rangle - \frac{V_{\pm 1}^{(1)}E_{\pm 1}^{(1)}}{V_{\mp 1}^{(2)}E_{\mp 1}^{(2)}}|F_g = 2, m = \pm 1\rangle\right\}. \quad (4)$$

Here, $V_{\pm 1}^{(1, 2)}$ are the corresponding matrix elements of the dipole moment operator (Fig. 1a); $N_{\pm}$ are the normalization constants. In this general case, the $|trap\rangle$ state is absent. This fact allows a high-contrast resonance to form. It is worth mentioning that the resonance shift due to the second-order magnetic field dependence in the case of this scheme of excitation is 1.33 times smaller than for the true 0–0 resonance in the case of the traditional excitation scheme.

States given by (4) do not appear in any other scheme of excitation of the dark resonance. For example, Fig. 1b illustrates the situation when excitation occurs through an excited state with $F_e = 2$. Here, ground state levels $|F_g = 1, m = \pm 1\rangle$ and $|F_g = 2, m = \pm 1\rangle$ are coupled with the excited states $|F_e = 2, m = \pm 2\rangle$. These transitions destroy the dark states. For atoms with other quantum numbers of total angular momen-
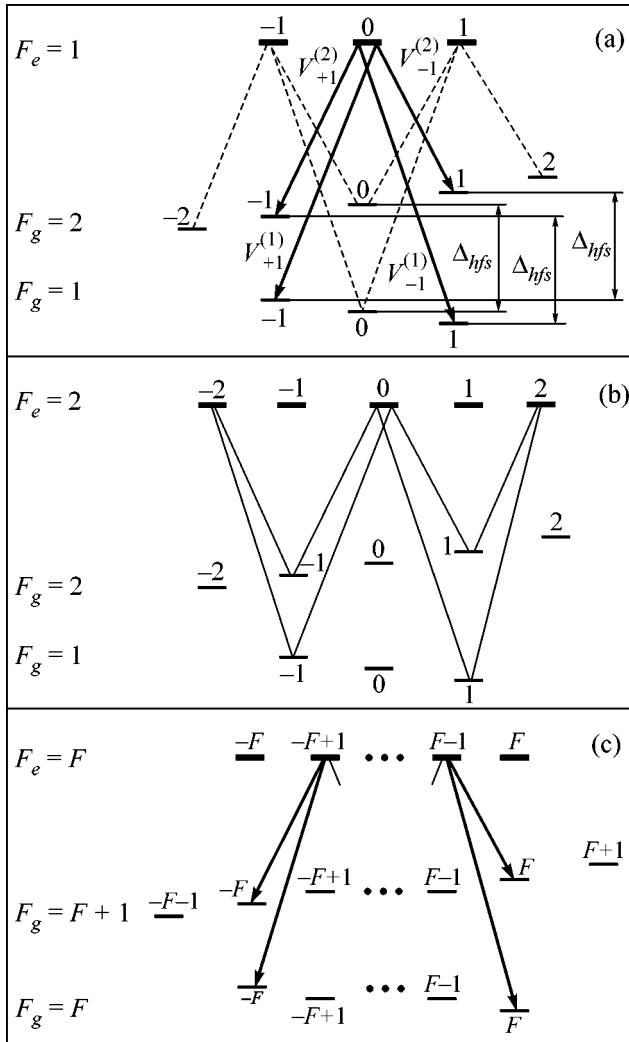
**Fig. 1.** Schemes of the light-induced transitions in a bichromatic field with arbitrary (elliptical in general) polarizations for different variants of excitation: (a) the unique case of $F_g = 1, 2$ at excitation via $F_e = 1$, when simple $\Lambda$ systems are realized for Zeeman sublevels with different magnetic quantum numbers $m = \pm 1$ (solid arrows); (b) the case of $F_g = 1, 2$ at excitation via $F_e = 2$, when simple $\Lambda$ systems are absent; (c) the general case of $F_g = F, F + 1$ at excitation via $F_e = F$, when the outermost magneto-sensitive resonances are formed through simple $\Lambda$ systems (solid arrows) for arbitrary (elliptical in general) polarizations.

tum $F_g$ (i.e., for those that have $I \neq 3/2$), dark states (4) are not induced for any given $F_e$.

Thus, alkali atoms with a nuclear spin of $I = 3/2$ are of great interest due to the new possibilities for forming high-contrast magneto-insensitive dark resonances with arbitrarily polarized light fields. However, the key requirement of good spectral resolution of the excited state $F_e = 1$ determines the choice of atom and transition. Most promising is the D1 line of $^{87}$Rb, because the hyperfine splitting of the excited state is equal to 812 MHz. This fact allows its use in cells at room tem-

perature. For all other alkali atoms ($^7$Li, $^{23}$Na, $^{39, 41}$K) with similar structure, and also for the D2 line of $^{87}$Rb, good spectral resolution of the excited state can be reached only in the case of laser-cooled atoms or in a collimated atomic beam.

We focus our attention on the case of lin‖lin polarizations of the light fields, where both resonant fields have equal linear polarizations. For this excitation scheme, the $|trap\rangle$ state does not exist. Also, it is experimentally easy to create such a linear polarized field using one laser source. In addition, this situation is preferable if the influence of nuclear spin on the splitting of levels is taken in account. Nuclear spin leads to a small difference in the absolute values of $g$ factors for different hyperfine components of the ground state. As a result of this mismatch of $g$ factors, the frequencies of the $(-1)$–$(+1)$ and $(+1)$–$(-1)$ two-photon $\Lambda$ resonances are also different (for $^{87}$Rb, this difference is 2.8 kHz/G), but their position is symmetrical relatively to the hyperfine splitting frequency $\Delta_{hfs}$. Thus, in case of the lin‖lin excitation scheme in the presence of a small magnetic field, this fact leads only to the broadening of the resonance and not to its shift (in the linear approximation), because both $\Lambda$ systems are identical for the lin‖lin field. Also, it is worth mentioning that the true 0–0 resonance in the case of lin‖lin excitation is absent due to the destructive interference of two-photon transitions induced by different components of the circularly polarized light.

Let us mention another interesting peculiarity of the excitation scheme through the $F_e = 1$ excited state. As can be seen in Fig. 1a, two field sensitive resonances $(-1)$–$(-1)$ and $(+1)$–$(+1)$, formed on levels with the same $m$ quantum number, are also excited in $\Lambda$-type schemes. For these $\Lambda$ schemes, dark states exist at exact two-photon resonance. This means that these resonances can also have large contrasts. This situation takes place for the D1 line not only in the case of nuclear spin $I = 3/2$ but in the more general case of $F_g = F, F + 1$ as well, when resonant interaction of the two-frequency field (2) occurs through the level with $F_e = F$. As can be seen from Fig. 1c, interaction between $|F_g = F, m = -F\rangle$ and $|F_g = F + 1, m = -F\rangle$, and also between $|F_g = F, m = F\rangle$ and $|F_g = F + 1, m = F\rangle$, occurs by the $\Lambda$-type scheme of excitation with arbitrary polarizations. Thus, resonances sensitive to the magnetic field $(-F)$–$(-F)$ and $(F)$–$(F)$ can also have large contrast. For example, for $^{133}$Cs atoms ($I = 7/2$), they will be $(-3)$–$(-3)$ and $(+3)$–$(+3)$ resonances under excitation through the level with $F_e = 3$.

The given qualitative description is confirmed by numerical calculations and experiment.

## EXPERIMENT

Figure 2 shows the schematic of the experimental setup. This includes a laser system providing bichro-
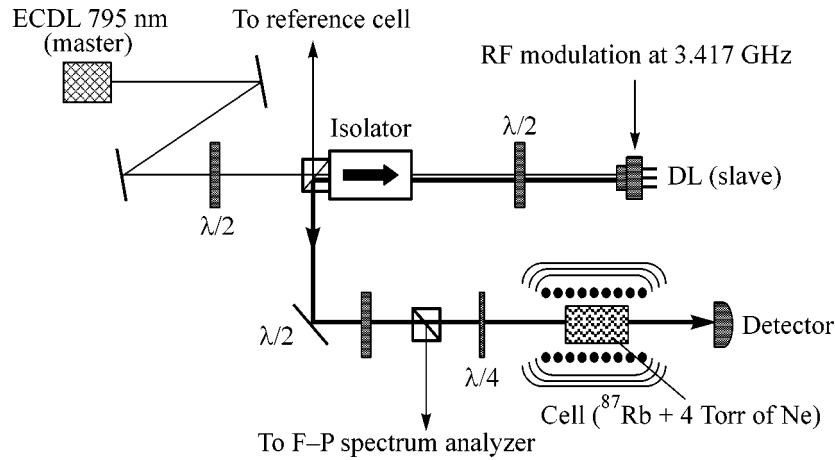
**Fig. 2.** Experimental setup. Cell contains $^{87}$Rb and 4 Torr of Ne buffer gas.

matic radiation, a heated cell with alkali metal vapor, and a signal detection scheme. The experiment was carried out with a Pyrex cylindrical cell (40 mm long and 25 mm in diameter) containing isotopically enriched $^{87}$Rb and 4 Torr Ne buffer gas. The cell was placed inside a solenoid that provided a longitudinal magnetic field of 150 mG to lift the degeneracy of the Zeeman sublevels and to separate magneto-insensitive "clock" resonance, which has no first-order magnetic field dependence, from the field-dependent resonances. The solenoid was placed within three concentric μ-metal shields in order to reduce the influence of external magnetic fields. The cell was heated by bifilar wire wrapped around the inner layer of the magnetic shielding. For the experiments reported here, the cell temperature was 50°C.

In order to obtain a bichromatic light field, we modulated the injection current of a diode laser. This was done in the following way: a slave diode laser, operating in the vicinity of 795 nm, was injection-locked by the radiation of a single mode extended cavity diode laser (ECDL), and at the same time its current was frequency-modulated at 3.417 GHz. This technique produced phase-correlated narrow-line-width optical fields and allowed easy tuning of these fields to the desired transitions. Also, it allowed the resonant field's intensity ratio to be varied by changing the current of the injection-locked diode laser. For the experiments reported here, approximately 25% of the total laser power was transferred to each first-order sideband, with the remainder residing in the carrier and high-order sidebands. The laser's injection current was frequency-swept.

In the case of the lin‖lin excitation scheme, CPT resonance was formed by two linearly polarized first-order sidebands tuned to the $F_g = 1 \longrightarrow F_e = 1$ and $F_g = 2 \longrightarrow F_e = 1$ transitions. In the case of the σ–σ excitation scheme, these fields were circularly polarized and tuned to the $F_g = 1 \longrightarrow F_e = 2$ and $F_g = 2 \longrightarrow$

$F_e = 2$ transitions. The laser beam passed a quarter-wave plate situated so as to leave the polarization of light unchanged (linear) or to make it circular, depending on the excitation scheme being studied. The optical power transmitted through the gas cell was then detected by a silicon photodiode.

We performed a comparative study of two different excitation schemes of CPT resonance. CPT resonance observed by use of different excitation schemes under the same experimental conditions are shown in Fig. 3. Lines are vertically shifted for ease of visual perception. It is clearly seen from this figure that the amplitude of the clock resonance in case of the lin‖lin scheme of excitation through $F_e = 1$ is much larger than in the case of σ–σ excitation through $F_e = 2$ and lin‖lin excitation through $F_e = 2$. The amplitude, the amplitude-to-width
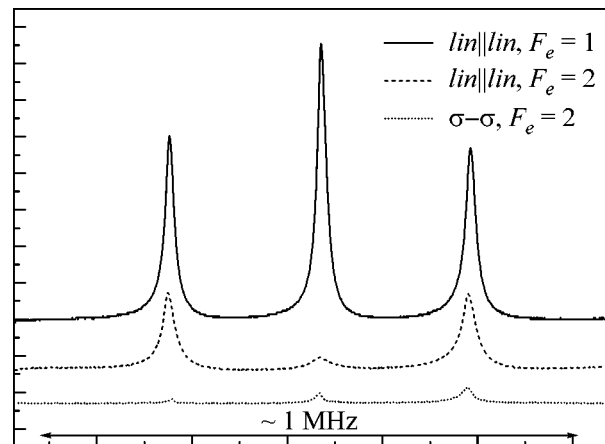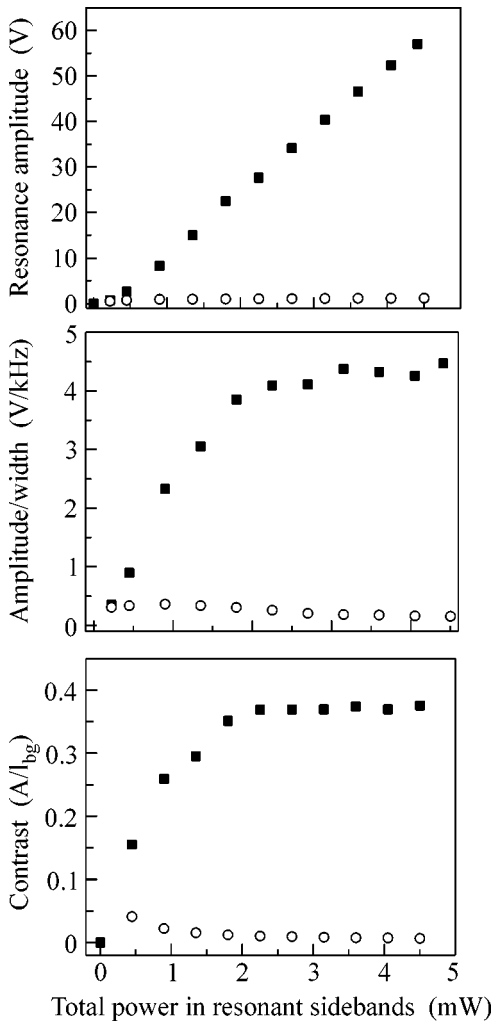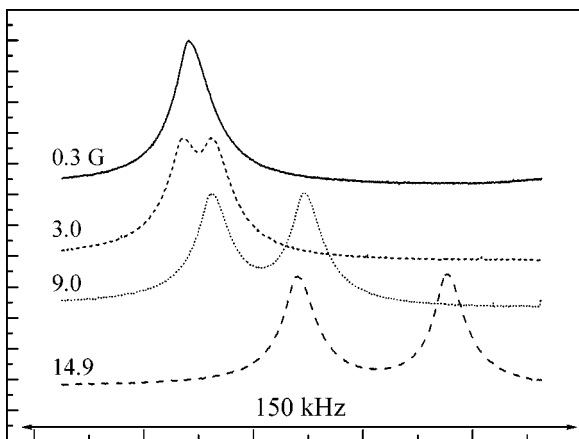


**Fig. 3.** OPT resonances (in transmission) for different excitation schemes; pressure of the buffer gas Ne at 4 Torr; cell temperature $T = 50°$; diameter of the laser beam $D = 5$ mm; the total power in sidebands, 2.5 mW.

**Fig. 4.** Amplitude, amplitude-to-width and contrast of the CPT resonance in case of lin∥lin ($F_e = 1$, black squares) and σ–σ ($F_e = 2$, circulars) excitation schemes.



**Fig. 5.** CPT resonances for lin∥lin excitation ($F_e = 1$) at different values of applied longitudinal magnetic field.

ratio, and the contrast of the resonance for different excitation schemes are shown in Fig. 4.

Figure 5 shows the behavior of the clock CPT resonance in the case of lin∥lin excitation scheme through $F_e = 1$ at different values of applied longitudinal magnetic field. For small magnetic fields, this leads to broadening of the resonance and does not change the position of its maximum (in the linear approximation). At large magnetic fields, the resonance is eventually split into two components because of the difference in absolute values of the $g$ factors for the two hyperfine levels. The center of the resonance line shape is shifted due to the quadratic Zeeman effect. It should be noted that the double structure has been observed previously [15, 16]. However, the observed resonance amplitudes were very small, because other excitation schemes were used: the D2 line of Cs in [15] and the D1 line of $^{87}$Rb at higher buffer gas pressure in [16]. Recently it was proposed to use the gap between two peaks to lock the frequency in an atomic clock [17].

Thus, in the present paper, we have proposed and experimentally realized a new scheme of excitation of the D1 line of alkali atoms with nuclear spin $I = 3/2$ with a bichromatic lin∥lin field. This allows us to significantly increase the contrast of the magneto-insensitive dark resonance in comparison with the standard excitation of the 0–0 resonance with the bichromatic circular polarized field. Under usual conditions, such a possibility exists only for $^{87}$Rb, when the exited-state hyperfine levels are spectrally resolved. In addition, in this case the magneto-sensitive $m$–$m$ resonances with maximal $|m|$ have the highest contrast. The obtained results indicate that the D1 line of $^{87}$Rb under excitation through the level with $F_e = 1$ is a special object of study for an atomic clock and magnetometer based on CPT. These results were first presented in part at ICONO'05 [18].

## REFERENCES

1. E. Arimondo, in *Progress in Optics*, Ed. by E. Wolf (North-Holland, Amsterdam, 1996), Vol. 35, p. 257.

2. P. R. Hemmer, S. Ezekiel, and C. C. Leiby, Opt. Lett. **8**, 440 (1983).

3. J. Kitching, S. Knappe, N. Vukicevic, *et al.*, IEEE Trans. Instrum. Meas. **49**, 1313 (2000).

4. L.-A. Liew, S. Knappe, H. Robinson, *et al.*, Appl. Phys. Lett. **84**, 2694 (2004).

5. M. Stahler, S. Knappe, C. Affolderbach, *et al.*, Europhys. Lett. **54**, 323 (2001).

6. P. D. D. Schwindt, S. Knappe, V. Shah, *et al.*, Appl. Phys. Lett. **85**, 6409 (2004).

7. S. Brandt, A. Nagel, R. Wynands, and D. Meschede, Phys. Rev. A **56**, R1063 (1997).

8. R. Wynands and A. Nagel, Appl. Phys. B **68**, 1 (1999).

9. M. Stahler, R. Wynands, S. Knappe, *et al.*, Opt. Lett. **27**, 1472 (2002).

10. J. Vanier, M. W. Levine, D. Janssen, *et al.*, Phys. Rev. A **67**, 065 801 (2003).

11. A. V. Taichenachev, V. I. Yudin, V. L. Velichansky, *et al.*, Pis'ma Zh. Éksp. Teor. Fiz. **80**, 265 (2004) [JETP Lett. **80**, 236 (2004)].

12. Y.-Y. Jau, E. Miron, A. B. Post, *et al.*, Phys. Rev. Lett. **93**, 160 802 (2004).

13. T. Zanon, S. Guerandel, E. de Clercq, D. Holleville, N. Dimarcq, and A. Clairon, Phys. Rev. Lett. **94**, 193 002 (2005).

14. A. V. Taichenachev, V. I. Yudin, V. L. Velichansky, and S. A. Zibrov, quant-ph/0503036 v2 (2005).

15. S. Knappe, W. Kemp, C. Affolderbach, *et al.*, Phys. Rev. A **61**, 012 508 (2000).

16. A. Godone, F. Levi, and S. Micalizio, *Coherent Population Trapping Maser* (CLUT, Torino, 2002).

17. G. Kazakov, B. Matisov, I. Mazets, *et al.*, quant-ph/0506167 v2.

18. S. A. Zibrov, Y. O. Dudin, V. L. Velichansky, *et al.*, in *Abstract Book of ICONO'05* (St. Petersburg, 2005), p. ISK8.

# Loss of Electrons from Fast Heavy Structure Ions Colliding with Atoms

**V. I. Matveev[a], D. U. Matrasulov[b], and S. V. Ryabchenko[c]**

*[a] Lomonosov Pomor State University, Arkhangel'sk, 163002 Russia*
*e-mail: matveev.victor@pomorsu.ru*
*[b] Department of Thermal Physics, Academy of Sciences of Uzbekistan, Tashkent, 700135 Uzbekistan*
*[c] Arkhangel'sk State Technical University, Arkhangel'sk, 163002 Russia*
Received August 3, 2005; in final form, August 22, 2005

Nonperturbative theory is developed for the multiple ionization of fast heavy structure ions colliding with neutral complex atoms. The cross sections for multiple loss of electrons by structure uranium ions $U^{10+}$ (loss of up to 82 electrons) and $U^{28+}$ (loss of up to 64 electrons) colliding with argon atoms are calculated. The results are compared with available experimental data. © 2005 Pleiades Publishing, Inc.

PACS numbers: 34.10.+x, 34.90.+q

Partially stripped high-energy multicharged ions are used in many experiments at heavy ion accelerators (see, e.g., [1–3] and references therein). Such ions consist of a nucleus and bound electrons. Strictly speaking, the collisions of such structure ions with atoms should be considered as the collision of two complex systems that is accompanied by the simultaneous excitation of electron shells of both colliding systems. In what follows, the moving structure ion and atom at rest are called projectile and target, respectively. Interest in multiple ionization, i.e., the stripping of the projectile in the collisions of heavy ions with neutral atoms, of increasing recently. In particular, in [1, 2], the cross sections for multiple ionization (loss of up to 15 electrons) of fast uranium ions colliding with multielectron neutral atoms were measured and the necessity of calculation of such processes by nonperturbative methods was pointed out. In [2], the cross sections for the multiple ionization of the projectile were calculated by nonperturbative methods. Quantum-mechanical nonperturbative consideration of the multiple ionization of the projectile has not yet been performed. The primary reason is the large number of electrons involved in the inelastic collision. For example, the total number of electrons is about 100 for the collision of the $U^{10+}$ ion with the argon atom. Therefore, it is necessary to numerically calculate a great number of multiple integrals, which seems extremely difficult even with current computational capabilities. In this situation, it is reasonable to develop a theory where the problem is treated as significantly multiparticle. In this work, we develop the nonperturbative theory of multiple ionization accompanying collisions of fast heavy structure ions with neutral complex atoms, perform calculations, and compare the results with experiment.

It is convenient to consider that the projectile is at rest at the coordinate origin and the target rectilinearly moves with constant velocity $\mathbf{v}$; i.e., the coordinates of the nucleus of the target atom are $\mathbf{R} = \mathbf{b} + \mathbf{v}t$, where $\mathbf{b}$ is the impact parameter and $t$ is the time. In order to simplify formulas, we suppose that each of projectile and target has one electron (generalization to multielectron colliding systems will be made below). Let $\mathbf{r}_p$ be the coordinates of the electron of the structure projectile ion with respect to the projectile nucleus and $\mathbf{r}_a$ be the coordinates of the electron of the target atom with respect to the target nucleus. The potential of the interaction between the projectile and target has the form (hereinafter, the atomic units are used)

$$
V(\mathbf{r}_a, \mathbf{r}_p, t) = -\frac{Z_p}{|\mathbf{R}(t) + \mathbf{r}_a|} - \frac{Z_a}{|\mathbf{R}(t) - \mathbf{r}_p|} + \frac{1}{|\mathbf{R}(t) + \mathbf{r}_a - \mathbf{r}_p|}, \tag{1}
$$

where $Z_p$ and $Z_a$ are the charges of the nuclei of the projectile and target, respectively, and the internuclear interaction is disregarded, because it does not induce electron transitions. The electronic states of the isolated target and isolated projectile are described by the complete sets of wave functions $\varphi_n(\mathbf{r}_a)$ and $\psi_k(\mathbf{r}_a)$, respectively. Correspondingly, the initial and final states of the colliding systems have the form $\Phi_{00} = \psi_0(\mathbf{r}_p)\varphi_0(\mathbf{r}_a)$ and $\Phi_{kn} = \psi_k(\mathbf{r}_p)\varphi_n(\mathbf{r}_a)$, respectively. In what follows, similar to [4, 5], we assume that the relative collision velocity $v$ is high and thereby perturbation (1) acts suddenly. The corresponding conditions are as follows. The time of the collision between the projectile and target is $\tau_c \sim a/v$, where $a \sim 1$ is the characteristic size of the colliding systems, and the characteristic time $\tau_s$ of the revo-

lution of electrons in an orbit should be taken ~1 for the electrons of both the projectile and target, because the aim of our consideration is collisions of multielectron systems, where most electrons are on upper shells with large quantum numbers. Thus, for the applicability of the sudden-perturbation approximation, $\tau_c \ll \tau_s$, it is sufficient to satisfy the inequality $v \gg 1$ in the case of interest. In the sudden-perturbation approximation, the amplitude of the collision-induced transition of the target-atom electron from the state $\varphi_0(\mathbf{r}_a)$ to the state $\varphi_n(\mathbf{r}_a)$ and the projectile electron from the state $\psi_0(\mathbf{r}_p)$ to the state $\psi_k(\mathbf{r}_p)$ is given by the expression [6, 7]

$$A_{0 \to k}^{0 \to n} = \left\langle \Phi_{kn} \left| \exp\left(-i \int_{-\infty}^{+\infty} V(\mathbf{r}_a, \mathbf{r}_p, t)dt\right) \right| \Phi_{00} \right\rangle. \quad (2)$$

The corresponding probability is equal to $w_{0 \to k}^{0 \to n} = |A_{0 \to k}^{0 \to n}|^2$. We are interested in the transitions accompanied by simultaneous change in the target state and projectile state and the probability of certain transitions in the projectile for an arbitrary (unfixed) final state of the target. For this reason, we sum over all finite states (complete set) of the target and, taking into account the completeness condition for the set of the functions $\varphi_n(\mathbf{r}_a)$, obtain

$$W_{0 \to k}(\mathbf{b}) = \sum_n w_{0 \to k}^{0 \to n} = \int d^3\mathbf{r}_a |\varphi_0(\mathbf{r}_a)|^2$$
$$\times \left| \int d^3\mathbf{r}_p \psi_k^*(\mathbf{r}_p) \exp\left(-i \int_{-\infty}^{+\infty} U_a(\mathbf{r}_a, \mathbf{r}_p, t)dt\right) \psi_0(\mathbf{r}_p) \right|^2. \quad (3)$$

Here, the part $U_a(\mathbf{r}_a, \mathbf{r}_p, t)$ of the potential $V(\mathbf{r}_a, \mathbf{r}_p, t)$ corresponds to the second and third terms in Eq. (1) and is equal to the potential describing the action of the target on the electron of the bombarding ion. Thus, we obtain the probability $W_{0 \to k}(\mathbf{b})$ of the transition of the projectile electron from the state $\psi_0$ to the state $\psi_k$ as a function of the impact parameter $\mathbf{b}$ as summed over all final states of the target atom. The corresponding excitation cross section is obtained by integrating the probability $W_{0 \to k}(\mathbf{b})$ over the entire plane of the impact parameter $\mathbf{b}$.

Let us consider inelastic processes in collisions of a multielectron structure ion having $N_p$ electrons with a complex multielectron atom having $N_a$ electrons. The potential $U_a(\{\mathbf{r}_a\}, \{\mathbf{r}_p\}, t)$ describing the action of the atom (target) on the electrons of the bombarding ion is a function not only of the relative coordinates $\mathbf{R} = (vt, \mathbf{b})$ of the nuclei of the projectile and target but also of the positions $\{\mathbf{r}_a\}$ of all electrons of the target and the positions $\{\mathbf{r}_p\}$ of all electrons of the projectile. The corresponding natural generalization of Eq. (3) to the case of the transition of the projectile electrons from the ground state $|\Psi_0(\{\mathbf{r}_p\})\rangle$ to an arbitrary excited state

$|\Psi_n(\{\mathbf{r}_p\})\rangle$ for an arbitrary final state of the target atom has the form

$$W_{0 \to n}(\mathbf{b}) = \langle \varphi_0(\{\mathbf{r}_a\})|$$
$$\times \left| \left\langle \Psi_n \left| \exp\left(-i \int_{-\infty}^{+\infty} U_a(\{\mathbf{r}_a\}, \{\mathbf{r}_p\}, t)dt\right) \right| \Psi_0 \right\rangle \right|^2 |\varphi_0(\{\mathbf{r}_a\})\rangle. \quad (4)$$

The direct use of this formula is difficult when the projectile and target are fundamentally multielectron; i.e., $N_a \gg 1$ and $N_p \gg 1$. However, this circumstance allows the following simplification. During the collision time, the position of electrons in the target does not change with respect to the nucleus of the target. When the numbers of electrons in the target and projectile are large, it is natural to assume that the potential describing the action of the atom (target) on the electrons of the bombarding ion (projectile) is the average of the potential $U_a(\{\mathbf{r}_a\}, \{\mathbf{r}_p\}, t)$ over the initial ground state of the electrons of the target. We suppose that the states of electrons in the target are described [8] by the single-electron orbitals in the mean self-consistent field in the Dirac–Hartree–Fock–Slater model. In this case, the screening function for neutral atoms with atomic numbers $Z_a = 1$–92 can be written in a simple analytical form [8]. Correspondingly, the potential describing the action of the target on the electrons of the projectile can be represented in the form

$$U_a(\{\mathbf{r}_a\}, \{\mathbf{r}_p\}, t) = -\sum_{p=1}^{p=N_p} \frac{Z_a}{|\mathbf{R}(t) - \mathbf{r}_p|}$$
$$\times \sum_{i=1}^{i=3} A_i e^{(-\alpha_i)|\mathbf{R}(t) - \mathbf{r}_p|}, \quad (5)$$

where $A_i$ and $\alpha_i$ are the constants tabulated in [8] for all elements. Thus, the potential $U_a$ in Eq. (4) is independent of the coordinates $\{\mathbf{r}_a\}$ of the electrons in the target and, since $\langle \varphi_0(\{\mathbf{r}_a\})|\varphi_0(\{\mathbf{r}_a\})\rangle = 1$, probability (4) of the transition of the electrons of the projectile from the ground state $|\Psi_0(\{\mathbf{r}_p\})\rangle$ to an arbitrary excited state $|\Psi_n(\{\mathbf{r}_p\})\rangle$ for an arbitrary final state of the target atom is given by the simple expression

$$W_{0 \to n}(\mathbf{b})$$
$$= \left| \left\langle \Psi_n(\{\mathbf{r}_p\}) \left| \exp\left(-i \sum_{p=1}^{p=N_p} \chi(\mathbf{b}, \mathbf{r}_p)\right) \right| \Psi_0(\{\mathbf{r}_p\}) \right\rangle \right|^2. \quad (6)$$

Here,

$$\chi(\mathbf{b}, \mathbf{r}_p) = -\frac{Z_a}{v} \sum_{i=1}^{i=3} A_i K_0(\alpha_i |\mathbf{b} - \mathbf{s}_p|) \quad (7)$$

is the eikonal phase, where $\mathbf{s}_p$ is the projection of $\mathbf{r}_p$ onto the plane of the impact parameter $\mathbf{b}$. In other words (cf. [9]), expression (6) is the probability of exciting the

structure projectile ion that is at rest at the coordinate origin by the neutral target atom with velocity **v** and is described as an extended object with the spatially inhomogeneous charge density. Following the procedure presented in [9], the desired probability for exciting atoms by extended relativistic charges can be obtained in the eikonal approximation applied to the problem under consideration. Thus, Eq. (6) is also applicable for collisions between the relativistic projectile and target when the electrons of the projectile are nonrelativistic in the projectile reference frame before and after the collision (the same requirement concerns the electrons of the target in its reference frame). The further analysis follows the scheme that was developed in [10] for describing the collisions between multicharged heavy ions with complex atoms and was successfully applied in [11, 12] to calculate the cross section for the multiple (up to 18) ionization of Ar and Ne atoms by high-energy multicharged uranium ions. The electrons of the projectile are treated as distinguishable and nonrelativistic in the projectile reference frame before and after the collision. Each electron is described by a single-electron hydrogenlike wave function. In this case, the initial and final wave functions have the form $\Psi_0(\mathbf{r}_1, \ldots, \mathbf{r}_{N_p}) = \prod_{i=1}^{N_p} \phi_i(\mathbf{r}_i)$ and $\Psi_f(\mathbf{r}_1, \ldots, \mathbf{r}_{N_p}) = \prod_{i=1}^{N_p} \psi_i(\mathbf{r}_i)$, respectively. Therefore, in view of the unitarity of probability (6), the total probability of the $(N_p - N)$-multiple ionization of the nonrelativistic $N_p$-electron structure ion from which $N_p - N$ electrons appear in continuum and other $N$ electrons, in any states of the discrete spectrum, is given by the expression (cf. [11, 12])

$$
W^{(N_p - N)+}(\mathbf{b}) = \frac{N_p!}{(N_p - N)!N!}
$$
$$
\times \prod_{i=1}^{N_p - N} p_i(\mathbf{b}) \prod_{j=N_p - N + 1}^{N_p} (1 - p_j(\mathbf{b})). \tag{8}
$$

Here, $\prod_{j=N_p - N + 1}^{N_p} (\ldots) = 1$ for $N = 0$ and the generalized single-electron inelastic form factor is represented as

$$
p_i(\mathbf{b}) = \int d^3 k_i
$$
$$
\times \left| \int d^3 r_i \psi_{\mathbf{k}_i}^*(\mathbf{r}_i) \exp\{-i\chi_i(\mathbf{b}, \mathbf{r}_i)\} \phi_i(\mathbf{r}_i) \right|^2, \tag{9}
$$

where $\mathbf{k}_i$ is the momentum of the $i$th electron in continuum. Similar to [11, 12], we introduce projectile-shell-averaged generalized single-electron inelastic form factor $p(b)$, which has the meaning of the average probability of single-electron ionization. Then, changing each single-electron form factor by $p(b)$, we obtain the probability of the complete ionization of the projectile in the form $W^{N_p+} = [p(b)]^{N_p}$, where $b \equiv b Z_{N_p}^*$ and $Z_{N_p}^*$

is the effective charge of the nucleus of the projectile that corresponds to the complete ionization of the projectile, and the following general expression for the probability of the ionization of $N_p - N$ electrons:

$$
W^{(N_p - N)+}(b) = \frac{N_p!}{(N_p - N)!N!}
$$
$$
\times \sum_{m=0}^{N} (-1)^m \frac{N!}{(N-m)!m!} \{p(b)\}^{N_p - N + m}. \tag{10}
$$

Here, the term with $\{p(b)\}^{N_p - N + m}$ corresponds to $(N_p - N + m)$-multiple ionization and $b \equiv b Z_{N_p - N + m}^*$ in it, where $Z_{N_p - N + m}^*$ is the effective charge for $(N_p - N + m)$-multiple ionization. In order to obtain the cross section for $(N_p - N)$-electron ionization, it is necessary to integrate probability (10) over the entire plane of the impact parameter

$$
\sigma^{(N_p - N)+} = 2\pi \int_0^\infty W^{(N_p - N)+}(b) b\, db. \tag{11}
$$

In order to calculate the integral, it is necessary to know the function $p(b)$. It seems very difficult to calculate this function when the number of electrons on the ion shells is large (e.g., when considering the multiple ionization of the $U^{10+}$ projectile colliding with the neutral argon or xenon atom). However, for ionization of high multiplicity $N_p \gg 1$, where $N_p - N \gg 1$, which will be considered below, the problem can be simplified using the procedure proposed in [10–12]. The integral with respect to the impact parameter in Eq. (11) with probability (10) can be calculated asymptotically by the Laplace method under the assumption that $p(b)$ has a maximum located inside or at the left boundary $b = 0$ of the integration interval. Indeed, it is reasonable to consider that the probability of ionization in collision with the neutral atom is maximal when the impact parameter is close or equal to zero. For this reason, we accept the standard assumptions [13] concerning the properties of the function $p(b)$ for the applicability of the Laplace method. First, we write $[p(b)]^N = \exp[N\ln(p(b))] = \exp[Nf(b)]$. Then, for $N \gg 1$, according to [13],

$$
\int_{b_0}^{b_1} e^{-Nf(b)} g(b)\, db \sim \frac{G}{\mu} \Gamma\left(\frac{\lambda}{\mu}\right) e^{-Nf(b_0)} \left[\frac{1}{FN}\right]^{\lambda/\mu}, \tag{12}
$$

where $\Gamma(x)$ is the gamma function and $G$, $\mu$, $\lambda$, and $F$ are the numbers determined by the behavior of the functions $f(b)$ and $g(b)$ near the maximum point $b_0$: $f(b) - f(b_0) \sim F(b - b_0)^\mu$, $g(b) \sim G(b - b_0)^{\lambda - 1}$. According to Eq. (11), the function $g(b)$ appears when integrating over the entire plane of the impact parameter and, if $b_0 \neq 0$, $g(b) = b$, which corresponds to $G = b_0$ and $\lambda = 1$.
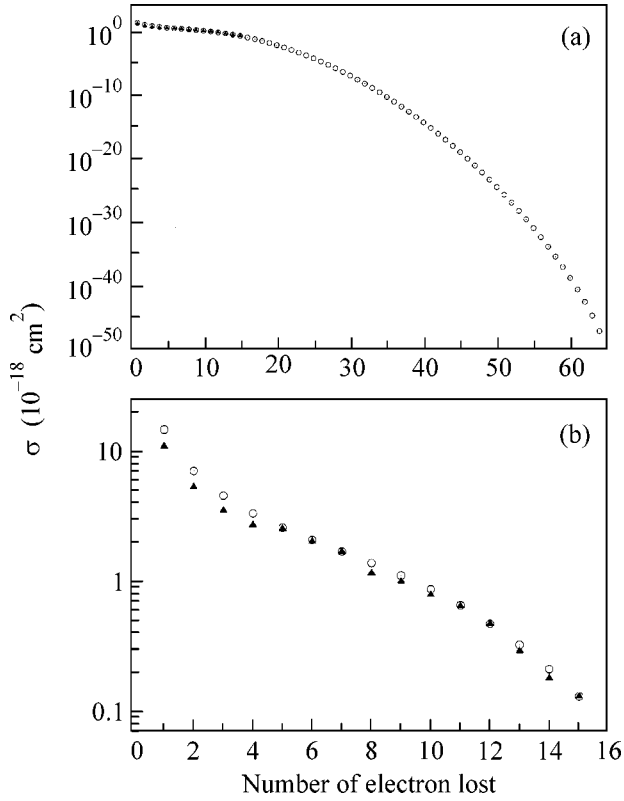
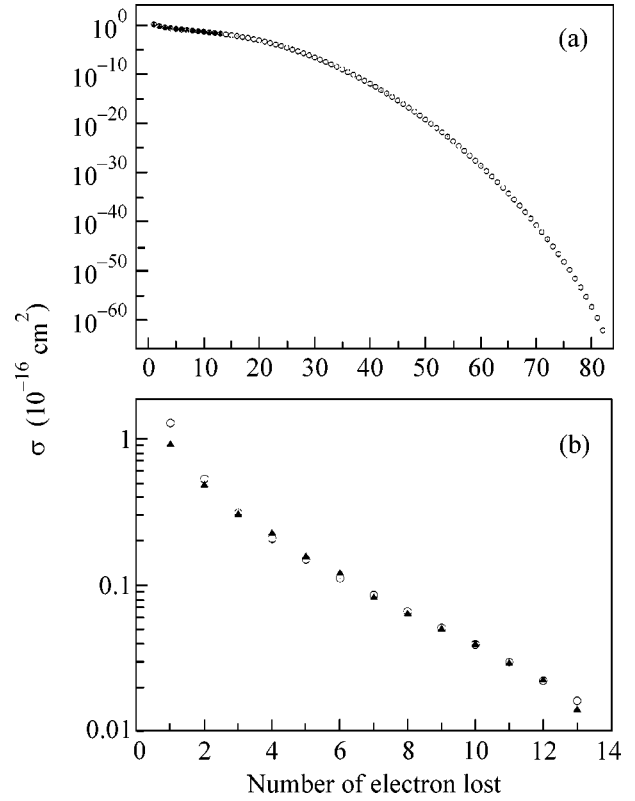**Fig. 1.** (Circles) Calculated cross section (divided by $10^{-18}$ cm$^2$) for the multiple loss of electrons by the U$^{28+}$ ion with an energy of 6.5 MeV/u that collides with the Ar atom vs. the number of removed electrons (a) in the entire possible range of the number of removed electrons from a minimum value of 1 to a maximum value of 64 and (b) in the narrow range of the number of removed electrons from 1 to 15 for which measurements (shown by the triangles) were carried out [2].



**Fig. 2.** (Circles) Calculated cross section (divided by $10^{-16}$ cm$^2$) for the multiple loss of electrons by the U$^{10+}$ ion with an energy of 1.4 MeV/u that collides with the Ar atom vs. the number of removed electrons (a) in the entire possible range of the number of removed electrons from a minimum value of 1 to a maximum value of 82 and (b) in the narrow range of the number of removed electrons from 1 to 13 for which measurements (shown by the triangles) were carried out [1].

When $b_0 = 0$, the integration in Eq. (11) should be performed with respect to $db^2$ and $g(b) = G = 1/2$ and $\lambda = 1$. As a result, the cross section for the complete $N_p$-multiple ionization of the projectile is expressed as

$$\sigma^{N_p+} = 2\pi\frac{G}{(Z_{N_p}^*)^2}\frac{1}{\mu}\Gamma\left(\frac{\lambda}{\mu}\right)\left[\frac{1}{FN_p}\right]^{\lambda/\mu}[p(b_0)]^{N_p}. \quad (13)$$

For the $(N_p - 1)$-multiple ionization, the probability is equal to the difference between two terms. Separately integrating each term by the Laplace method, we obtain the cross section for $(N_p - 1)$-multiple ionization in the form

$$\sigma^{(N_p-1)+} = N_p\sigma^{N_p+}$$
$$\times\left[\left(\frac{Z_{N_0}^*}{Z_{N_p-1}^*}\right)^2\left(\frac{N_p}{N_p-1}\right)^{\lambda/\mu}\frac{1}{p(b_0)} - 1\right]. \quad (14)$$

For the general case of $(N_p - N)$-multiple ionization, we similarly obtain

$$\sigma^{(N_p-N)+} = \frac{N_p!\sigma^{N_p+}}{(N_p-N)!N!}$$
$$\times\sum_{m=0}^{N}(-1)^m\left(\frac{Z_{N_p}^*}{Z_{N_p-N+m}^*}\right)^2\frac{N!}{(N-m)!m!} \quad (15)$$
$$\times\left(\frac{N_p}{(N_p-N+m)}\right)^{\lambda/\mu}\{p(b_0)\}^{-N+m},$$

where $Z_{N_p-N+m}^*$ is the effective charge at $(N_p - N + m)$-multiple ionization.

In principle, final Eqs. (13)–(15) make it possible to calculate the cross section for ionization of any multiplicity (under the condition that $N_p \gg 1$ and $N_p - N \gg 1$) or to reconstruct all cross sections from two known cross sections. It is worth noting that the choice of two

cross sections considered experimentally known can be arbitrary and is determined by the conditions $N_p - N \gg 1$ of the applicability of Eqs. (13)–(15). The result of this calculation for the multiple ionization of uranium ions colliding with argon atoms is shown in Figs. 1 and 2 together with experimental data [1, 2]. In calculations, the effective charge is taken to be equal to the ionization multiplicity, i.e., $Z_N^* = Q + N$, where $Q$ is the initial charge (the structure ion charge before collision) of the projectile. The $\lambda/\mu$ ratio is a varying parameter. For $U^{28+}$ + Ar collisions, we take $\lambda/\mu = 1.1$ and the cross sections $\sigma^{12+}$ and $\sigma^{15+}$ are treated as known. For $U^{10+}$ + Ar collisions, we take $\lambda/\mu = 1.5$ and the cross sections $\sigma^{10+}$ and $\sigma^{12+}$ are treated as known.

Panels (a) of both figures show cross sections vs. the number of removed electrons in a wide range (entire interval) from a minimum value, i.e., the removal of one electron, to a maximum possible number of removed electrons (e.g., the maximum possible number of removed electrons is equal to 82 for $U^{10+}$). For convenient comparison between calculation and experiment, panels (b) of both figures show cross sections for which experimental data are available, because the wide range of variation of quantities presented in panels (a) cannot provide the correct representation of the corresponding relatively narrow region. As is seen in the figures, the calculation results are in satisfactory agreement with experiments [1, 2] even for low-multiple ionization that is formally beyond the applicability domain ($N_p - N \gg 1$) of Eqs. (13)–(15). Strictly speaking, Eq. (6) should be used for the case of low-multiple ionization.

## REFERENCES

1. R. D. DuBois, A. C. F. Santos, Th. Stohlker, *et al.*, Phys. Rev. A **70**, 032 712 (2004).

2. R. E. Olson, R. L. Watson, V. Horvat, *et al.*, J. Phys. B **37**, 4539 (2004).

3. R. L. Watson, Yong Peng, V. Horvat, *et al.*, Phys. Rev. A **67**, 022 706 (2003).

4. A. B. Voitkiv, N. Grun, and W. Scheid, J. Phys. B **33**, 3431 (2000).

5. A. B. Voitkiv, G. M. Sigaud, and E. C. Montenegro, Phys. Rev. A **59**, 2794 (1999).

6. J. Eichler, Phys. Rev. A **15**, 1856 (1977).

7. A. M. Dykhne and G. L. Yudin, Usp. Fiz. Nauk **125**, 377 (1978) [Sov. Phys. Usp. **21**, 549 (1978)].

8. F. Salvat, J. D. Martinez, R. Mayol, and J. Parellada, Phys. Rev. A **36**, 467 (1987).

9. V. I. Matveev and E. S. Gusarevich, Zh. Éksp. Teor. Fiz. **123**, 42 (2003) [JETP **96**, 34 (2003)].

10. V. I. Matveev, Fiz. Élem. Chastits At. Yadra **26**, 780 (1995) [Phys. Part. Nucl. **26**, 329 (1995)].

11. V. I. Matveev and Kh. Yu. Rakhimov, Zh. Éksp. Teor. Fiz. **114**, 1646 (1998) [JETP **87**, 891 (1998)].

12. V. I. Matveev, Kh. Yu. Rakhimov, and D. U. Matrasulov, J. Phys. B **32**, 3849 (1999).

13. F. W. J. Olver, *Asymptotics and Special Functions* (Academic, New York, 1974; Nauka, Moscow, 1978).

*Translated by R. Tyapaev*

# Features of the Pressure-Induced Phase Transitions in Eu₂(MoO₄)₃ Single Crystals

**I. M. Shmyt'ko\*, E. A. Kudrenko, V. V. Sinitsyn, B. S. Red'kin, and E. G. Ponyatovsky**

*Institute of Solid State Physics, Russian Academy of Sciences, Chernogolovka, Moscow region, 142432 Russia*

*\* e-mail: shim@issp.ac.ru*

Received August 5, 2005

The structural changes induced by a 9-GPa pressure in $Eu_2(MoO_4)_3$ single crystals at room temperature have been studied using x-ray diffraction. It is established that a structural phase transition from the initial tetragonal phase to the new high-pressure tetragonal phase occurs rather than solid-phase amorphization that was observed previously in polycrystalline samples. The samples in the observed transition remain single-crystalline despite a significant difference ($\Delta V \sim 18\%$) between the specific volumes of the initial and final phases. It is shown that the transition from the initial state to the high-pressure phase occurs via the formation of broad transition zones featuring a continuous and smooth change of the crystal lattice parameters. © 2005 Pleiades Publishing, Inc.

PACS numbers: 74.50.+r, 74.80.Fp

$Eu_2(MoO_4)_3$ crystals belong to an isostructural series of rare earth molybdates with the general formula $R_2(MoO_4)_3$, where R = Pr, Nd, Sm, Eu, Gd, Tb, and Dy [1]. At atmospheric pressure, these compounds occur in the form of two thermodynamically stable crystal modifications, namely, the high-temperature $\beta$ phase ($P42_1m$) and the low-temperature $\alpha$ phase ($C2/c$) [1]. The $\alpha \Rightarrow \beta$ phase transition in $Eu_2(MoO_4)_3$ takes place on heating to 1078 K and is accompanied by a significant (~25%) change in the specific volume [1, 2]. This large difference retards the kinetics of the reverse $\beta \Rightarrow \alpha$ polymorphic transformation, so that the $\beta$ phase is retained in a metastable state on cooling down to 453 K. At this temperature, europium molybdate exhibits a phase transition of the first order (close to the second order) with a small volume change to another metastable ($\beta'$) phase with $Pba2$ symmetry [1, 3].

Brixner [2] suggested that a sufficiently high pressure would induce a transition of the $\beta'$ phase of rare earth molybdates to the more compact $\alpha$ phase. However, it was found that $Gd_2(MoO_4)_3$ exhibited pressure-induced amorphization, rather than the anticipated $\beta' \Rightarrow \alpha$ phase transition. Subsequently, the phenomenon of amorphization under the action of high pressure was confirmed for $Gd_2(MoO_4)_3$ [4] and observed for the first time in $Tb_2(MoO_4)_3$, $Sm_2(MoO_4)_3$, $TbGd(MoO_4)_3$, and $Eu_2(MoO_4)_3$ [5–7]. The pressure corresponding to the onset of amorphization at room temperature was approximately the same (~7 GPa) for all compounds [5], and the final amorphous state was retained up to 11.5 GPa (the maximum pressure achieved in these investigations). Based on the available data and an analysis of the specific volume changes, it was suggested [4, 5] that the pressure-induced amorphization

observed in $Sm_2(MoO_4)_3$, $Tb_2(MoO_4)_3$, $Gd_2(MoO_4)_3$, and $Eu_2(MoO_4)_3$ was probably stimulated by the chemical decomposition of these compounds into $R_2O_3$ and $MoO_3$ oxides. It was also pointed out that (i) there was a difference in the x-ray diffraction patterns observed for the amorphous samples obtained under hydrostatic and quasihydrostatic conditions and (ii) the samples amorphized at a pressure in the interval from 7.0 to 11.5 GPa remained amorphous upon pressure release. An important factor in all the aforementioned investigations was that the experiments were performed on polycrystalline (powdered) samples.

This paper presents the results of an x-ray diffraction study of structural changes taking place in the initially single-crystalline $Eu_2(MoO_4)_3$ samples under the action of a hydrostatic pressure of about 9 GPa. This pressure level was selected so as to correspond approximately to the middle of the interval of pressures in which irreversible amorphization was observed in all the polycrystalline $R_2(MoO_4)_3$ samples studied previously.

The initial $Eu_2(MoO_4)_3$ single crystals had the form of Czochralski melt-grown ingots with a diameter of 15 mm and a length of 25 mm. The ingot was cut into separate single crystal samples with dimensions $3.0 \times 4.0 \times 1.0$ mm and the large face parallel to the (100) or (001) crystallographic planes (*a*- and *c*-cuts, respectively). The x-ray diffraction measurements were performed on a Siemens D-500 diffractometer using $CuK_{\alpha1}$ radiation. It was established that the surfaces of samples as-cut from the ingot exhibited reflections characteristic of the $\beta'$ phase, whereas the x-ray diffraction pattern observed upon the optical polishing of these samples corresponded to the $\beta$ phase.
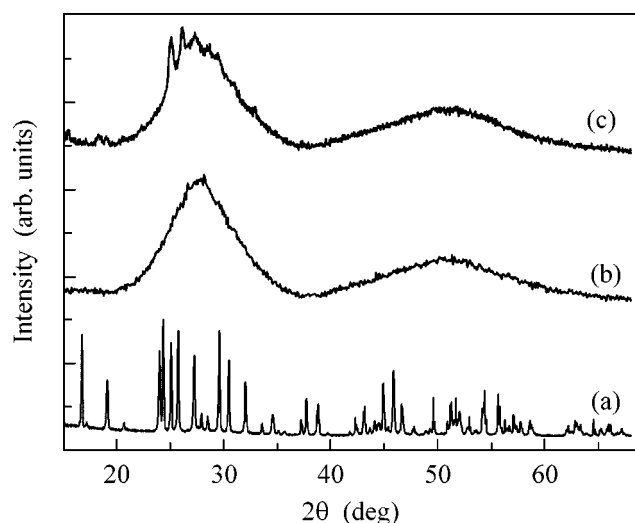
**Fig. 1.** X-ray diffraction patterns of polycrystalline $Eu_2(MoO_4)_3$ samples (a) in the initial state and (b, c) upon 9-GPa compression under quasihydrostatic and hydrostatic conditions, respectively, at room temperature.
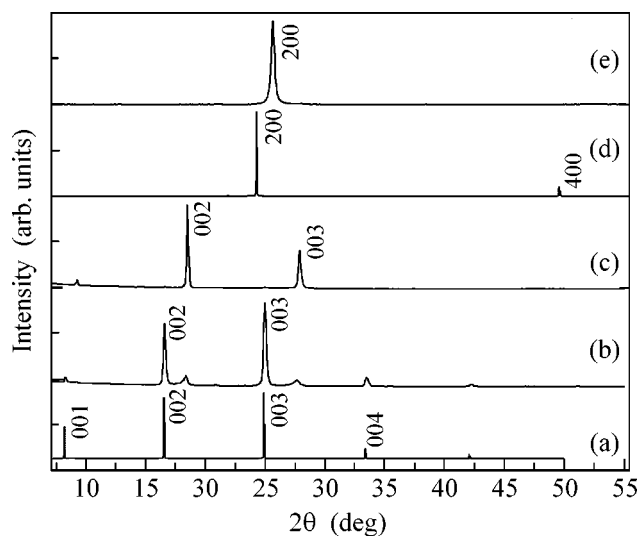


**Fig. 2.** X-ray diffraction patterns of $Eu_2(MoO_4)_3$ singe crystals: (a–c) *c*-cut samples in the initial state and upon 9-GPa hydrostatic compression for 1 and 7 days, respectively; (d, e) *a*-cut samples in the initial state and upon 9-GPa hydrostatic compression for 7 days, respectively.

The investigation was carried out at room temperature in a high-pressure chamber of the toroid type. In order to reveal the similarity and difference in behavior of the polycrystalline and single-crystalline $Eu_2(MoO_4)_3$ samples under pressure, we performed the following series of experiments.

(i) A fine disperse powder obtained by grinding of a single crystal was subjected for 2 h to a 9-GPa quasi–

hydrostatic compression (in the absence of any pressure transmitting medium).

(ii) The same powdered sample was subjected for 2 h to a 9-GPa pressure under hydrostatic conditions.

(iii) A *c*-cut single crystal was subjected to a 9-GPa hydrostatic pressure for 1 or 7 days.

(iv) An *a*-cut single crystal was subjected to a 9-GPa hydrostatic pressure for 7 days.

The pressure transmitting medium for hydrostatic loading was an ethanol–methanol mixture, which occurs in a liquid state in the range of pressures used in our experiments.

Figure 1a shows the typical x-ray diffractogram of the initial polycrystalline $Eu_2(MoO_4)_3$ sample. The positions and intensities of the diffraction lines correspond to the β phase of $Eu_2(MoO_4)_3$, which implies that the grinding (crushing and trituration) of single crystals leads to the phase transition from β' to β phase.

Figure 1b presents the x-ray diffraction profile of a polycrystalline sample compressed to 9-GPa under quasihydrostatic condition for 2 h and then unloaded to atmospheric pressure. The broad reflections are indicative of an amorphouslike state of the sample, which confirms the previous results concerning the amorphization of polycrystalline $R_2(MoO_4)_3$ samples at pressures in the 7–11.5 GPa range [2, 4, 5].

Figure 1c shows the typical x-ray diffraction pattern of a polycrystalline sample exposed to a 9-GPa pressure under hydrostatic conditions for 2 h and then unloaded to atmospheric pressure. As can be seen, the diffractogram displays rather narrow lines on the background of broad halo reflections. These peaks show evidence either for incomplete amorphization or for a partial reverse process (recrystallization). Attempts to assign indices of the α or β phases to the observed narrow reflections were unsuccessful.

Figure 2 presents the x-ray diffractograms of *a*- and *c*-cut single crystals measured in a broad range of diffraction angles. Here, Fig. 2a corresponds to the initial state of the *c*-cut sample; Figs. 2b and 2c refer to the *c*-cut sample upon 9-GPa hydrostatic compression for 1 and 7 days, respectively; Fig. 2d shows the diffractogram of the *a*-cut single crystal in the initial state; and Fig. 2e characterizes this crystal upon a 7-day hydrostatic compression at 9 GPa. In addition to the main (200) reflection characteristic of the *a*-cut observed in Fig. 2e, this diffractogram contains several weak reflections. The positions of these signals relative to the main reflections observed in the initial state are presented on a greater scale in Fig. 3. The diffractograms of *c*-cut samples exhibited no other weak reflections besides those depicted in Fig. 2.

It should be emphasized that all the single-crystalline samples remained transparent upon unloading.

The main conclusion following from an analysis of the x-ray diffractograms in Fig. 2 is that the initial single crystals subjected to hydrostatic compression at

9 GPa exhibited the transition to a new, previously unknown high-pressure phase, rather than a solid-phase amorphization such as that observed in polycrystalline samples. In addition, the positions of diffraction lines in Fig. 2 suggest that $Eu_2(MoO_4)_3$ single crystals exhibit, during the exposure to a 9-GPa hydrostatic pressure, a phase transition from the tetragonal β phase (metastable at atmospheric pressure) to a new high-pressure tetragonal phase with the lattice cell parameters $a \approx 7.025$ Å and $c \approx 9.702$ Å. This conclusion follows from the fact that the diffractograms of $a$- and $c$-cut single crystals upon a 7-day compression at 9 GPa exhibit the lines corresponding to only one lattice parameter ($c$ in Fig. 2c and $a$ in Fig. 2e) in several orders of reflection. The unit cell volume of the new high-pressure tetragonal phase is $V \approx 478.82$ Å$^3$, which is 18.6% smaller than the value for the initial tetragonal phase at the same pressure ($a \approx 7.364$ Å, $c \approx 10.641$ Å, $V \approx 577.05$ Å$^3$). After a 1-day exposure at 9 GPa (Fig. 2b), the sample was two-phase and comprised a mixture of the initial β phase and the new high-pressure tetragonal phase.

The natural question as to whether the observed transition is isomorphic, that is, whether the space groups of the initial tetragonal phase and the new high-pressure tetragonal phase are coinciding, cannot be given a clear answer based on the above structural data. However, we must pay attention to the difference in the relative intensities of the (300) and (400) reflections in the initial state and in the new high-pressure phase. Indeed, the (300) reflection is absent (because it is forbidden) in the x-ray diffraction pattern of the initial phase (Fig. 3a), whereas both the (300) and (400) reflections of significant intensity are present in the diffractogram of the high-pressure phase (Fig. 3b). At the same time, Figs. 3b and 2e show that these (300) and (400) reflections for the high-pressure phase possess a much lower intensity relative to that of the (200) reflection as compared to the case of the initial phase (Fig. 2d). These differences in relative intensities can be both due to a difference in the space symmetry groups and due to strong local structure violations in the high-pressure phase. As is known, local straining of a crystal lattice may lead, on the one hand, to violation of the laws of reflection quenching (and, hence, to the appearance of forbidden reflection) and, on the other hand, to a drop in intensity of the high-order reflections (because an irregular structure hinders multiple reflections necessary for the formation of such diffraction signals).

Let us consider the observed two-phase state in more detail. The presence of such a state featuring two different single-crystalline phases in the same sample poses a question concerning their matching. An answer is provided by an analysis of the 2D patterns obtained for cross sections in the reciprocal space of base reflections of the (00$l$) type for a sample in the two-phase state. Figure 4 shows an example of such a 2D map for (002)$_{atmospheric pressure}$ and (002)$_{high pressure}$ reflections. As
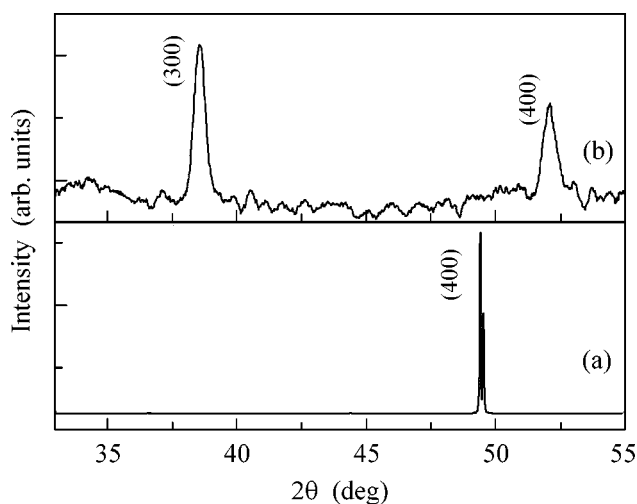


**Fig. 3.** Region of weak reflections in the x-ray diffractograms of the $a$-cut $Eu_2(MoO_4)_3$ singe crystals (a) in the initial state and (b) upon 9-GPa hydrostatic compression for 7 days.
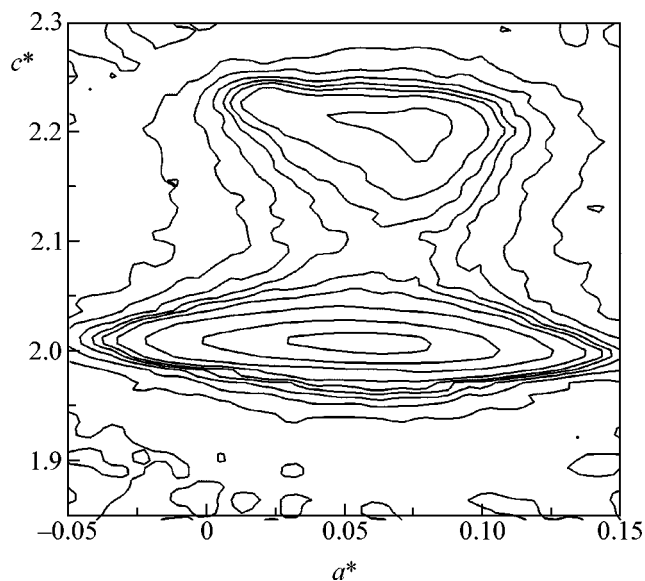


**Fig. 4.** 2D cross section of the reciprocal lattice of a $Eu_2(MoO_4)_3$ singe crystal in the region of (002)$_{atmospheric pressure}$ and (002)$_{high pressure}$ reflections.

can be seen, the reflections of the initial phase and the high-pressure phase are connected by a junction region featuring several isolines of the diffraction intensity, which are common for both phases. The presence of this junction region connecting the two reflections indicates that the transition from one phase to another proceeds via the formation of transition zones featuring a continuous and smooth change of the crystal lattice parameters from $d(002)_{atmospheric pressure}$ to $d(002)_{high pressure}$. We believe that this transition is possi-

ble only if the local order in both phases is retained. This conclusion implies that the transition from the initial state to the high-pressure phase has a subgroup character or is even isomorphic. Additional evidence in favor of this interpretation is the retained transparency of samples in the two-phase state (otherwise, a change in the local order would lead to the formation of random phase boundaries and, hence, to the loss of transparency).

In conclusion, the main results of this investigation can be formulated as follows:

(i) The results of x-ray diffraction measurements showed that the sequence of phase states formed in $Eu_2(MoO_4)_3$ single crystals as a result of a high-pressure treatment is substantially different from that observed in polycrystalline samples. In particular, the exposure to a pressure in the region of 9 GPa leads to the formation of a new tetragonal phase with a specific volume 18.6% lower than that of the initial β phase, rather than to the well-known amorphization of the initial polycrystalline powder.

(ii) The structural phase transition from the initial tetragonal phase to the new high-pressure tetragonal phase in single-crystalline samples proceeds via the formation of broad transition zones featuring a continuous and smooth change of the crystal lattice parameters.

## REFERENCES

1. L. H. Brixner, J. R. Barkley, and W. Jeitschko, in *Handbook on the Physics and Chemistry of Rare Earths*, Ed. by K. A. Gschneider, Jr. and L. Eyring (North-Holland, Amsterdam, 1979; Metallurgiya, Moscow, 1982), Chap. 30, p. 610.

2. L. H. Brixner, Mater. Res. Bull. **7**, 879 (1972).

3. A. Fouskova, J. Phys. Soc. Jpn. **27**, 1699 (1969).

4. E. G. Ponyatovsky, V. V. Sinitsyn, R. A. Dilanyan, and B. S. Red'kin, JETP Lett. **61**, 222 (1995).

5. V. Dmitriev, V. Sinitsyn, R. Dilanyan, *et al.*, J. Phys. Chem. Solids **64**, 307 (2003).

6. A. Jayaraman, S. K. Sharma, Z. Wang, *et al.*, J. Phys. Chem. Solids **54**, 827 (1993).

7. A. V. Pal'nichenko, E. G. Ponyatovskiĭ, B. S. Red'kin, and V. V. Sinitsyn, Pis'ma Zh. Éksp. Teor. Fiz. **68**, 623 (1998) [JETP Lett. **68**, 657 (1998)].

*Translated by P. Pozdeev*

# Formation and Composition of the Clathrate Phase in the H₂O–H₂ System at Pressures to 1.8 kbar

**O. I. Barkalov[a], S. N. Klyamkin[b], V. S. Efimchenko[a], and V. E. Antonov[a]**

[a] *Institute of Solid State Physics, Russian Academy of Sciences, Chernogolovka, Moscow region, 142432 Russia*
*e-mail: efimchen@issp.ac.ru*
[b] *Moscow State University, Vorob'evy gory, Moscow, 119992 Russia*
Received July 14, 2005

The transition of the hexagonal ice phase $I_h$ to the clathrate phase $s$II has been found in the $H_2O$–$H_2$ system at a pressure of about 1 kbar under conditions of an excess of gaseous hydrogen. The pressures of the $I_h \longrightarrow s$II and $s$II $\longrightarrow I_h$ transitions have been determined over a temperature range from –36 to –18°C, and the pressure dependence of the synthesis temperature of the clathrate phase from a liquid at pressures from 1.0 to 1.8 kbar has been constructed. The solubility of hydrogen in the $I_h$ and $s$II phases and in liquid water has been measured. The concentration of hydrogen in the clathrate phase $s$II is about 1.2 wt % (10 mol %) near the boundary of the $s$II $\longrightarrow I_h$ transition, and it increases to 2 wt % (16 mol %) at a pressure of 1.8 kbar. © 2005 Pleiades Publishing, Inc.

PACS numbers: 05.70.Fh

Dyadin *et al.* [1] studied the $H_2O$–$H_2$ system by differential thermal analysis and found a region with anomalous behaviors of the melting temperature and the kinetics of melting of ice in an atmosphere of hydrogen at pressures from 1 to 3.6 kbar. They hypothesized that the clathrate phase of hydrogen hydrate was formed in this pressure range. Indeed, the clathrate phase $s$II of hydrogen hydrate was synthesized more recently [2, 3] from a liquid at a pressure of about 2 kbar and at –24°C. Lokshin *et al.* [3] studied the composition of this phase by neutron-diffraction analysis and found that $H_2/H_2O = (32 + X)/136$, where $X$ varied from 0 to 16 depending on pressure and temperature.

The value of $X = 16$ corresponds to the dissolution of 3.8 wt % hydrogen in ice. Because of such a high concentration of hydrogen in ice at the pressure $P \approx$ 2 kbar, which is reachable within ice planet satellites, a study of the $H_2O$–$H_2$ system at $P \leq 2$ kbar is of considerable interest in both high-pressure physics and chemistry and planetology [2].

The aim of this work was to study experimentally the transition of the hexagonal phase $I_h$ of low-pressure ice to the clathrate phase $s$II and vice versa and to study the transition from the liquid phase to the clathrate phase. The measurements were performed under conditions of an excess of molecular hydrogen. The transitions were determined from changes in the solubility of hydrogen in $H_2O$ at pressures from 0.2 to 1.8 kbar.

The experimental setup has been described elsewhere [4]. High-purity hydrogen (99.9999%) was prepared by the thermal decomposition of the hydride of the Ti–Fe–V alloy. The amount of hydrogen absorbed by a sample was determined volumetrically by measuring pressure and temperature in calibrated volumes of the measuring system. A modified van der Waals equation for strongly compressed hydrogen was used as the equation of state for the gaseous phase; this equation took into account the temperature and pressure dependence of coefficients [5]. Published data [6] on the pressure and temperature dependence of the molar volumes of liquid water and ice $I_h$ were used. The molar volume of the clathrate phase $s$II was evaluated based on the published value [2] of the lattice parameter $a \approx 17.05$ Å of this cubic phase at $P = 2.2$ kbar and $T = -39$°C.

The sample of $H_2O$ had a volume of about 1 cm³ and consisted of individual segments with characteristic sizes of about 5 mm. The steady-state pressure reached after changing temperature or total hydrogen amount in an autoclave was measured in the experiments. The drift of pressure lasted about 5 min, about 1 h, or 3–5 min in the absence of phase transitions, in the $I_h \longrightarrow s$II and $s$II $\longrightarrow I_h$ transitions, or in the synthesis of the $s$II phase from a liquid, respectively. With consideration for errors in the determination of various phase volumes in the $H_2O$–$H_2$ system, the concentration of hydrogen in condensed phases was determined to within ±0.05 wt %.

Figure 1 shows a typical solubility isotherm of hydrogen in water ice. The concentration of hydrogen in the $I_h$ phase at $T = -22$°C increased from 0.1 wt % at $P = 0.5$ kbar to 0.3 wt % at $P = 1$ kbar. A transition to the clathrate phase $s$II occurred at a higher pressure, and the amount of dissolved hydrogen increased to 1.2 wt %. As the pressure was increased to 1.8 kbar, the solubility of hydrogen in the clathrate phase monotonically increased to approximately 2 wt %.
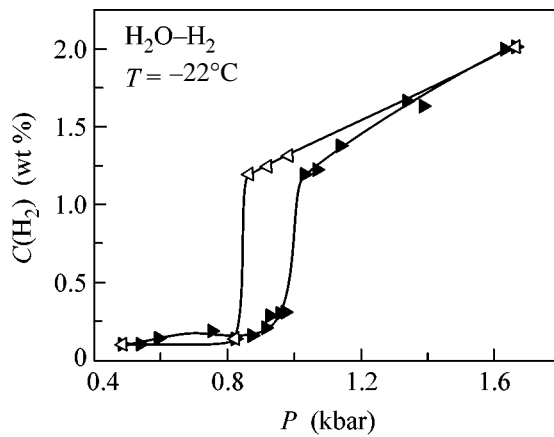
**Fig. 1.** Solubility of hydrogen in ice at –22°C. Closed and open triangles refer to increasing and decreasing pressure, respectively.



**Fig. 2.** Solubility of hydrogen in $H_2O$ in the course of decreasing temperature at a pressure of 1.3 kbar.

A smooth decrease in the concentration of hydrogen in the clathrate phase was observed in the course of decreasing pressure at all of the test temperatures. For example, as can be seen in Fig. 1, at $T = -22$°C, the composition decreased from 2 wt % at $P = 1.8$ kbar to 1.2 wt % at $P \approx 0.8$ kbar; thereafter, a transition to the ice phase $I_h$ occurred.

Figure 2 shows the isobar of hydrogen solubility in liquid water and the $s$II phase at $P \approx 1.3$ kbar. The amount of hydrogen dissolved in the liquid increased from 0.2 wt % at +16°C to 0.4 wt % at –18°C. After the transition to the clathrate phase, the solubility of hydrogen increased to 1.9–2.0 wt %.

The phase transition points in the $H_2O$–$H_2$ system determined in this work were plotted in the $T$–$P$ diagram, which is shown in Fig. 3. The pressure of the transition of ice $I_h$ to the clathrate phase $s$II is about 1 kbar, and it only slightly depends on temperature. The pressure of the reverse transition of the $s$II phase to ice $I_h$ decreased with temperature from 0.9 kbar at –18°C to 0.5 kbar at –36°C. The synthesis of the clathrate phase from the liquid occurred at a temperature 5–7°C lower than the melting temperature of ice $I_h$ at the same pressure in the absence of hydrogen.

In the tested range of temperatures to –36°C, the maximum concentration of hydrogen in ice $I_h$ was about 0.3 wt %; this concentration was reached at the pressure $P \approx 1$ kbar near the boundary of a transition to the clathrate phase $s$II (closed circles in Fig. 3). The concentration of hydrogen in the $s$II phase changed from approximately 1.2 wt % near the boundary of a transition to ice $I_h$ (to the right of open circles in Fig. 3) to 2 wt % at a pressure of 1.8 kbar.

The solubility of hydrogen in the $I_h$ and $s$II phases over the given temperature and pressure ranges was not studied previously. Lokshin *et al.* [3] evaluated the hydrogen content of the $s$II phase at temperatures lower than –73°C based on the most likely interpretation of
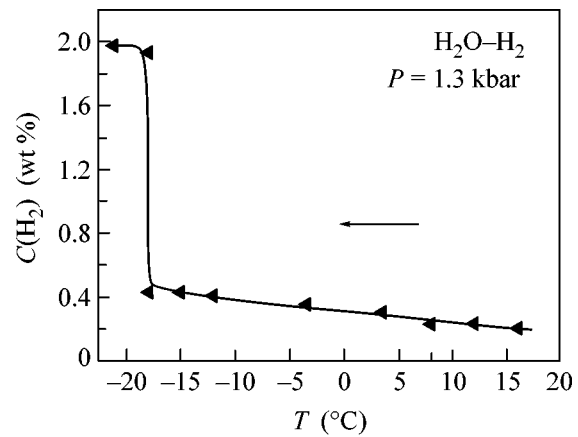
the neutron-diffraction patterns of $D_2O$–$D_2$ polycrystals measured at the two pressures 1 bar and 2 kbar over a temperature range from –233 to –73°C. According to this evaluation, the concentration of hydrogen in the $s$II phase of the $H_2O$–$H_2$ system can vary within a range from 2.5 wt % ($H_2/H_2O = 32/136$) to 3.8 wt % ($H_2/H_2O = 48/136$).

The minimum value of 1.2 wt % obtained in this work for the concentration of hydrogen in the $s$II phase is lower than a value of 2.5 wt % by a factor of about 2; according to Lokshin *et al.* [3], the latter value is required for the stability of the clathrate structure $s$II. The linear extrapolation of the solubility isotherms of
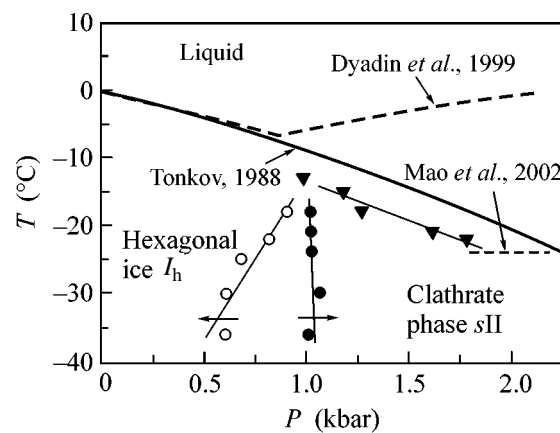


**Fig. 3.** $T$–$P$ diagram of the $H_2O$–$H_2$ system. Closed and open circles refer to $I_h \longrightarrow s$II and $s$II $\longrightarrow I_h$ phase transition points, respectively. Closed triangles indicate the conditions of the synthesis of the $s$II phase from a liquid with decreasing temperature (this work) and the dashed horizontal segment refers to published data [2]. The dashed curve shows the melting line of the clathrate phase $s$II determined by Dyadin *et al.* [1] and the solid line shows the melting temperature of ice $I_h$ in the absence of hydrogen [7].

hydrogen in the $s$II phase (e.g., see Fig. 1) to a maximum pressure of 3.6 kbar (according to Dyadin *et al.* [1], this is the maximum pressure at which this phase can exist) gave a value of about 4 wt %. This value is close to an estimated value of 3.8 wt % found by Lokshin *et al.* [3] for the maximally possible hydrogen concentration in the $s$II phase.

## REFERENCES

1. Yu. A. Dyadin, É. G. Larionov, and A. Yu. Manakov, Zh. Strukt. Khim. **40**, 974 (1999).

2. W. L. Mao, H. Mao, A. F. Goncharov, *et al.*, Science **297**, 2247 (2002).

3. K. A. Lokshin, Y. Zhao, D. He, *et al.*, Phys. Rev. Lett. **93**, 125503 (2004).

4. S. N. Klyamkin and V. N. Verbetsky, J. Alloys Compd. **194**, 41 (1993).

5. H. Hemmes, A. Driessen, and R. Griessen, J. Phys. C **19**, 3571 (1986).

6. W. B. Bridgman, J. Chem. Phys. **3**, 597 (1935).

7. E. Yu. Tonkov, *High Pressure Phase Transformations: A Handbook* (Metallurgiya, Moscow, 1988; Gordon and Breach, Philadelphia, 1992), Vol. 2, p. 448.

*Translated by V. Makhlyarchuk*

# Atomic Structure of the Cu(410)-O Surface: STM Visualization of Oxygen and Copper Atoms

## A. N. Chaĭka and S. I. Bozhko

*Institute of Solid State Physics, Russian Academy of Sciences, Chernogolovka, Moscow region, 142432 Russia*
Received July 25, 2005

The structure of the Cu(410)-O surface is studied by a scanning tunneling microscope (STM) with atomic resolution. Tunneling is accomplished for various states of the tungsten STM probe, which allows oxygen and copper atoms to be visualized separately. © *2005 Pleiades Publishing, Inc.*

PACS numbers: 68.35.Rh, 68.37.Ef, 68.43.Fg, 73.40.Gk

Knowledge of oxidation processes is important for understanding corrosion processes and for developing technologies using oxide layers as interfaces. Interest in ordered oxygen structures on the copper surface is also due to the development of studies of high-temperature superconductivity. Ordered structures arising upon oxygen adsorption on the Cu(100) surface and on vicinal copper surfaces were studied using various techniques [1–10], including scanning tunneling microscopy (STM) [1–7]. One of the most comprehensively studied oxygen structures of vicinal copper surfaces is (410)-O. However, a certain atomic structure model cannot be definitively chosen for this surface based on the experimental results obtained. The goal of this work was to study the atomic structure of the Cu(410)-O surface by the STM technique. The surface was prepared by Cu(511) surface faceting.

A Cu(511) sample was cut by an electric spark machine from a single crystal copper ingot that was preannealed at a temperature of 1050°C (slightly lower than the melting apex) in an oxygen atmosphere ($p = 5 \times 10^{-4}$ Torr) for 30 h. Upon annealing, oxygen penetrated into the crystal bulk and bound electrically active impurities, which led to an increase in the electron mean free path [11]. The sample was a disk 8 mm in diameter and 3 mm in thickness whose surface plane coincided with the (511) plane. The surface orientation was determined using x-ray diffraction methods with an accuracy of 1°. Before investigations, the sample was previously polished mechanically and electrochemically to remove the broken surface layer. The cleaning of the Cu(511) surface from impurities (carbon and sulfur) was performed by means of several sequential cycles of ion (Ar$^+$) bombardment ($p = 5 \times 10^{-5}$ Torr, $E = 550$ eV) and heating in ultrahigh vacuum (UHV) at temperatures of 400–450°C for 20–30 min. The base vacuum in the STM chamber was no worse than $1 \times 10^{-10}$ Torr. At these temperatures, the diffusion of oxygen atoms from the sample bulk to the surface is insignificant. The elemental composition was controlled by Auger electron spectroscopy (AES). The UHV annealing of the sample at temperatures of 550–600°C led to the diffusion of oxygen toward the sample surface, where its equilibrium concentration was attained in 15–20 min. According to the AES data, the further heating of the surface left the oxygen concentration on the surface unchanged. The ratio of the intensities of the oxygen and copper lines in the Auger spectra after the heating of the sample was $I_{O(512)}/I_{Cu(920)} = 0.16 \pm 0.03$, which corresponded to a surface coverage of 0.5 monolayer of oxygen [12]. Surface faceting occurred under these conditions (Fig. 1), and well-ordered structures formed on each face of the facets. The occurrence of an ordered crystal structure on the faceted surface was controlled by low-energy electron diffraction. It was very difficult to interpret the diffraction pattern, because it represented a superposition of diffraction patterns from three facet surfaces; however, the atomic ordering of the faces can be judged from the occurrence of sharp reflections. The characteristic sizes of the facets were determined by the annealing temperature and time and varied from several hundreds to several thousands of angstroms. One of the facet faces (designated in Fig. 1) coincided with the (410) plane.

The atomic structure of the (410) face of a facet was studied by STM at room temperature under UHV conditions. A tungsten tip was used as a probe. The tip apex was obtained by electrochemically overetching a polycrystalline wire 0.3 mm in diameter. The quality of the obtained tips (the apex length to apex diameter ratio) was controlled by a transmission electron microscope. To remove oxides from the tip and to obtain a thinner apex, the tip was subjected to high-temperature heating in the preparation chamber (20–30 s at $t = 800$°C, $p = 1 \times 10^{-9}$ Torr) and ion (Ar$^+$) bombardment in the STM chamber ($E = 600$ eV, $p = 5 \times 10^{-5}$ Torr). At the ion etching, the defocused argon ion beam was directed along the apex axis. At this coaxial arrangement of the tip and the incident beam (the beam deflection did not exceed 10°–12°), the apex was sharpened. Before the measure-
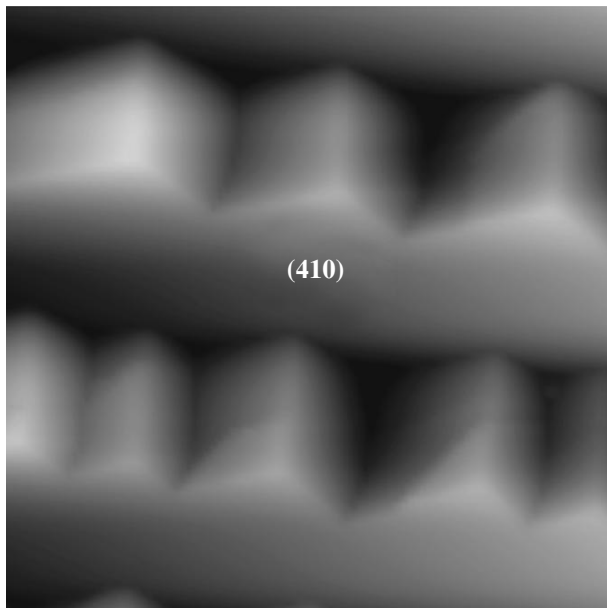
**Fig. 1.** The $776 \times 792$-nm STM image of the faceted Cu(511)-O surface. The image was obtained in the constant tunneling current mode at $U_{tun} = -700$ mV, $I_{tun} = 0.15$ nA. Indices designate one of the (410) planes.

ments at the copper surface, the STM tips and scanner were previously tested and calibrated on a highly oriented pyrolytic graphite HOPG(0001) surface.

In order to avoid uncontrolled temperature drift, the atomic structure of the faceted Cu(511)-O surface was studied by the STM technique several hours after the annealing of the sample. The time from the heating to the measurements was varied from 2 to 70 h. Under these conditions, the temperature drift did not exceed 4 Å/min. Note that, at such long time intervals between sample preparation and measurements, well-ordered structures were retained at the surface, which pointed to their stability in UHV.

Three typical structures (Figs. 2a, 3a, 4a) were observed in the images of the (410)-O surface obtained with atomic resolution (constant tunneling current mode). These structures corresponded to different states of the probe apex. All three structures were obtained in the same surface area at different times. A regular structure of steps directed along [001] and separated by terraces of width $7.2 \pm 0.2$ Å is seen in all the images. This distance between the steps corresponds to terraces with four atomic rows. The distance between the neighboring atoms along a step is $3.6 \pm 0.2$ Å. The measured distances are in good agreement with the sizes of the unreconstructed Cu(410) surface with (100) terraces containing four atomic rows in the [001] direction. Nevertheless, each of the STM images presented in Figs. 2a, 3a, and 4a bears different information on the structure of the terraces on the vicinal surface. An image of three atomic rows (trimers) is seen in Fig. 2a (Fig. 2b demonstrates the corresponding quasi-3D
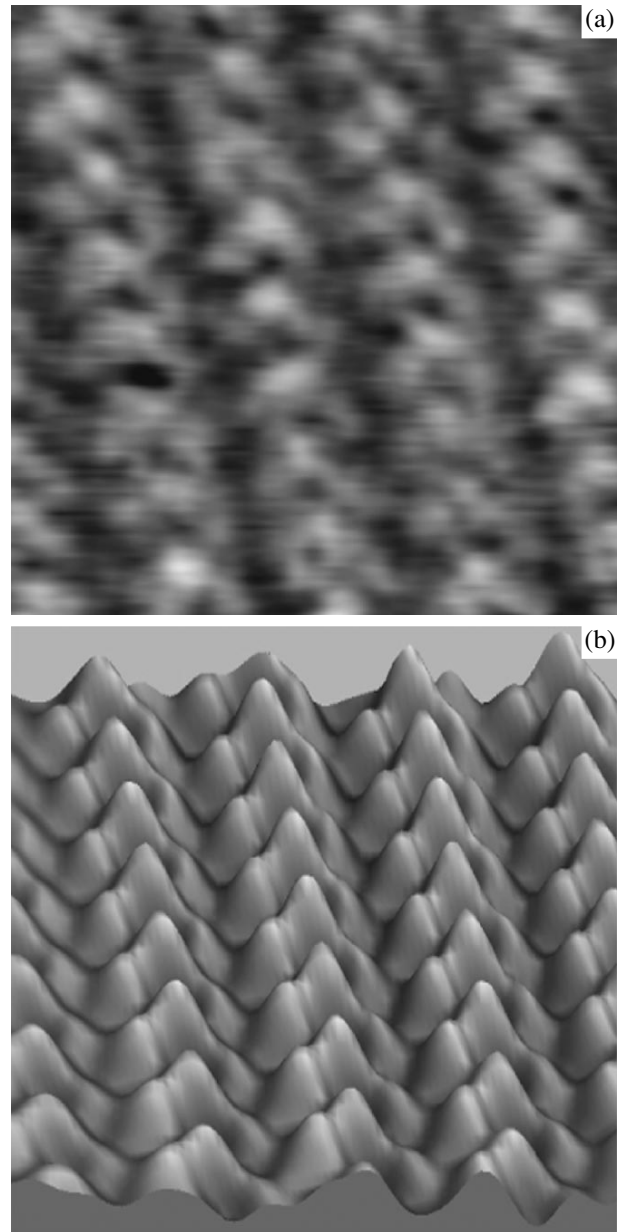


**Fig. 2.** (a) $30 \times 28$ Å STM image of the Cu(410)-O surface in which three rows of copper atoms are visualized within a terrace ($U_{tun} = -10$ mV, $I_{tun} = 0.2$ nA) and (b) the corresponding 3D image after Fourier filtering of noise.

image after Fourier filtering of noise). The surface images in Fig. 4a and in the upper part of Fig. 3a consist of dimers the distance between which also corresponds to the period of the unreconstructed Cu(410) surface. The distance between the rows within the dimer structure was $3.1 \pm 0.2$ Å (Fig. 3a) and $3.3 \pm 0.2$ Å (Fig. 4a). The 3D images in Figs. 3b and 4b emphasize the difference between the presented dimer structures. In one of them (Fig. 4b), the atomic corrugations in rows are comparable, while those in the other one (Fig. 3b) differ
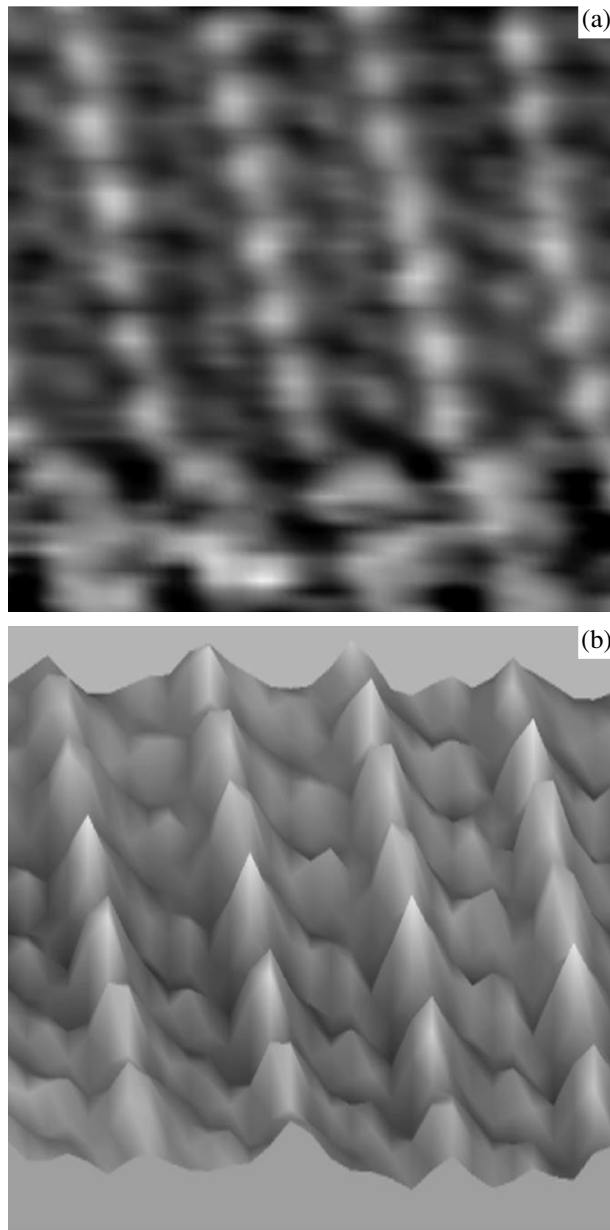
**Fig. 3.** (a) $30 \times 28$-Å STM image demonstrating two rows of copper atoms within a terrace ($U_{tun} = -5$ mV, $I_{tun} = 0.1$ nA) and (b) the $30 \times 21$ Å 3D image of the upper part of the frame after Fourier filtering.
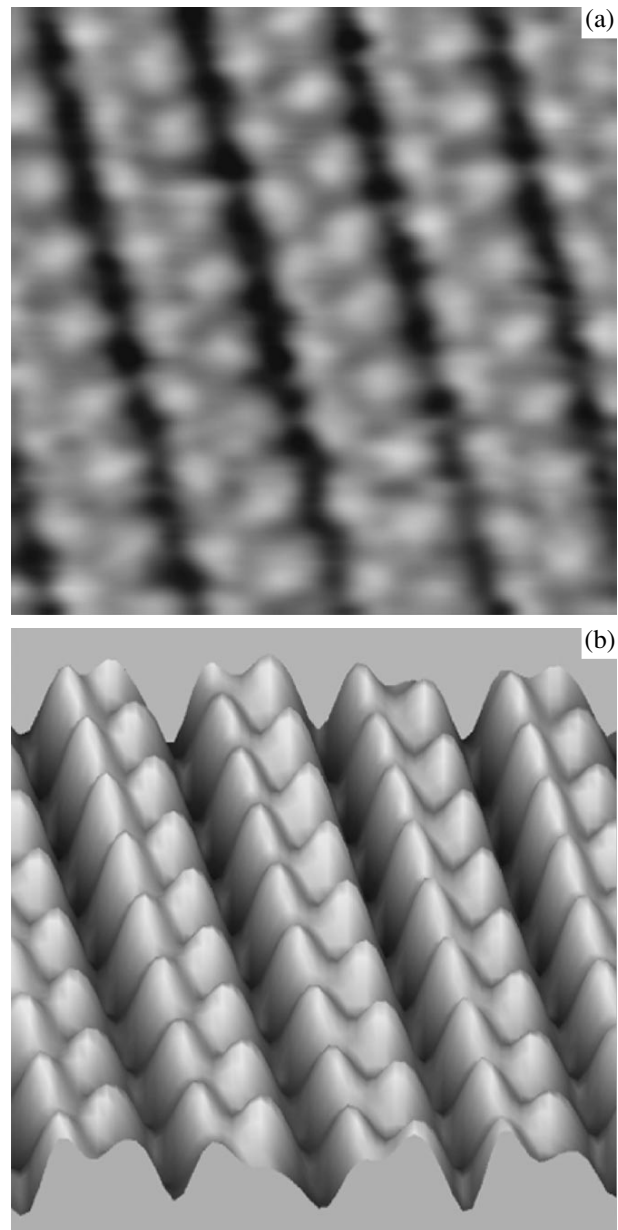
**Fig. 4.** (a) $30 \times 28$-Å image demonstrating the arrangement of oxygen atoms on the Cu(410)-O surface ($U_{tun} = -2$ mV, $I_{tun} = 0.12$ nA) and (b) the corresponding 3D image after Fourier filtering.

substantially, because of which one of the rows becomes more pronounced.

The atomic structure of the reconstructed Cu(410)-O surface was the subject of a number of investigations [3–5, 7, 9]. In accordance with the x-ray diffraction [9] and STM [3, 7] data, various models were proposed for the Cu(410)-O structure with a missing row of copper atoms in the middle of the terrace and near a step and also the overlayer model without a missing row. However, the accurate surface structure has remained controversial so far. In all the models, it was suggested that

oxygen atoms are arranged between copper atoms in the first and third terrace rows in such a way that chains of oxygen and copper atoms form in the [001] direction. STM images of the Cu(410)-O surface similar to those presented in Figs. 2–4 were obtained by the authors of [3, 7] and were interpreted in favor of the model with one missing row under the suggestion that oxygen atoms are invisible in STM images. According to this suggestion, the most geometrically perfect tips demonstrate (like the image in Fig. 2a) an arrangement of copper atoms inside a terrace with three filled and

one missing row. However, x-ray diffraction data and density-functional calculations published subsequently [9] indicated that the overlayer model of the Cu(410)-O surface is more preferable than the missing-row models.

We managed to obtain images corresponding to three different states of the probe apex during the scanning of one frame (Fig. 5). The tunneling voltage and current and the frame recording rate were not varied during scanning; therefore, the change in the terrace structure (from two rows to one, then to three, and back to two) can be associated only with a change in the state of the tip during scanning. Unfortunately, we did not manage to select scanning parameters at which the image of atoms would be of equal quality for different probe states within one frame. Nevertheless, it is seen in the presented figure that the positions of two rows of the structure in area *1* of Fig. 5 coincide (with an accuracy of small lateral displacements) with the first and third rows of atoms in area *3* and that the position of one row in area *2* coincides with minima in areas *1* and *3* when the corresponding areas of the STM images are matched. A similar behavior is also seen in Fig. 3a, which demonstrates terraces with one pronounced row after switching of the probe state. Because the surface area structure (Fig. 5) is independent of the probe state and does not change substantially over time (which is evidenced by the images reproduced in Figs. 2–4), we prove the suggestion of the possibility of discrimination of atoms of one or another sort in relation with a change in the probe apex state that was made on the basis of studies of the O/Cu(100) [13], S/Cu(110) and O/Cu(110) [14]. In this case, it might be expected that the STM images of the Cu(410)-O surface obtained at different states of the tip reflect the arrangement of copper and oxygen atoms on the surface. Assuming that the probe in different states visualizes different surface atoms, we imposed images in Figs. 2–4 on the corresponding areas in Fig. 5 and obtained the surface model presented in Fig. 6. Comparing the obtained model with the models proposed earlier [3, 9] and with the structure of the perfect Cu(410) surface, one can draw the conclusion that Fig. 2a presents an image of the first three rows of copper atoms, Fig. 3a presents the fourth row of copper atoms, and Fig. 4a shows oxygen atoms that are arranged with small lateral displacements with respect to the positions of bulk crystal lattice sites in the first and third rows. Because the Cu–O bond lengths in oxides and on reconstructed copper surfaces equal 1.8–1.95 Å [10, 15], it can be suggested that oxygen atoms in rows are arranged between copper atoms, forming Cu–O–Cu–O chains in the first and third rows of terraces.

Thus, the presented results count in favor of the overlayer model. The positions of various atoms in the surface plane were determined by the results of superposition (see table). For comparison, the coordinates of atoms in the overlayer model obtained on the basis of x-ray diffraction data [9] are given in the right-hand
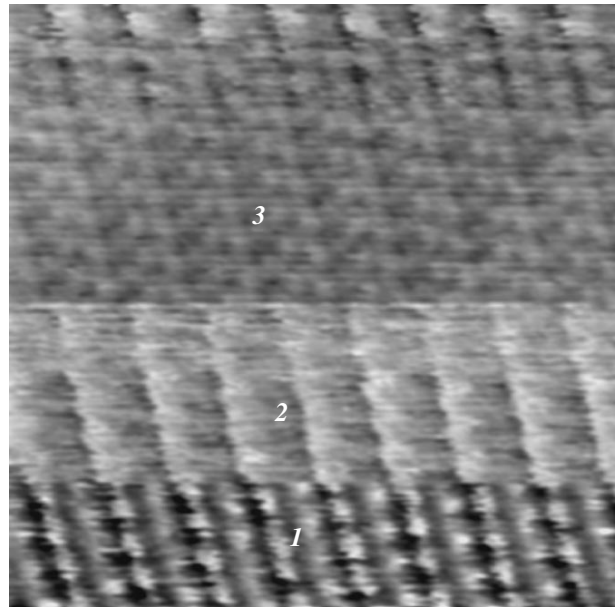


**Fig. 5.** The $61 \times 61$-Å STM image ($U_{tun} = -2$ mV, $I_{tun} = 0.12$ nA) demonstrating a change of contrast associated with a change in the tip state. Two rows of atoms are seen in the lower part (*1*) of the frame, one pronounced row is seen in area *2*, and three rows of atoms are seen in area *3* within terraces.
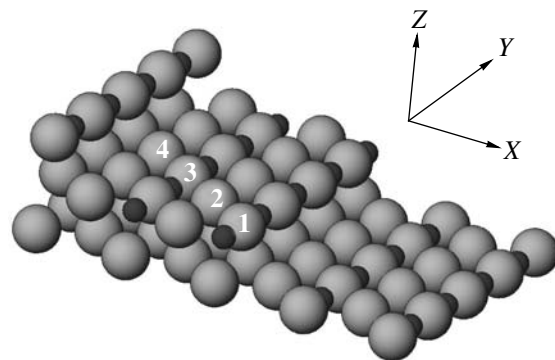


**Fig. 6.** Overlayer model of the Cu(410)-O surface structure. Light and black circles designate copper and oxygen atoms, respectively.

column. In spite of a discrepancy in the absolute values of displacements calculated by the STM image in Fig. 5, a reasonable agreement with the results obtained in [9] is evident. The correct position of atoms along the normal to the surface plane cannot be obtained from the results of superposition because, as a result of a change in the probe state, (1) a vertical displacement of the image of the surface area as a whole is probable because of the change in tunneling conditions and (2) atoms occupying nonequivalent positions are revealed in STM images differently, which is evidenced by our

Positions of copper and oxygen atoms on the terraces of the Cu(410)–O structure as obtained from the STM data (Fig. 5) in comparison with the diffraction data [9]. The displacements of the atoms with respect to the unreconstructed (410) surface are presented [9]

| Row no. | Atom | $\Delta x$ (Å) | XRD [9] | |
|---------|------|------|------|------|
| | | | $\Delta x$ (Å) | $\Delta z$ (Å) |
| 1 | Cu | −0.2 | −0.1 | 0.15 |
| 1 | O | 0.4 | 0.06 | 0.04 |
| 2 | Cu | 0 | 0.17 | 0.27 |
| 3 | Cu | 0.4 | 0.14 | 0.07 |
| 3 | O | 0.6 | 0.20 | 0.59 |
| 4 | Cu | 0.5 | 0.02 | −0.08 |

data and the results of investigations at different states of the tip [16]. Substantial relative vertical displacements of oxygen and copper atoms take place on the reconstructed Cu(410)-O surface. For example, oxygen atoms located in the third row are seen in the images higher than those located in the first row, whereas the second row of copper atoms is approximately 0.2 Å higher than the first row. The relative lateral displacements of atoms within individual image areas in Fig. 5 can be determined rather accurately (0.2 Å). The accuracy of the determination of the relative displacements of atoms visualized in different areas of Fig. 5 is significantly lower by virtue of the imperfection of the superposition process.

Different probe states and, as a consequence, visualization of atoms of one or another sort in STM images are evidently associated with the occurrence of oxygen atoms adsorbed on the tip apex. Under ultrahigh vacuum conditions, the occurrence of an oxygen atom on the tip apex is hardly probable. In this case, oxygen atoms arrive at the sample surface through diffusion from the bulk and can jump to the tip apex. Oxygen exchange leads to switching of image modes during scanning. Presumably, the probe state at a certain instant of time in our experiments was determined by the amount of oxygen atoms adsorbed on the tip apex. In this case, the state of the electronic system changed and tunneling was performed through the same atom at the apex, which allowed the surface model to be correctly recovered.

Thus, we studied the structure of the Cu(410)-O surface. The modes of obtaining STM images corresponding to various probe states were used. A procedure for recovering the atomic structure of the surface was proposed. It was shown that the atomic structure of the Cu(410)-O surface corresponds to the overlayer model; i.e., a model without a missing row of copper atoms in the [001] direction.

## REFERENCES

1. F. Jensen, F. Besenbacher, E. Laegsgaard, and I. Stensgaard, Phys. Rev. B **42**, 9206 (1990).

2. Ch. Woll, R. J. Wilson, S. Chiang, *et al.*, Phys. Rev. B **42**, 11 926 (1990).

3. P. J. Knight, S. M. Driver, and D. P. Woodruff, J. Phys.: Condens. Matter **9**, 21 (1997).

4. P. J. Knight, S. M. Driver, and D. P. Woodruff, Chem. Phys. Lett. **259**, 503 (1996).

5. P. J. Knight, S. M. Driver, and D. P. Woodruff, Surf. Sci. **376**, 374 (1997).

6. E. Taglauer, St. Reiter, A. Liegl, and St. Schomann, Nucl. Instrum. Methods Phys. Res. B **118**, 456 (1996).

7. S. Reiter and E. Taglauer, Surf. Sci. **367**, 33 (1996).

8. M. Sotto, Surf. Sci. **260**, 235 (1992).

9. E. Vileg, S. M. Driver, P. Goedtkindt, *et al.*, Surf. Sci. **516**, 16 (2002).

10. I. K. Robinson, E. Vileg, and S. Ferrer, Phys. Rev. B **42**, 6954 (1990).

11. V. F. Gantmakher, V. A. Gasparov, T. I. Kulesko, and V. N. Matveev, Zh. Éksp. Teor. Fiz. **63**, 1752 (1972) [Sov. Phys. JETP **36**, 925 (1973)].

12. M. Wuttig, R. Franchy, and H. Ibah, Surf. Sci. **213**, 103 (1989).

13. F. M. Leibsle, Surf. Sci. **337**, 51 (1995).

14. L. Ruan, F. Besenbacher, I. Stensgaard, and E. Laegsgaard, Phys. Rev. Lett. **70**, 4079 (1993).

15. G. Dorenbos, M. Breeman, and D. O. Boerma, Phys. Rev. B **47**, 1580 (1993).

16. A. R. H. Clarke, J. B. Pethica, J. A. Nieminen, *et al.*, Phys. Rev. Lett. **76**, 1276 (1996).

*Translated by A. Bagatur'yants*

# Enhancement of Superconductivity in Disordered Films by Parallel Magnetic Field[¶]

## M. Yu. Kharitonov[a, b] and M. V. Feigelman[a]

*[a] Landau Institute for Theoretical Physics, Russian Academy of Sciences, Moscow, 119334 Russia*
*[b] Ruhr-Universität Bochum, 44801 Bochum, Germany*
Received July 27, 2005

We show that the superconducting transition temperature $T_c(H)$ of a very thin highly disordered film with strong spin–orbital scattering can be increased by a parallel magnetic field $H$. This effect is due to the polarization of magnetic impurity spins, which reduces the full exchange scattering rate of electrons; the largest effect is predicted for spin-1/2 impurities. Moreover, for some range of magnetic impurity concentrations, the phenomenon of *superconductivity induced by magnetic field* is predicted: the superconducting transition temperature $T_c(H)$ is found to be nonzero in the range of magnetic fields $0 < H^* \leq H \leq H_c$. © 2005 Pleiades Publishing, Inc.

PACS numbers: 74.25.Ha, 74.78.–w, 74.78.Na

The problem of superconducting alloys with magnetic impurities was addressed long ago by Abrikosov and Gor'kov (AG) [1]. They have shown that superconductivity (SC) is suppressed due to exchange scattering (ES) of electrons on magnetic impurities, with the transition temperature $T$ determined from the equation (hereafter, we employ units in which $\hbar = 1$)

$$\ln\frac{T_{c0}}{T} = \pi T \sum_{\varepsilon}\left(\frac{1}{|\varepsilon|} - \frac{1}{|\varepsilon| + \nu_S}\right). \qquad (1)$$

Here, $\varepsilon = 2\pi T(m + 1/2)$ is the fermionic Matsubara frequency ($m$ is integer), $T_{c0}$ is the transition temperature of a clean sample, and $\nu_S = 2\pi N_F n_S J^2 S(S + 1)$ is the ES rate of electrons on magnetic impurities ($N_F$ is the normal metal density of states per single spin state, $n_S$ is the concentration of magnetic impurities, $J$ is the exchange coupling constant, and $S$ is the impurity spin length). The solution of (1) yields the function $T = T_{AG}(\nu_S)$. There exists a critical point at which the transition temperature is suppressed down to zero, the critical scattering rate being $\nu_S^* = \pi/(2e^C)T_{c0} = 0.882T_{c0}$, where $C = 0.577$ is the Euler constant. The critical concentration, corresponding to $\nu_S^*$, is further denoted by $n_S^*$. We emphasize that $\nu_S$ is the *full* ES rate; i.e., the sum of the spin-flip scattering rate $2\pi N_F n_S J^2(\langle S_x^2 \rangle + \langle S_y^2 \rangle) = 2/3\nu_S$ and the rate of scattering without spin flip $2\pi N_F n_S J^2 \langle S_z^2 \rangle = 1/3\nu_S$.

The results of AG were derived for unpolarized magnetic impurity spins. In this Letter we investigate how the polarization of impurity spins affects the ES mechanism of SC suppression. We show that polariza-tion of magnetic impurity spins by an external magnetic field reduces the full ES rate $\Gamma(\varepsilon)$. It reaches its minimal value $\nu_\infty = \nu_S S/(S + 1) < \nu_S$ at an infinite field, when the impurity spins are completely polarized and spin-flip processes have frozen out. This reduction is due to quantum fluctuations of impurity spins; thus, it is strongest for $S = 1/2$ and vanishes in the limit $S \gg 1$.

If ES were *the only* mechanism of SC suppression in nonzero magnetic field $h = \mu_B H$, the transition temperature $T_c^\circ(h)$ would always be higher than $T_c(h = 0) = T_{AG}(\nu_S)$, determined by result of (1). $T_c^\circ(h)$ is a growing function, approaching the value $T_\infty = T_{AG}(\nu_\infty)$ at very high fields $h \longrightarrow \infty$. The transition temperature increase $T_c^\circ(h) - T_c(0)$ comparable to $T_\infty - T_c(0)$ is attained in the field range $h \gtrsim T_c^\circ(h)$. However, apart from ES, there are other mechanisms of SC suppression by magnetic field, namely, the paramagnetic effect (PE) and the orbital effect (OE). Thus, to observe an increase $T_c(h) > T_c(0)$ in the actual transition temperature, PE and OE should be small compared to ES in the field range $h \sim T_c(h)$. Strong reduction of PE is achieved in the presence of high spin–orbital scattering rate $\nu_{so} \gg T_{c0}$ [2–4]. OE is suppressed for a thin-film (thickness $d$ shorter than the magnetic length $l_H = \sqrt{c/eH}$) with parallel orientation of external magnetic field [5].

In this Letter, we show that the increase in the transition temperature can be observed if two quite stringent conditions on the smallness of PE and OE are met. First, the spin–orbit scattering rate $\nu_{so}$ must be sufficiently high:

$$\nu_{so}/\nu_S \gg \zeta^2. \qquad (2)$$

---

[¶] The text was submitted by the authors in English.
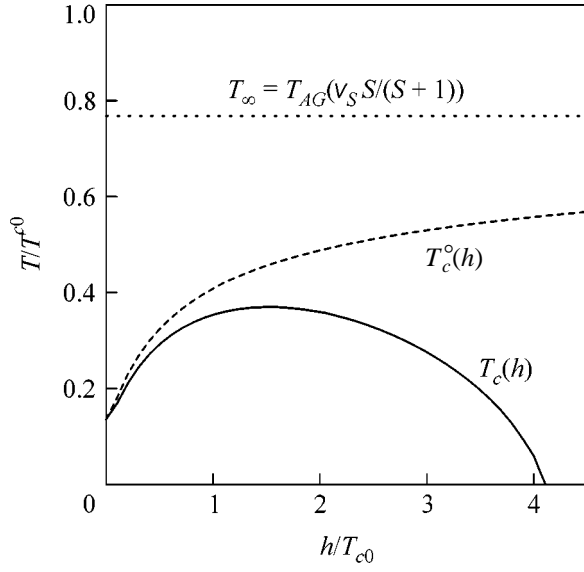
**Fig. 1.** Enhancement of superconductivity by magnetic field. $T_c(h)$ is the transition temperature as a function of magnetic field with PE and OE taken into account (solid line). The area under $T_c(h)$ curve corresponds to the superconducting state. $T_c^\circ(h)$ is the transition temperature with PE and OE disregarded (dashed line), $T_\infty = T_c^\circ(\infty)$ (dotted line). The parameters used are $\nu_S = 0.85 T_{c0} < \nu_S^*$, $S = 1/2$, $J < 0$ (ferromagnetic exchange), $\zeta = 5$, $\nu_{so} = 10^3 T_{c0}$, $\nu = 10^4 T_{c0}$, $p_F d = 30$, $T_c(0) = 0.135 T_{c0}$, $T_\infty = 0.768 T_{c0}$.
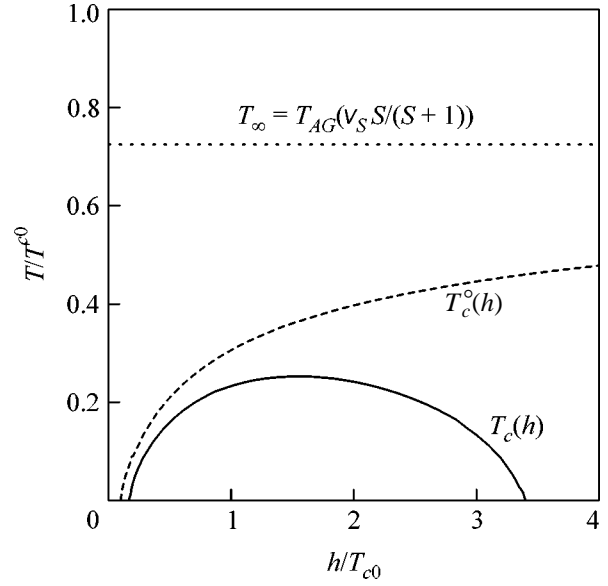
**Fig. 2.** Magnetic-field-induced superconductivity. $T_c(h)$ is the transition temperature as a function of magnetic field with PE and OE taken into account (solid line). The area under the $T_c(h)$ curve corresponds to the superconducting state. $T_c^\circ(h)$ is the transition temperature with PE and OE disregarded (dashed line); $T_\infty = T_c^\circ(\infty)$ (dotted line). The parameters used are $\nu_S = 1.0 T_{c0} > \nu_S^*$, $S = 1/2$, $J < 0$ (ferromagnetic exchange), $\zeta = 5$, $\nu_{so} = 10^3 T_{c0}$, $\nu = 10^4 T_{c0}$, $p_F d = 30$, $h^* = 0.17 T_{c0}$, $T_\infty = 0.725 T_{c0}$.

Here, $\zeta = n_S |J| S / \nu_S = (2\pi N_F |J| (S + 1))^{-1} \gg 1$ is the inverse Born parameter for the exchange scattering. Second, the elastic scattering rate $\nu$ and thickness of the film $d$ must satisfy the condition

$$1 \lesssim (p_F d)^2 \ll \nu / T_{c0}, \qquad (3)$$

where $p_F$ is the Fermi momentum.

We distinguish between two different regimes depending on the value of ES rate $\nu_S$. If $\nu_S < \nu_S^*$, i.e., if there exists a finite transition temperature $T_c(0) = T_{AG}(\nu_S)$ at zero field, then, provided that the conditions (2) and (3) on PE and OE are met, the increase $T_c(h) > T_c(0)$ in the transition temperature in some range of $h$ is expected (see solid line in Fig. 1). The growth of $T_c(h)$ at $h \lesssim T_c(h)$ is due to the reduction of the full ES rate. At higher fields, PE and OE inevitably prevail, leading to complete suppression of SC at some critical field $h_c$. The most favorable regime for the observation of $T_c(h)$ increase is when SC is significantly suppressed at zero field, i.e., when $\nu_S$ is close to (but smaller than) $\nu_S^*$. In this case, a large ratio $(T_c^{max} - T_c(0))/T_c(0)$ is expected (see Fig. 1).

The most exotic situation occurs when $\nu_S > \nu_S^* > \nu_\infty = \nu_S S / (S + 1)$. Then, at $h = 0$, superconductivity is totally suppressed. Disregarding PE and OE, one obtains a finite transition temperature $T_\infty = T_{AG}(\nu_\infty)$ at very high fields (indicated by the dotted line in Fig. 2). If the conditions (2) and (3) are satisfied, superconductivity does not exist below some critical field $h^*$, but it appears at higher fields $h \geq h^*$. A nonzero transition temperature $T_c(h)$ (the solid line in Fig. 2) exists in a range of fields starting from $h^*$ and terminating at some higher critical field $h_c$, when PE and OE dominate over ES. Such behavior is possible in the range of concentrations $n_S^* < n_S < n_S^{**}$, where $n_S^{**}$ is smaller than $n_S^* (S + 1)/S$ and is determined by the parameters involved in PE and OE. The better the conditions (2) and (3) are satisfied, the closer is $n_S^{**}$ to $n_S (S + 1)/S$. The most favorable situation for the experimental observation of magnetic-field-induced superconductivity is realized when $n_S$ is only slightly larger than $n_S^*$. In this case, $h^*$ is sufficiently small and the curve $T_c(h)$ produces quite a steep growth at the fields $h$ just above $h^*$ (see Fig. 2). Two specific examples of $T_c(h)$ behavior are presented in Figs. 1 and 2 for $S = 1/2$, for the following set of parameters: $J < 0$ (ferromagnetic exchange), $\zeta = 5$,

$\nu_{so} = 10^3 T_{c0}$, $\nu = 10^4 T_{c0}$, $p_F d = 30$. The similar set of parameters corresponds, for example, to the 3-nm-thick PtSi film studied in [6, 7].

Below, we briefly outline the method used to derive the announced results; details of our calculations will be presented in a separate publication.

The starting point of our problem is the following Hamiltonian:

$$\mathcal{H} = \mathcal{H}_{BCS} + \mathcal{H}_S + \mathcal{H}_{eS} + \mathcal{H}_{eU}.$$

Here,

$$\mathcal{H}_{BCS} = \int \left\{ \psi_\alpha^\dagger \left( \frac{1}{2m}(\mathbf{p} - e/c\mathbf{A})^2 - \varepsilon_F \right) \psi_\alpha \right.$$

$$\left. + \frac{\lambda}{2} \psi_\alpha^\dagger \psi_\beta^\dagger \psi_\beta \psi_\alpha - \psi_\alpha^\dagger \sigma_{\alpha\beta}^z h \psi_\beta \right\} d\mathbf{r}$$

is the BCS Hamiltonian which includes the orbital and paramagnetic effects of external magnetic field on conduction electrons;

$$\mathcal{H}_{eS} = \int \left\{ \psi_\alpha^\dagger \sum_a (u_S \delta_{\alpha\beta} + J(\mathbf{S}_a, \sigma_{\alpha\beta})) \delta(\mathbf{r} - \mathbf{R}_a) \psi_\beta \right\} d\mathbf{r}$$

describes the interaction with magnetic impurities; and $\mathcal{H}_S = -\sum_a \omega_S S_a^z$ is the Hamiltonian of impurity spins in external magnetic field ($\omega_S = g_S h = 2h$ is their Zeeman splitting). Finally,

$$\mathcal{H}_{eU} = \int \left\{ \psi_\alpha^\dagger(\mathbf{r}) \sum_b v_{\alpha\beta}(\mathbf{r} - \mathbf{R}_b, \mathbf{r}' - \mathbf{R}_b) \psi_\beta(\mathbf{r}') \right\} d\mathbf{r} d\mathbf{r}'$$

describes the scattering of electrons on nonmagnetic impurities, which includes both potential and spin–orbit parts. Here $v_{\alpha\beta}(\mathbf{r}, \mathbf{r}')$ is the Born amplitude in coordinate representation; since we work in momentum space, we only need its Fourier transform $v_{\alpha\beta}(\mathbf{p}, \mathbf{p}') = u_0 \delta_{\alpha\beta} + i v_{so}/p_F^2 ([\mathbf{p}, \mathbf{p}'], \sigma_{\alpha\beta})$. Magnetic and nonmagnetic impurities are uniformly distributed over the sample volume with concentrations $n_S$ and $n$, respectively.

We solve the problem using the standard diagrammatic technique for BCS theory and disordered metals [1, 8] and employing the following approximations:

(i) $p_F l \gg 1$, where $l = v_F/\nu$ is the mean free path for potential scattering;

(ii) the Born approximation for impurity scattering;

(iii) a "dirty limit," i.e., $\nu \gg \nu_{so} \gg T_c$.

The equation for the transition temperature $T$ can be obtained in the form

$$\ln \frac{T_{c0}}{T} = \pi T \sum_\varepsilon \left( \frac{1}{|\varepsilon|} - C_0(\varepsilon) \right), \tag{4}$$

where $C_0(\varepsilon) = 1/2(C_{\downarrow\downarrow}^{\uparrow\uparrow} - C_{\downarrow\uparrow}^{\uparrow\downarrow} + C_{\uparrow\uparrow}^{\downarrow\downarrow} - C_{\uparrow\downarrow}^{\downarrow\uparrow})$ is the singlet Cooperon component. In the approximation $p_F l \gg 1$ the Cooperon is given by an infinite sum of ladder-type diagrams, each "ladder step" containing an impurity line and the product of two disorder-averaged normal state Green's functions. The expression for the components of such a Green's function with electron spin directed along ($\uparrow$) the external field $h$ and in the opposite direction ($\downarrow$) reads

$$G_{\uparrow,\downarrow}^{-1}(\varepsilon, \mathbf{p}) = i\varepsilon - \xi \pm h'$$

$$+ \frac{i}{2}(\nu + \nu_{so} + \Gamma\varepsilon)) \operatorname{sgn}\varepsilon \pm i\tilde{\nu}_S \operatorname{sgn}\varepsilon.$$

Here, $\nu = 2\pi N_F(n_S u_S^2 + n u_0^2)$ is the potential scattering rate, $\nu_{so} = 2\pi N_F n v_{so}^2 2/3$ is the spin–orbit scattering rate, $\tilde{\nu}_S = 2\pi N_F n_S u_S J \langle S_z \rangle$ is the interference contribution between potential and exchange scattering on magnetic impurities (however, this term is irrelevant and falls out of the final result), and $h' = h - n_S J \langle S_z \rangle$ is the effective magnetic field acting on electron spins comprised of the external field $h$ and exchange field of polarized impurities $-n_S J \langle S_z \rangle$. Hereafter, $\langle \ldots \rangle$ stands for thermodynamic averaging over the states of an isolated impurity spin subjected to external magnetic field $h$: $\langle \hat{A} \rangle = 1/Z \sum_{m=-S}^S A_{mm} e^{m\omega_S/T}$, $Z = \sum_{m=-S}^S e^{m\omega_S/T}$. Thus,

$$\langle S_z \rangle = \left( S + \frac{1}{2} \right) \coth \left[ \left( S + \frac{1}{2} \right) \frac{\omega_S}{T} \right] - \frac{1}{2} \coth \frac{\omega_S}{2T}.$$

Further, $\Gamma(\varepsilon) = \nu_z + \Gamma_{sf}(\varepsilon)$ is the full ES rate due to exchange interaction of electrons with polarized magnetic impurities. It is given by the sum of the rate of scattering without spin flip $\nu_z = \nu_S \langle S_z^2 \rangle / S(S+1)$ and the spin-flip scattering rate

$$\Gamma_{sf}(\varepsilon) = \nu_S \frac{\langle S_\perp^2 \rangle}{S(S+1)} - \delta\Gamma(\varepsilon), \tag{5}$$

where

$$\delta\Gamma(\varepsilon) = \nu_S \frac{\langle S_z \rangle}{S(S+1)} T \sum_{|\omega| > |\varepsilon|} \frac{2\omega_S}{\omega^2 + \omega_S^2}. \tag{6}$$

Here, $\omega = 2\pi T n$ is the bosonic Matsubara frequency ($n$ is integer) and $S_\perp^2 = S_x^2 + S_y^2$.

We now discuss the properties of the full exchange scattering rate $\Gamma(\varepsilon) = \nu_z + \Gamma_{sf}(\varepsilon)$ and then use the knowl-

edge of this function while determining $T_c(h)$. For $|\varepsilon| \gg \omega_S$ at any ratio $\omega_S/T$, we have $\Gamma_{sf}(\varepsilon) \approx \nu_S \langle S_\perp^2 \rangle / S(S+1)$ and $\Gamma(\varepsilon) \approx \nu_S$. At zero field $\Gamma_{sf}(\varepsilon) = 2/3\nu_S$, $\nu_z = 1/3\nu_S$, and $\Gamma(\varepsilon) = \nu_S$ for any $\varepsilon$. The full ES rate $\Gamma(\varepsilon) \approx \nu_S$ for electrons with energies $|\varepsilon| \gg \omega_S$ is not modified by the magnetic field, although $\Gamma_{sf}(\varepsilon)$ and $\nu_z$ do depend on $h$.

Consider the limit of strong polarization $\omega_S \gg T$. In this case, one can replace in (6) the sum over $\omega$ by the integral and obtain

$$\Gamma_{sf}(\varepsilon) = \nu_S \frac{1}{S+1} \frac{2}{\pi} \arctan \frac{|\varepsilon|}{\omega_S} \quad \text{and} \quad \nu_z = \nu_S S/(S+1). \quad (7)$$

For electron energies $|\varepsilon| \ll \omega_S$ less than the Zeeman splitting $\Gamma_{sf}(\varepsilon) \approx \nu_S \frac{1}{S+1} \frac{2}{\pi} \frac{|\varepsilon|}{\omega_S} \ll \nu_S$ reflecting the fact that spin-flip processes freeze out for strongly polarized spins. Hence, the full ES rate $\Gamma(\varepsilon) \approx \nu_z = \nu_S S/(S+1) < \nu_S$ in a wide range of energies $|\varepsilon| \lesssim \omega_S$. At very strong field $\Gamma_{sf}(\varepsilon) \longrightarrow 0$ and $\Gamma(\varepsilon) = \nu_\infty = \nu_S S/(S+1)$ for all $\varepsilon$. Expressing $\Gamma(\varepsilon)$ in the form $\Gamma(\varepsilon) = \nu_S - \delta\Gamma(\varepsilon)$, we see that the full ES rate in nonzero field is always less than $\nu_S$, with $\delta\Gamma(\varepsilon, \omega_S)$ for a fixed $\varepsilon$ being a growing function of $\omega_S$ with limiting values $\delta\Gamma(\varepsilon, 0) = 0$, $\delta\Gamma(\varepsilon, \infty) = \nu_S/(S+1)$.

The Cooperon can be shown to obey the following equation for $C_0(\varepsilon)$:

$$\left( |\varepsilon| + \Gamma(\varepsilon) + \frac{1}{2}(\hat{L}_0 - \Gamma_{sf}(\varepsilon)) + \frac{3h'^2}{2\nu_{so}} + \gamma_{orb} \right) C_0 = 1. \quad (8)$$

Here,

$$\gamma_{orb} = \frac{1}{2} D \left( \frac{2e}{c} H \right)^2 \frac{d^2}{12} = \frac{2}{9} (p_F d)^2 \frac{h^2}{\nu}$$

is the dephasing rate corresponding to OE of the magnetic field ($D = 1/3\nu_F l$ is the diffusion constant) and the operator $\hat{L}_0$ acts as

$$\hat{L}_0 C_0(\varepsilon) = \nu_S \frac{\langle S_z \rangle}{S(S+1)} T \sum_\omega \frac{2\omega_S}{\omega^2 + \omega_S^2} C_0(\varepsilon - \omega).$$

At zero field $h = 0$, it is straightforward to check that $\hat{L}_0 - \Gamma_{sf}(\varepsilon) = 0$ and $\Gamma(\varepsilon) = \nu_S$. Therefore, the solution to (8) is $C_0(\varepsilon) = 1/(|\varepsilon| + \nu_S)$ and one recovers result (1) for the transition temperature.

**Enhancement of $T_c$ by parallel field.** We start our analysis from the case $\nu_S < \nu_S^*$, when a nonzero transition temperature $T_c(0) = T_{AG}(\nu_S)$ exists at zero field. First we study the equation

$$\left( |\varepsilon| + \nu_S - \delta\Gamma(\varepsilon) + \frac{1}{2}(\hat{L}_0 - \Gamma_{sf}(\varepsilon)) \right) C_0 = 1 \quad (9)$$

leaving in (8) the terms related to ES only and neglecting PE and OE. In the limit $h \longrightarrow \infty$ we get $\hat{L}_0 \longrightarrow 0$, $\Gamma_{sf}(\varepsilon) \longrightarrow 0$, $\Gamma(\varepsilon) \longrightarrow \nu_\infty$, and $C_0(\varepsilon) = 1/(|\varepsilon| + \nu_\infty)$. Thus, in the strong-field limit and in the absence of PE and OE, the transition temperature would be $T_\infty = T_{AG}(\nu_\infty)$ (indicated by the dotted line in Fig. 1), which is higher than the zero-field value $T_{AG}(\nu_S)$ since $\nu_\infty < \nu_S$. For an arbitrary field, solving Eqs. (4) and (9) together numerically, one obtains the transition temperature curve $T_c^\circ(h)$ with PE and OE disregarded (the dashed line in Fig. 1). Formally, the enhancement of transition temperature compared to the zero-field result of AG $T_{AG}(\nu_S)$ is due to the term $-\delta\Gamma(\varepsilon)$ in (9), whose effect is always stronger than the (opposite-sign) effect from the term operator $1/2(\hat{L}_0 - \Gamma_{sf}(\varepsilon))$ in the same equation.

We are now in position to derive conditions (2) and (3) for the strengths of paramagnetic and orbital effects compatible with observation of an increase of the actual transition temperature $T_c(h)$. Indeed, the terms in (8) related to PE and OE must be sufficiently smaller than the terms responsible for ES in the relevant fields $h \sim T_{c0}$: $[h'(h \sim T_{c0})]^2/\nu_{so} \ll \nu_S$ and $\gamma_{orb}(h \sim T_{c0}) \ll \nu_S$. Since we are interested in $\nu_S \sim T_{c0}$ the latter condition immediately leads to (3). Due to the Born approximation ($\zeta \gg 1$) for $h \sim T_{c0}$ and $T \lesssim T_{c0}$, the exchange field $n_S J \langle S_z \rangle$ dominates over $h$ in the effective field $h'$ and is on the order of its maximal value $n_S JS$. Therefore, estimating $h' \sim n_S JS$, we obtain (2). Thus, provided conditions (2) and (3) are satisfied, one observes an increase in the transition temperature $T_c(h)$ (solid line in Fig. 1).

**Superconductivity induced by magnetic field.** Now we turn to the case $\nu_S > \nu_S^* > \nu_\infty$ or, expressed in terms of magnetic impurity concentrations, $n_S^* < n_S < n_S^* (S+1)/S$. First we study Eqs. (4) and (9) neglecting PE and OE. Since $\nu_S > \nu_S^*$, the SC is totally suppressed at $h = 0$, but at infinite field one obtains a finite transition temperature $T_\infty = T_{AG}(\nu_\infty)$ (indicated by dotted line in Fig. 2), because $\nu_\infty < \nu_S^*$. This leads to the existence of a critical field $h_o^*$, below which SC does not exist at any temperature but appears in greater fields $h \geq h_o^*$. The field $h_o^*$ is determined from the equation

$$\int_0^\infty d\varepsilon (C_0(\varepsilon, h) - 1/(\varepsilon + \nu_S^*)) = 0, \quad (10)$$

where $C_0(\varepsilon, h)$ is the solution to (9) in the zero-temperature limit and depends on only one parameter, $\nu_S$. The transition temperature $T_c^\circ(h)$ in the absence of PE and OE (dashed line in Fig. 2) is a growing function of $h$, starting from the zero value $T_c^\circ(h_o^*) = 0$ at $h_o^*$ and tending to $T_\infty$ as $h \longrightarrow \infty$. The critical field $h_o^*$ as a

function of $n_S$ has the following limiting values: $h_\circ^* \longrightarrow 0$ as $n_S \longrightarrow n_S^* + 0$, $h_\circ^* \longrightarrow \infty$ as $n_S \longrightarrow n_S^* (S + 1)/S - 0$; and $h_\circ^* \sim T_{c0}$ when $n_S$ is close neither to $n_S^*$ nor to $n_S^* (S + 1)/S$.

For magnetic impurity concentrations $n_S$ not very close to $n_S^* (S + 1)/S$, the field $h_\circ^* \lesssim T_{c0}$. Then, provided conditions (2) and (3) are met, the described behavior of the transition temperature in fields $h \sim h_\circ^*$ survives under the action of orbital and paramagnetic effects. PE and OE slightly change $h_\circ^*$, making the actual critical field $h^*$ greater than $h_\circ^*$. The actual transition temperature curve $T_c(h)$ (solid line in Fig. 2) is close to $T_c^\circ (h)$ at fields $h \sim h^*$ and deviates significantly only at higher fields, when PE and OE dominate over ES. We found the critical field $\omega_S^* = g_S h^*$ analytically (with logarithmic accuracy in $\omega_S^* / \nu_S^*$) for the case when $n_S$ is slightly greater than critical $n_S^*$, i.e., $\delta\nu_S = \nu_S - \nu_S^* \ll \nu_S^*$:

$$\frac{\omega_S^*}{\nu_S^*} \ln\frac{\nu_S^*}{\omega_S^*} = \pi(S + 1)\left[\frac{\delta\nu_S}{\nu_S^*} + \frac{3(n_S JS)^2}{2\nu_{\mathrm{so}}\nu_S^*}\right]. \qquad (11)$$

If $h_\circ^* \gg T_{c0}$, i.e., if $n_S$ is close to $n_S^* (S + 1)/S$, accounting for PE and OE, even with conditions (2) and (3) fulfilled, SC is destroyed in such a high field. Thus, for such $n_S$, SC is totally suppressed at any field. This yields that the regime of "magnetic-field-induced SC" actually exists in a narrower (than in the absence of PE and OE) range of concentrations $n_S^* < n_S < n_S^{**}$, where $n_S^{**}$ is smaller than $n_S^* (S + 1)/S$ and is determined by the values of parameters involved in PE and OE.

In conclusion, we have predicted the mechanism of superconductivity enhancement in thin films by external parallel magnetic field. The effect is due to the polarization of magnetic impurity spins, which reduces the full rate of electron exchange scattering. In some range of magnetic impurity concentrations, the phenomenon of *magnetic-field-induced superconductivity* is predicted. The predicted effect is expected to be observable in very thin disordered superconductive films containing heavy metals leading to high spin–orbital scattering rate. We expect that a similar effect may exist in superconductive-ferromagnet thin-film bilayers with spontaneous magnetization parallel to the surface.

## REFERENCES

1. A. A. Abrikosov and L. P. Gor'kov, Zh. Éksp. Teor. Fiz. **39**, 1781 (1960) [Sov. Phys. JETP **12**, 1243 (1961)].

2. K. Maki, Phys. Rev. **148**, 362 (1966).

3. N. R. Werthamer, E. Helfand, and P. C. Hohenberg, Phys. Rev. **147**, 295 (1966).

4. L. P. Gor'kov and A. I. Rusinov, Zh. Éksp. Teor. Fiz. **46**, 1363 (1964) [Sov. Phys. JETP **19**, 922 (1964)].

5. K. Maki, Prog. Theor. Phys. **29**, 603 (1963).

6. Z. D. Kvon, T. I. Baturina, R. A. Donaton, *et al.*, Phys. Rev. B **61**, 11340 (2000).

7. T. I. Baturina, Thesis (Inst. of Semiconductor Physics, Novosibirsk, 2002).

8. A. A. Abrikosov, L. P. Gor'kov, and I. E. Dzyaloshinskiĭ, *Methods of Quantum Field Theory in Statistical Physics* (Fizmatgiz, Moscow, 1962; Prentice-Hall, Englewood Cliffs, N.J., 1963).

# Fano Interference with the Alternating Asymmetry Parameter in Time-Domain Experiments

## O. V. Misochko[a], M. Hase[b], K. Ishioka[b], and M. Kitajima[b]

*[a] Institute of Solid State Physics, Russian Academy of Sciences, Chernogolovka, Moscow region, 142432 Russia*
*e-mail: misochko@issp.ac.ru*
*[b] National Institute for Materials Science, 305-0047 Tsukuba, Japan*
Received August 5, 2005

It has been found that the time-domain reflection signal arising after the excitation of a bismuth single crystal at helium temperature by an ultrashort laser pulse exhibits Fano interference in the presence of the interaction between the lattice and charge degrees of freedom. This property is manifested in the characteristic spectral lineshape of the Fourier-transformed signal, whose asymmetry parameter is a periodic function of the delay time $\tau$ between the pumping and probing pulses. The most interesting property is the change of the sign of the asymmetry parameter when $\tau$ varies, which indicates that time reversal symmetry is broken. Various possible causes of the effect, observed for the first time, are discussed. © 2005 Pleiades Publishing, Inc.

PACS numbers: 42.25.Kb, 63.20.–e, 78.47.+p

Fano interference is one of the paradigms of modern physics that allows investigation of the internal structure of quantum objects. In his fundamental work [1], which is one of the most frequently cited papers in physics, Fano considered the multiparticle problem of the coupling of continuum states with a discrete level and showed that interference distorting the initial spectral characteristics of both the discrete level and continuum is possible in this case. This interference is observed in all kinds of spectroscopy, where various excitations are analyzed [2], and is manifested in the characteristic asymmetric profile of the spectral line that arises when the discrete and continuum spectra overlap and indicates that they are coupled with each other. The Fano formalism enables one to completely describe this interaction in terms of a limited number (only three) of quantities [1]. Since the Fano model is well known, we only briefly outline it. We consider a system consisting of overlapping continuum and the discrete level; see Fig. 1. In this case, the transition probability, which is proportional to the cross section for absorption or scattering, from the initial state to the final one exhibits a characteristic dependence, which can be written for the discrete level $\varepsilon$ in the form

$$I(\varepsilon) = (\varepsilon + q)^2/(1 + \varepsilon^2). \qquad (1)$$

Here, $\varepsilon$ is the dimensionless energy of the transition of the discrete level in units of the damping factor $\Gamma$ and $q$ is proportional to the ratio of the amplitudes $T_\mathrm{d}$ and $T_\mathrm{c}$ of transitions between the discrete states and continuum states, respectively. The quantity $q$ is called the Fano asymmetry parameter, because it determines the resulting spectral lineshape $I(\varepsilon)$ in dependence of the coupling constant $V$. If the excitation of continuum is

absent ($T_\mathrm{d} = 0$, $|q| \longrightarrow \infty$), the spectral line has a symmetric (Lorentzian) shape with the half-width determined by the discrete level lifetime $\Gamma^{-1}$. If the excitation of the discrete level is absent ($T_\mathrm{c} = q = 0$), a symmetric dip (antiresonance) is observed in the spectrum. When both amplitudes are nonzero, an asymmetric spectral line with antiresonance at $\varepsilon = -q$ arises due to the constructive and destructive interferences for energies above and below the discrete-state energy, respectively. It is evident that the position of the antiresonance can be changed only by changing the sign of the asymmetry parameter $q$. In the fundamental work by Fano, $q$ was a
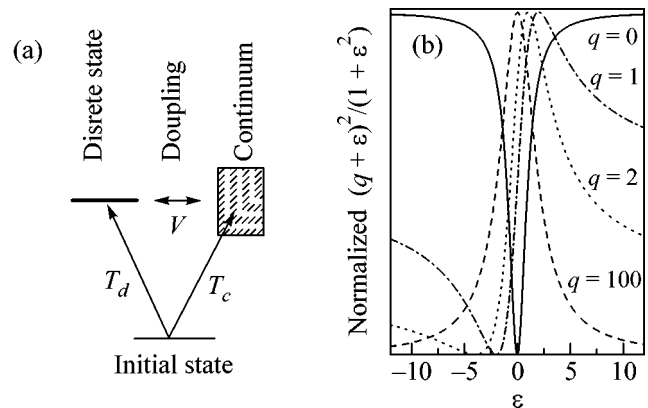


**Fig. 1.** (a) Energy scheme schematically represented Fano interference. (b) The energy dependence of the normalized intensity for several positive values of the asymmetry parameter $q$. The curves for negative $q$ values are obtained by inverting the abscissa axis.

real number, because the amplitudes $T_d$ and $T_c$ determining $q$ were considered as real owing to the use of standing waves instead of traveling waves [2]. However, experiments with a quantum dot placed in one of the arms of an Aharonov–Bohm interferometer [3] showed that this assumption is valid only for systems with time reversal symmetry. When this symmetry is broken, the amplitudes $T_d$ and $T_c$ are complex and thereby the sign (and absolute value) of $q$ can be controlled by external interaction [3, 4]. Until recently, Fano interference was studied only under stationary conditions (frequency domain) [2]. However, increasing interest in investigation of the response of condensed matter to the action of an ultrashort laser pulse provided studies in the time region. In particular, access to ultrafast lattice dynamics, which is ensured by the observation of coherent phonons that are manifested as reflection oscillations [5], shows that Fano interference exists and can be analyzed in the time region [6]. This quantum interference is manifested in the asymmetry of the phonon spectral line obtained by the Fourier transform of a time-oscillating signal and points to the *coherent* interaction between the lattice and charge degrees of freedom in time-domain experiments. Moreover, the use of 10-fs pulses provided recent observation [7] of the production of phonons and evolution of electron–phonon interaction responsible for Fano interference in real time. In this work, we focus on the dynamics of the interaction between charge carriers and phonons that determines the relaxation of a bismuth crystal at helium temperature that is excited by an ultrashort laser pulse under the conditions of the collapse and revival of coherent phonons [8].

The optical response of the Bi single crystal was analyzed for a plane perpendicular to the (0001) trigonal axis. All measurements of coherent phonons were carried out with ultrashort high-energy light pulses at $T = 7$ K. To this end, the radiation of a Ti: sapphire laser ($\lambda = 800$ nm) was transformed by a regenerative solid-state amplifier at whose output pulses had duration $\Delta t \leq 140$ fs and followed with repetition frequency $\nu = 100$ kHz. The pumping and probing laser beams were focused on the crystal surface by a lens with focal length $f = 10$ cm and the 20 : 1 ratio of their intensities was maintained. In this case, the polarizations of the pumping and probing pulses were orthogonal to each other and were parallel to the binary and bisecting axes of the crystal, respectively. The pumping channel was modulated by an optical interrupter with a frequency of 2 kHz and the resonant reflection as a function of the delay time $\tau$ between pumping and probing, which was created by the delay line, was recorded by the synchronous detection of signals recorded by a $p$–$i$–$n$ silicon photodiode.

Figure 2a shows the time-domain optical response of the bismuth single crystal at helium temperature that is observed when coherent phonons are excited in the collapse–revival mode [8]. The general shape of the
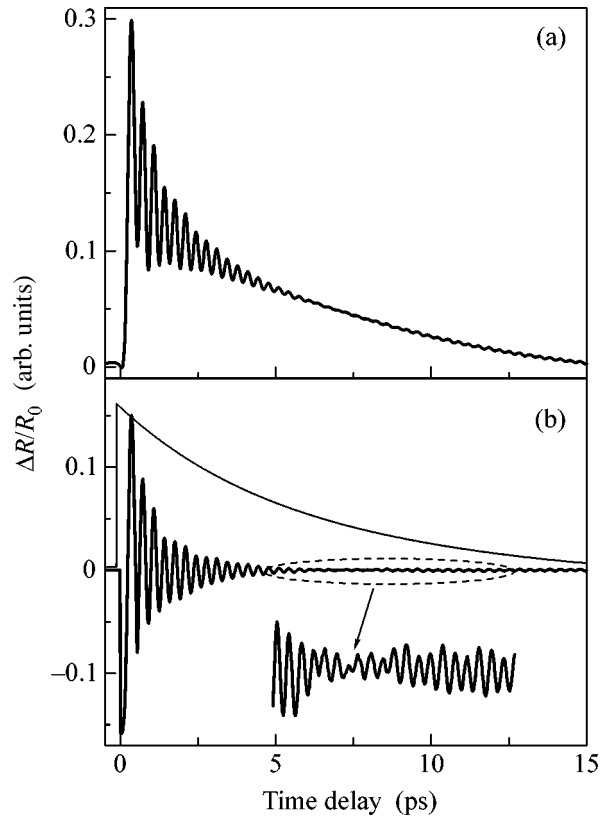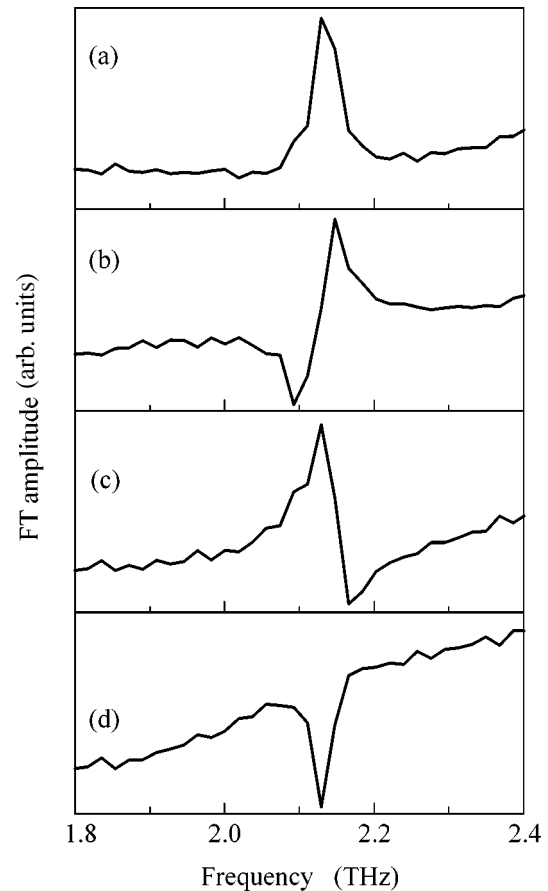


**Fig. 2.** (a) Time-domain normalized differential reflection $\Delta R/R_0$ of the bismuth single crystal for the experimental parameters $T = 7$ K and $F = 9$ mJ/cm$^2$. (b) The decomposition of the signal shown in panel (a) into oscillating and nonoscillating components. The inset shows the part of the signal exhibiting the collapse and revival of oscillations.

response shows that the pumped crystal relaxes to the equilibrium state for times on the order of ten picoseconds and fast oscillations are imposed on this relaxation, which demonstrate the collapse–revival effect in times $\tau \approx 7$–8 ps; see the inset in Fig. 2b. The decomposition of the signal into oscillating (lattice) and monotonically decreasing (electron) components (see Fig. 2b) with the subsequent Fourier analysis of the former component shows that oscillations in the collapse–revival mode are generated by totally symmetric ($A_{1g}$) and doubly degenerate ($E_g$) coherent phonons and their difference combination ($A_{1g} - E_g$). The spectrum shown in Fig. 3 exhibits two features the first of which is the two-component structure of the totally symmetric phonon with the long-lived component indicating the presence of quantum (Fröhlich) condensation [9]. The second feature of the spectrum is the strongly asymmetric lineshape of the twice degenerate ($E_g$) coherent phonon, which is similar to the dispersion curve rather than to the Lorentzian profile. To reveal the causes of such a surprising spectral lineshape, we analyzed the dependence of the spectrum on the size and position of the time window used in the Fourier transform. Since
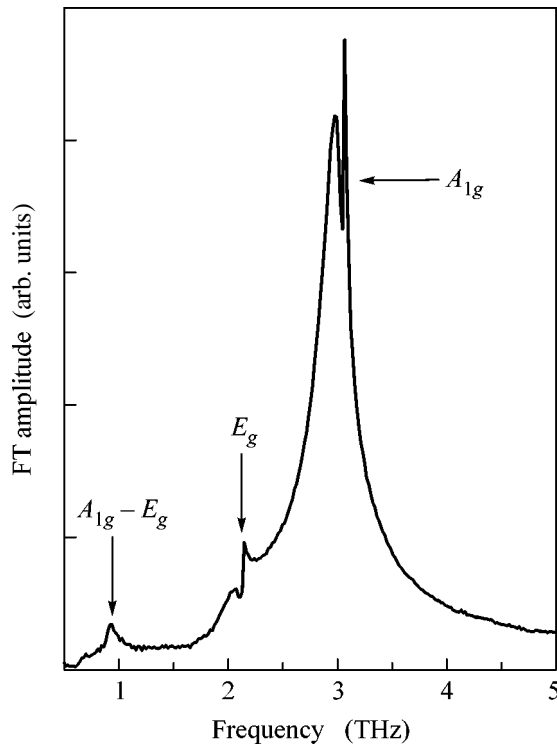
**Fig. 3.** Fourier spectrum of the oscillating component of the reflected signal.



**Fig. 4.** Spectrum of the $E_g$ phonon in the Bi single crystal when varying the initial position of the time window used for the Fourier transform. The initial position of the window varies within 1 ps for the total window width on the order of 25 ps.

the basic contribution to the Fourier transform comes from large-amplitude oscillations near the lower limit of the time window, a change in this limit provides a dependence similar to the time dependence of the spectrum. The performed analysis shows that the spectral lineshape depends significantly on the lower limit of the time window for all three components $A_{1g}$, $E_g$, and $A_{1g} - E_g$ observed in the spectrum. In this work, we focus only on the $E_g$ phonon, leaving detailed description of the totally symmetric and difference modes for future investigations. Figure 4 shows the dependence of the lineshape of the $E_g$ phonon on the lower limit of the time window. According to this figure, the shift of the time window significantly changes the lineshape of the $E_g$ phonon from the pure Lorentzian peak to the symmetric spectral dip, between which asymmetric profiles appear with dips on low-frequency and high-frequency wings of the line. Such a change in the lineshape of the $E_g$ phonon is periodic in time and is repeated with a period approximately equal to the period of the difference phonon mode ($A_{1g} - E_g$). When the time window is shifted beyond the limits of the collapse time, the phonon line remains asymmetric with a steeper high-frequency wing, but the oscillating character of asymmetry disappears. Approximation of the line by Eq. (1) indicates that the asymmetry parameter is positive for the spectra presented in Figs. 4a and 4c, whereas it is negative for the spectra shown in Figs. 4b and 4d. We note that, without any mathematical fitting, this conclu-

sion follows directly from the antiresonance position determined by the condition $q = -\varepsilon$. The alternating and oscillating behavior of the Fano parameter definitely indicates that $q$ is a complex number due to the time dependence of the zero and pole of the scattering amplitudes.

Controlled change in the spectral lineshape that includes the effect of the transfer of the antiresonance dip is well known and widely used in the active polarization nonlinear spectroscopy [10]. Although the physics of the effect, which is reduced to the interference of the electron continuum and discrete (phonon) level, is similar in the frequency and time domains, there are significant differences. In active spectroscopy, change in the spectral position of the antiresonance is achieved by varying the orientation of the polarization analyzer in the detection channel and, correspondingly, by choosing the coupling components of the tensors responsible for the discrete level and continuum. In this case, the sign of the asymmetry parameter is determined by the relation between the signs of the tensor components. In other words, the sign of $q$ is determined

by the symmetry properties as in [3, 4]. In our experiments, the detection conditions remain unchanged and the change of the sign of the Fano parameter is determined only by the dynamics of the system under investigation, which is the first observation of this kind.

First of all, we consider how the change of the sign of the asymmetry parameter is formally possible. The pumping–probing method is a time-domain analogue of the coherent anti-Stokes/Stokes stimulated Raman scattering, which is one kind of active nonlinear spectroscopy. In this case, the generation of coherent excitations is determined by the square of the nonlinear susceptibility of the crystal that is induced by an intense pumping pulse. In contrast to spontaneous Raman scattering, where the Stokes and anti-Stokes channels are independent of each other, which follows from time reversal symmetry and is responsible for the detailed balance principle, in our experiment, these channels correlate with each other and anti-Stokes scattering occurs even at absolute zero temperature, breaking the detailed-balance principle. Moreover, spontaneous scattering occurs through one intermediate (virtual) level, whereas stimulated scattering involves two intermediate levels [10]. Therefore, stimulated scattering may exhibit resonance between a phonon and the electron continuum, which is determined by the difference of the intermediate levels (wave mixing responsible for the process is possible even in the absence of the mixed phonon resonance [10]). Thus, ultrashort light pulses excite both lattice and electron states. For this reason, the pumping of the crystal is of the mixed character and the nonstationary coherent effect arises because the crystal holds a certain phase between the electron and lattice excitations for certain time. This behavior can be schematically illustrated by the simplified diagram shown in Fig. 5. According to this diagram, the sign of the Fano parameter can be changed by either changing the properties of the electron continuum or modifying the properties of the lattice mode. In other words, the change $\chi(\Omega) \longrightarrow \chi(-\Omega) \equiv -\chi(\Omega)$ for the discrete level or continuum may ensure the desired the change of the sign of the asymmetry parameter.

In experiments [3], the change of the sign of the asymmetry parameter is treated as the complexity of $q$ and is attributed to the breaking of time reversal symmetry. In this case, following the formalism developed for Raman scattering [11], we may represent Eq. (1) in the form

$$I(\varepsilon) = \frac{|\varepsilon + q|^2}{1 + \varepsilon^2} = \frac{[(\varepsilon + \mathrm{Re}q)^2 + (\mathrm{Im}q)^2]}{1 + \varepsilon^2}$$

$$= 1 + \frac{[(\mathrm{Re}q)^2 + (\mathrm{Im}q)^2]}{1 + \varepsilon^2} + \frac{2\varepsilon\mathrm{Re}q - 1}{1 + \varepsilon^2}. \quad (2)$$

Here, the second term describes the discrete-excitation part that does not undergo interference (imaginary part of susceptibility) and the last, interference, term is determined by the real parts of the susceptibility of the
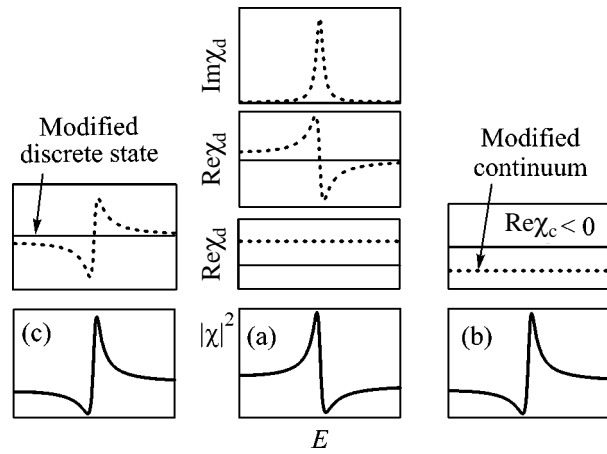


**Fig. 5.** (a) Schematic representation of the interference between the mixing active discrete state, which is described by the real and imaginary parts of susceptibility $\chi_d$, and the continuum presented by the real part of susceptibility $\chi_c$ and the results of the changes (b) $\chi_d(\Omega) \longrightarrow \chi_d(-\Omega)$ and (c) $\chi_c(\Omega) \longrightarrow \chi_c(-\Omega)$.

continuum and discrete level. Formula (2) describes the asymmetric and symmetric profiles for $\mathrm{Re}q \gg \mathrm{Im}q$ and $\mathrm{Re}q \ll \mathrm{Im}q$, respectively, and transfers the position of the antiresonance when the sign of the real part changes.

The connection of the change of the sign of the Fano parameter with the breaking of time reversal symmetry physically means that experimental conditions include external or internal axisymmetric fields (e.g., magnetic fields). In this case, the symmetry of the system is reduced from the type-II Shubnikov group to the type-I Shubnikov group, which is mathematically equivalent to the absence of the complex conjugation (spin reversal). It would be assumed that certain internal fields that are responsible for broken symmetry also arise in the case of Fröhlich condensate [9], but it is more natural to search for an interpretation of the experiment that would avoid such fundamental conclusions, and we try to show that this is possible.

The breaking of time-reversal symmetry can be microscopically caused by the presence of dissipation in the system and change in the type of carriers or process responsible for the detected signal. With sufficient confidence in our experiments, we can exclude dissipation as a cause of the alternating behavior of the Fano parameter, which is attributed to the periodic (oscillating) character of the observed phenomenon. Two other causes, replacement of an electron by a hole (the latter is an electron moving back in time) and change in the scattering channel (i.e., change of the phenomenon to "anti-phenomenon"), should be analyzed in more detail. Indeed, it is known from investigations of Raman scattering in semiconductors that a change in the type of carriers gives rise to the change in the sign of the asymmetry parameter of the phonon line [11].

The band structure of bismuth is characterized by the presence of electron and hole pockets at the boundary of the Brillouin zone [12]. For this reason, it can be assumed that, with a significant increase in the inter-atomic spacing that is caused by the large phonon amplitude, the lattice interacts primarily with one type of current carriers, whereas interaction in the presence of interatomic approaching occurs with another type of carriers. It is impossible to exclude the possibility of the dielectric transition induced by the large displacements of atoms involved in the formation of coherent phonons. In this case, the bottom of the conduction band in a semimetal moves upward and can leave the region of band overlapping. As a result, electrons sink to the valence band and the conduction band remains empty. We note that the replacement of an electron by a hole is equivalent to a change in the real part of the susceptibility of the continuum shown in Fig. 5b.

The second possible cause of the alternating (complex) behavior of the Fano parameter is a change in the scattering channel in dependence on the delay time. To explain this fact, we emphasize that the probing light pulse in our experiments interacts with the *coherent* medium prepared by the pumping pulse. Such a parametric interaction between waves of different origins constitutes phase-dependent Raman scattering [13], where the Stokes and anti-Stokes components of the probing pulse are enhanced (or damped) in dependence on the phase relations between excitations of matter and the electromagnetic field. Indeed, using the pumping–probing method supplemented by the spectral analysis of the probing pulse, it was found [13] that the spectrum of the probing pulse (as well as its integral intensity) is a function of the time delay; i.e., the Stokes and anti-Stokes components of the probing pulse are alternately enhanced and damped. The periodic variation in the absolute value and sign of the asymmetry parameter may be attributed to this alternation of the Stokes and anti-Stokes scattering channels (we remind that the Stokes process for spontaneous scattering is the time-reversed anti-Stokes process). Change in the scattering channel for the mixing active phonon level that occurs under the transformation $\mathrm{Re}\chi(\Omega) \longrightarrow \mathrm{Re}\chi(-\Omega) \equiv -\mathrm{Re}\chi(\Omega)$ is caused by the change of the sign of the susceptibility argument (we note that the imaginary part of the susceptibility is an even function of frequency and remains unchanged).

The mechanism of the appearance of the complex asymmetry parameter is as follows. Through nonstationary stimulated Raman scattering, the pumping pulse excites phonons and electrons in the frequency range limited by the spectral width of the laser pulse. The energies of optical phonons in bismuth overlap with electrons due to interband transitions [12], which can be responsible for the appearance of the electron continuum, and the large excitation density allows the interaction between $A_{1g}$ and $E_g$ phonons through the electron continuum. In this case, the interaction of *each* phonon with the continuum gives rise to change in the

phase properties of this continuum and, as a result, the asymmetry parameter of the $E_g$ phonon becomes a function of the difference between the phases of the phonon level and continuum. Oscillations in $q$ are evidently sensitive to the interaction of *both* phonons with the continuum and occur with the frequency of the difference phonon mode.

Thus, using the pumping–probing method with high-energy femtosecond pulses in bismuth crystals at helium temperature, we observe Fano interference with the alternating (complex) asymmetry parameter $q$. The complex character of the Fano parameter indicates that time-reversal symmetry is broken in the nonlinear collapse–revival mode for coherent phonons and is attributed to either change in the type of carriers with which the lattice interacts or the alternation of the dominant scattering channel (from Stokes to anti-Stokes) for various delay times. At the current stage of investigations, it is difficult to favor any mechanism, although we think that change in the scattering channels is a more realistic cause.

## REFERENCES

1. U. Fano, Phys. Rev. **124**, 1866 (1961).
2. A. R. P. Rau, Phys. Scr. **69**, C10 (2004).
3. K. Kobayashi, H. Aikawa, S. Katsumoto, and Y. Iye, Phys. Rev. Lett. **88**, 256 806 (2002).
4. J. Faist, F. Capasso, C. Sirtori, *et al.*, Nature **390**, 589 (1997).
5. T. Dekorsy, G. C. Cho, and H. Kurz, in *Light Scattering in Solids VIII*, Ed. by M. Cardona and G. Güntherodt (Springer, Berlin, 2000), p. 169.
6. O. V. Misochko, K. Kisoda, K. Sakai, and S. Nakashima, Phys. Rev. B **61**, 4305 (2000).
7. M. Hase, M. Kitajima, A. M. Constantinescu, and H. Petek, Nature **426**, 51 (2003).
8. O. V. Misochko, M. Hase, and M. Kitajima, Pis'ma Zh. Éksp. Teor. Fiz. **78**, 85 (2003) [JETP Lett. **78**, 75 (2003)].
9. O. V. Misochko, M. Hase, K. Ishioka, and M. Kitajima, Phys. Lett. A **321**, 381 (2004).
10. G. Fogg, in *Light Scattering in Solids II*, Ed. by M. Cardona and G. Güntherodt (Springer, Berlin, 1975; Mir, Moscow, 1984), p. 275.
11. G. Abstreiter, M. Cardona, and A. Pinczuk, in *Light Scattering in Solid IV*, Ed. by M. Cardona and G. Güntherodt (Springer, Berlin, 1984; Mir, Moscow, 1986), p. 5.
12. M. S. Dresselhaus, *The Physics of Semimetals and Narrow-Gap Semiconductors*, Ed. by D. L. Carter and R. T. Bate (Pergamon, Oxford, 1973), p. 3.
13. O. V. Misochko, M. Hase, and M. Kitajima, J. Phys.: Condens. Matter **16**, 1879 (2004).

*Translated by R. Tyapaev*

# Quantum Interference in Mössbauer Scattering Spectra

## É. K. Sadykov*, V. V. Arinin, and F. G. Vagizov

*Kazan State University, Kazan, 420008 Russia*
*\*e-mail: esad@ksu.ru*
Received June 7, 2005; in final form, August 8, 2005

The role of quantum interference in the formation of the resonance scattering spectra of Mössbauer photons is studied. A resonant rf field mixing the spin levels of the excited state of a nucleus is considered to be the mechanism ensuring the conditions for quantum interference. A considerable intensity redistribution of the elastic and Raman scattering channels is shown to occur as a result of quantum interference. © *2005 Pleiades Publishing, Inc.*

PACS numbers: 61.18.Fs

In recent years, attempts have been made to realize quantum interference effects for gamma radiation amplitudes by using Mössbauer transitions [1]. These are the effects that have been observed previously in the optical region [2]: the electromagnetically induced transparency of a medium, the slow-down of the group velocity of light, the inversionless amplification and generation of radiation, and so on. Although as early as in the 1960s it was hoped that the Mössbauer effect might be used to solve some problems of gamma optics (in particular, the problem of gamma laser creation) [3], the notion of the quantum interference of Mössbauer photons was introduced much more recently [4], and it remains most important up to now. In this work, we studied the consequences of quantum interference in spectra of resonant Mössbauer scattering when the spin of the excited nuclear state is governed by coherent dynamics caused by a resonant rf field. As we will show below, due to the quantum interference, the Raman scattering prevails in this case.

Consider first a three-level model (Fig. 1a). Level 1 represents the ground state of a nucleus and levels 2 and 3 are the spin sublevels of its excited state. The rf driving field with a frequency $\omega_0$ is tuned to exact resonance with the transition 2–3 ($\omega_0 = \omega_{32} = \varepsilon_3 - \varepsilon_2$). The radiation of the Mössbauer source is tuned (possibly, with some detuning) to the transition 1–2. The Hamiltonian of this system has the form

$$\hat{H} = \hat{H}_0 + \hat{H}_{\rm rf}^0 + \hat{H}_\gamma^0 + \hat{H}_{\rm rf} + \hat{H}_\gamma(k). \tag{1}$$

Here, the term $\hat{H}_0$ represents the nuclear and hyperfine interactions; $\hat{H}_{\rm rf}^0$ and $\hat{H}_\gamma^0$ are responsible for the free rf and gamma fields, respectively; and $\hat{H}_{\rm rf}$ and $\hat{H}_\gamma$ describe the interactions of the nucleus with the rf field and Mössbauer radiation, respectively.

The terms of Hamiltonian (1) are expressed as

$$\hat{H}_0 = \sum_{j=1,2,3} \varepsilon_j a_j^+ a_j, \quad \varepsilon_1 = 0; \quad \hat{H}_{\rm rf}^0 = \omega_0 \hat{b}^+ \hat{b};$$

$$\hat{H}_\gamma^0 = \sum_k \omega_k \hat{c}_k^+ \hat{c}_k, \tag{2}$$

$$\hat{H}_{\rm rf} = \Omega_0 \hat{b} \hat{a}_3^+ \hat{a}_2 + \Omega_0^* \hat{b}^+ \hat{a}_2^+ \hat{a}_3, \tag{3}$$

$$\hat{H}_\gamma(k) = A_k \hat{c}_k \hat{a}_2^+ \hat{a}_1 + A_k^* \hat{c}_k^+ \hat{a}_1^+ \hat{a}_2, \quad \omega_k = c_0 k. \tag{4}$$

Here, $\hat{a}_j^+$, $\hat{a}_j$, and $\varepsilon_j$ are the Fermi operators of the creation and annihilation and the energy of the $j$th state of $H_0$, respectively (Fig. 1a); $\hat{b}^+$ and $\hat{b}$ are the Bose operators of creation and annihilation of an rf photon, respectively; $\hat{c}_k^+$ and $\hat{c}_k$ are the corresponding operators for a $\gamma$-ray photon with the wave vector $k$; $\Omega_0$ and $A_k$ are the coupling constants of rf and $\gamma$-ray photons with the nucleus, respectively; $c_0$ is the speed of light; and $\hbar = 1$ is assumed.

We will consider preliminarily a pair of spin levels coupled by a strong rf field,

$$\sum_{i=2,3} \varepsilon_i \hat{a}_i^+ \hat{a}_i + \omega_0 \hat{b}^+ \hat{b} + \Omega_0 \hat{a}_3^+ \hat{a}_2 \hat{b} + \Omega_0^* \hat{a}_2^+ \hat{a}_3 \hat{b}^+. \tag{5}$$

The eigenstates $e_q^n(t)$ ($q = 1, 2$) of this Hamiltonian are known as dressed states [5]. For the exact resonance ($\omega_0 = \varepsilon_3 - \varepsilon_2$), the explicit expressions for $e_q^n(t)$ in terms of the basis states $\hat{H}_0$ and $\hat{H}_{\rm rf}^0$ are given by

$$e_1^n(t) = e^{-iE_1^n t - in\omega_0 t} \frac{1}{\sqrt{2}}(-|2, n\rangle + e^{i\varphi}|3, n-1\rangle), \tag{6}$$
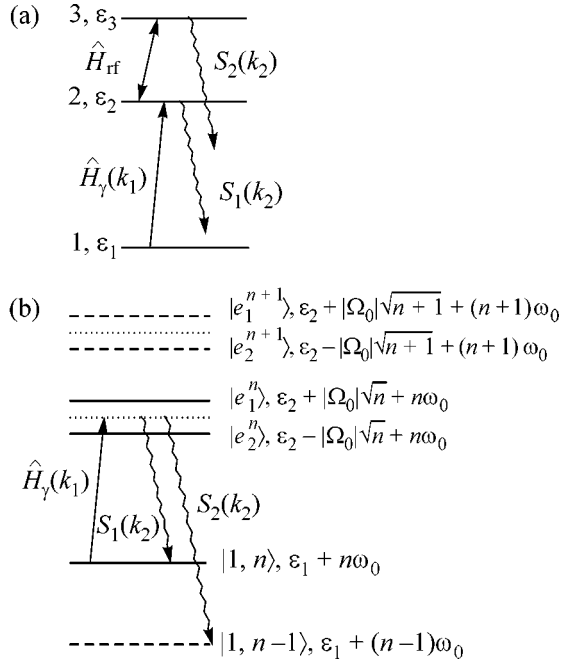
**Fig. 1.** (a) A three-level model scheme of the scattering of Mössbauer quanta and (b) an equivalent scheme of scattering by dressed states.

$$e_2^n(t) = e^{-iE_2^n t - in\omega_0 t} \frac{1}{\sqrt{2}}(e^{-i\varphi}|2, n\rangle + |3, n-1\rangle), \quad (7)$$

where $|j, n\rangle \equiv |j\rangle|n\rangle$, $|n\rangle$ is the $n$ photon state of the rf field, and $\varphi$ is defined by the expression $\Omega_0 = |\Omega_0|\exp(i\varphi)$.

States (6) and (7) can also be classified as quasi-energy states [6] (steady states [7]); i.e., their time dependence is defined as follows:

$$e_q^n(t) = \exp(-iE_q^n t)\chi_q^n(t), \quad \chi_q^n(t+T) = \chi_q^n(t), \quad (8)$$

where $T = 2\pi/\omega_0$ is the period of the rf field, $E_{1,2}^n = \mp|\Omega_0|\sqrt{n} + \varepsilon_2$ is the quasienergy, and $|\Omega_0|\sqrt{n}$ is the Rabi frequency. In the second-quantization representation, the classical rf field is described by the coherent state [8]

$$|\alpha| = \exp(-|\alpha|^2/2) \sum_{n=0}^{\infty} \frac{\alpha^n}{\sqrt{n!}}|n\rangle,$$

where

$$|\alpha|^2 = \bar{n} = \sum_{n=1}^{\infty} nP(n)$$

is large. In this case, the Poisson distribution $P(n)$ describing the population of the Fock states $|n\rangle$ has a sharp maximum at $n \approx \bar{n}$. Therefore, the effect of the

classical rf field on the spin states can be described with good accuracy by functions (6) and (7) at $n \approx \bar{n}$.

The resonance scattering of $\gamma$-ray photons will be described using the scattering amplitude in the dressed-state representation in the second order of the perturbation theory with respect to the interaction $\hat{H}(k)$. The use of dressed states allows one to take into account exactly the effect of the rf field,

$$A_{i,f} \sim \sum_q \int_0^{\infty} dt \exp(-\Gamma t/2)\langle f(t)|\hat{H}_\gamma(\mathbf{k}_2)|e_q^n(t)\rangle \qquad (9)$$

$$\times \langle e_q^n(0)|\hat{H}_\gamma(\mathbf{k}_1)|i(0)\rangle.$$

Here, $\Gamma$ is the natural width of the Mössbauer level; $|i(0)\rangle = |i(t = 0)\rangle = |1\rangle|n\rangle|k_1\rangle$ and $|f(t)\rangle = \exp(-iE_f t)|1\rangle|n'\rangle|k_2\rangle$ are the initial and final states of the system, whose total energies are $E_i = \varepsilon_1 + n\omega_0 + E_{k1}$ and $E_f = \varepsilon_1 + n'\omega_0 + E_{k2}$, respectively; and $k_1$ and $k_2$ are the wave vectors of the incident and scattered photons.

The probability of the scattering of Mössbauer radiation is calculated by the formula [9]

$$S_{i,f} \sim \int dE_{k_1}|A_{i,f}|^2\delta(E_f - E_i)f_L(E_{k_1} - E_{k_0}). \quad (10)$$

Here, the energy conservation law is taken into account and averaging over the energies $E_{k1}$ of the incident photons is performed with regard to the function describing the source line shape (commonly, the Lorentz function) $f_L(E_{k1} - E_{k0})$, where $E_{k0}$ is the energy corresponding to the maximum of this function. In what follows, the half-width of $f_L(E_{k1} - E_{k0})$ is assumed to be equal to $\Gamma/2$.

Figure 1b shows the scheme of the scattering of $\gamma$-ray photons in the dressed-state representation at $E_{k0} = \varepsilon_2$. We will consider transitions (9) with $n' = n$ and $n' = n - 1$, corresponding to the elastic scattering ($S_1$) and to the Raman scattering ($S_2$). The amplitudes of these two transitions have the form

$$A_{1nk_2, 1nk_1} \sim \sum_q \int_0^{\infty} dt\langle 1, n, k_2|\hat{H}(\mathbf{k}_2)|e_q^n(t)\rangle \qquad (11)$$

$$\times \langle e_q^n(0)|\hat{H}(\mathbf{k}_1)|1, n, k_1\rangle e^{iE_{k2}t + in\omega_0 t - \Gamma t/2},$$

$$A_{1nk_1, 1(n-1)k_2}$$

$$\sim \sum_q \int_0^{\infty} dt\langle 1, n-1, k_2|\hat{H}(\mathbf{k}_2)|e_q^n(t)\rangle \qquad (12)$$

$$\times \langle e_q^n(0)|\hat{H}(\mathbf{k}_1)|1, n, k_1\rangle e^{-\Gamma t/2 + iE_{k2}t + i(n-1)\omega_0 t}.$$

Substituting amplitudes (11) and (12) into Eq. (10) and integrating over the energy of the incident photons,

we obtain the spectral profiles of the elastic and Raman scattering for $E_{k0} = \varepsilon_2$,

$$S_1(k_2) = S_{k_1n,\,k_2n} \sim \left| \frac{1}{ip - \Omega_r} + \frac{1}{ip + \Omega_r} \right|^2 \tag{13}$$

$$\times f_L(E_{k2} - \varepsilon_2) \left| \langle 1 | \hat{H}(k_2) | 2 \rangle \langle 2 | \hat{H}(k_1) | 1 \rangle \right|^2,$$

$$S_2(k_2) = S_{k_1n,\,k_2n-1}$$

$$\sim \left| \frac{1}{ip - \Omega_r - \omega_0} - \frac{1}{ip + \Omega_r - \omega_0} \right|^2 \tag{14}$$

$$\times f_L(E_{k2} - \varepsilon_2 - \omega_0) \left| \langle 1 | \hat{H}(k_2) | 3 \rangle \langle 2 | \hat{H}(k_1) | 1 \rangle \right|^2,$$

where $p = -i(E_{k2} - \varepsilon_2) + \Gamma/2$, $\Omega_r = |\Omega_0| \sqrt{n}$ is the Rabi frequency of the rf field. In the case of the rf resonance ($\omega_0 = \varepsilon_3 - \varepsilon_2$), the proportionality coefficient in Eqs. (13) and (14) is the same.

It is easy to verify that, at small $\Omega_r$, Eqs. (13) and (14) exhibit constructive and destructive interference, respectively. In particular, at $\Omega_r$ tending to zero, $S_2$ also approaches zero. However, as $\Omega_r$ increases (more exactly, at $\Omega_r > \Gamma/2$), the character of the interference effects in Eqs. (13) and (14) reverses under the same conditions ($E_{k0} = \varepsilon_2$). Now, at sufficiently large $\Omega_r$, the intensity of the Raman line may become greater than the intensity of the elastic scattering line. In Fig. 2, the expected spectrum $S_1(k_2) + S_2(k_2)$ is shown, which was calculated for $\Omega_r = 1.5$ under the assumption that the matrix elements of the transitions 1–2 and 1–3 are equal to each other. The intensity ratio of the lines $S_2$ and $S_1$ is defined as $I_2/I_1$, where $I_2$ and $I_1$ are the areas under the curves $S_2$ and $S_1$, respectively. In Fig. 3, the ratio $I_2/I_1$ is shown as a function of $\Omega_r$. The fact that $I_2/I_1$ exceeds unity means that the nucleus absorbing a primary γ-ray photon in the transition 1–2 relaxes preferably from level 3, i.e., via the Raman rather than elastic channel. Such a preference in the way of nuclear relaxation we call the "valve" effect (intuitively, it seems that the ratio $I_2/I_1$ should asymptotically approach unity with increasing $\Omega_r$). This effect is explained by the fact that, at sufficiently large values of $\Omega_r$, the intensity of the elastic scattering decreases due to the destructive interference of the amplitudes, whereas the Raman scattering intensity increases due to their constructive interference. Both interferences are maximal precisely at $E_{k0} = \varepsilon_2$, at which the interfering amplitudes in Eqs. (13) and (14) are comparable in value. If the condition $E_{k0} = \varepsilon_2$ is violated (detuned), the magnitude of the valve effect decreases; as a result, the dependence of the ratio $I_2/I_1$ on the energy of the Mössbauer radiation $E_{k0}$ is resonant (Fig. 4).

As is seen in Fig. 3, the magnitude of the valve effect varies monotonically with $\Omega_r/\Gamma$. However, as the ratio $\Omega_r/\Gamma$ increases, the total intensity of scattering ($I_1 + I_2$) decreases rather rapidly (Fig. 5), which should be taken
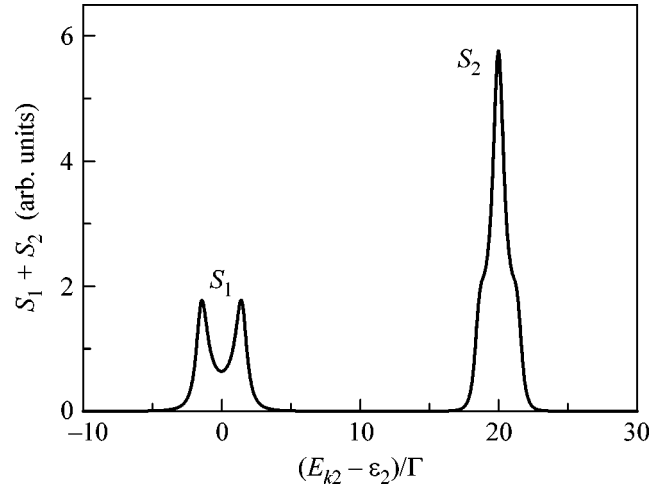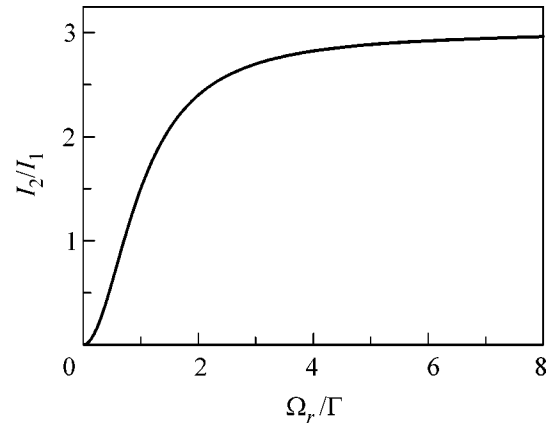
**Fig. 2.**



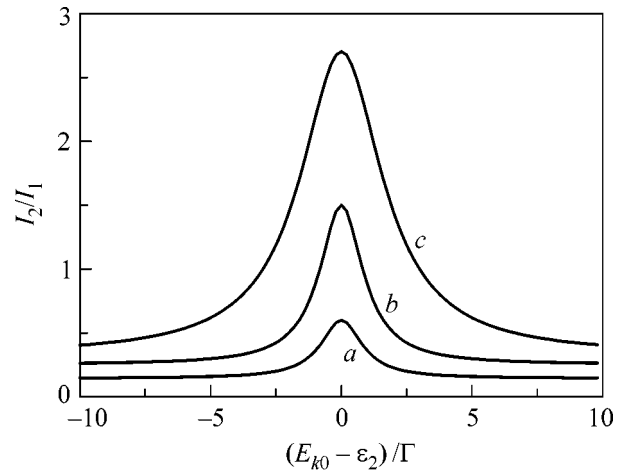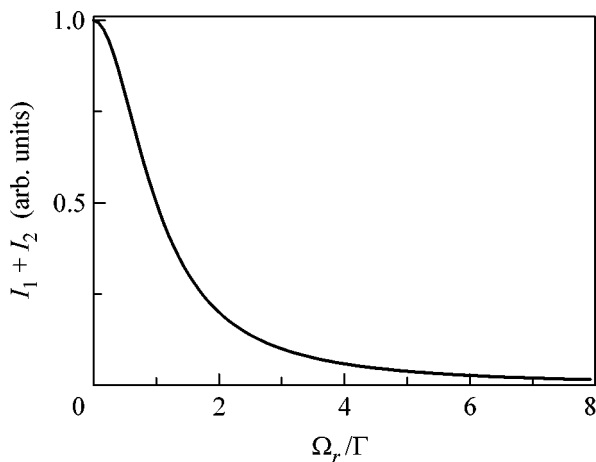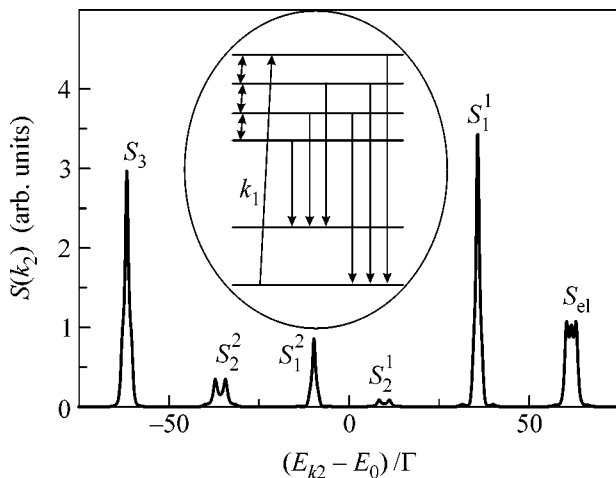**Fig. 3.** Dependence of the ratio $I_2/I_1$ on the Rabi frequency $\Omega_r$ at $E_{k0} = \varepsilon_2$.



**Fig. 4.** Dependence of the ratio $I_2/I_1$ on the photon energy $E_{k0}$ of the Mössbauer source for $\Omega_r =$ (a) 0.5, (b) 1, and (c) 3.

**Fig. 5.** Dependence of the total intensity of the scattered radiation $I_1 + I_2$ on the Rabi frequency $\Omega_r$ of the rf field at $E_{k0} = \varepsilon_2$.



**Fig. 6.** Expected resonance scattering spectrum for the $Fe^{57}$ isotope under the rf resonance conditions of the excited state of the nucleus. The Rabi frequency $\Omega_r = 1.5$ (see the text), and $E_0$ is the energy of the Mössbauer level. The pumping line is tuned to the sixth component of the Zeeman multiplet; $S_{el}$ is the line of the elastic scattering; and ($S_1^1$, $S_1^2$), ($S_2^1$, $S_2^2$), and $S_3$ are the Raman lines of the first, second, and third orders, respectively.

into account primarily in the experimental realization of this effect. Therefore, the optimal condition for the observation of the effect is reduced to the relation $\Omega_r \sim \Gamma$. This is the condition for a single photon to excite two in-phase dressed states, whose interference underlies the effect under discussion.

The abstract three-level system considered above is well suited for the understanding of the essence of the

valve effect. However, the number of levels in real isotopes is greater than three. In addition, it is necessary to take into account that the hyperfine components of Mössbauer transitions have different intensities and angular dependences of radiation. However, the valve effect will still be observed if the sublevels of the excited state of a nucleus are coupled with a driving field. As before, at a sufficiently large $\Omega_r/\Gamma$ value, the intensity of the elastic scattering decreases due to destructive interference. The intensity of a Raman line increases and decreases if the line is formed by an odd and even number of rf photons, respectively. However, the ratio of the line intensities should be compared now not with unity as a limiting value, but with the ratio of the squares of the corresponding transition matrix elements calculated for a particular scattering angle. The results of our calculations of the expected effect for the $Fe^{57}$ isotope are presented in Fig. 6.

In conclusion, we discuss how the effect considered in this study is related to the rf effects in Mössbauer spectroscopy described previously [10, 11]. The first works in this field were aimed at studying the quasienergy structure of Mössbauer spectra, which was described first in [10]. The expected structure in absorption spectra was observed in [12, 13]. Those experiments are directly related to the quantum interference effect discussed here. They showed the possibility of the coherent dynamics of nuclear spins of $Fe^{57}$ in magnetic materials under magnetization reversal. This is the main condition for the realization of the quantum interference effect under discussion. In addition, it was shown in [12, 13] that the Rabi frequency values necessary for the observation of the valve effect can be reached in the case of $Fe^{57}$ isotopes in magnetically ordered systems. Using the experimental spectra reported in [12], the amplitude of an oscillating hyperfine field induced at a nucleus is easily estimated as $h_1 \approx 88$ kOe, which corresponds to the Rabi frequency $\Omega_r \approx 1.5$ used in the calculation of the spectrum shown in Fig. 6.

We note that, for this (rf) mechanism of quantum interference, the manifestation of quantum interference effects should not be expected in absorption spectra (at least in the thin-absorber approximation). Indeed, according to the optical theorem, the absorption cross section can be represented as the imaginary part of the forward scattering amplitude. Then, the spectrum depends linearly (rather than quadratically) on the scattering amplitude, and the split amplitudes do not interfere. For this reason, the quantum interference effect could not be observed in [10, 11]. The early theories of the resonance scattering of Mössbauer radiation under the conditions of rf dynamics of nuclear spins [9, 14, 15] did not focus on quantum interference.

03), and by the NIOKR RT [project no. 06-6.1-2003/2005(F)].

## REFERENCES

1. O. Kocharovskaya, R. Kolesov, and Yu. Rostovtsev, Phys. Rev. Lett. **82**, 3593 (1999); E. K. Sadykov, L. L. Zakirov, and A. A. Yurichuk, Laser Phys. **11**, 409 (2001); R. Coussement, Y. Rostovtsev, J. Odeurs, *et al.*, Phys. Rev. Lett. **89**, 107601 (2002).

2. M. O. Scully and M. S. Zubairy, *Quantum Optics* (Cambridge Univ. Press, Cambridge, 1997; Fizmatlit, Moscow, 2003).

3. L. A. Rivlin, Vopr. Radioélektron. **6**, 43 (1963).

4. R. Coussement, M. Van den Bergh, G. S'heeren, *et al.*, Phys. Rev. Lett. **71**, 1824 (1993).

5. L. M. Narducci, M. O. Scully, G.-L. Oppo, *et al.*, Phys. Rev. A **42**, 1630 (1990); A. S. Manka, H. M. Doss, L. M. Narducci, *et al.*, Phys. Rev. A **43**, 3748 (1991).

6. H. Sambe, Phys. Rev. A **7**, 2203 (1973).

7. Jon H. Shirley, Phys. Rev. **138**, B979 (1965).

8. J. Perina, *Coherence of Light* (Van Nostrand Reinhold, New York, 1972; Mir, Moscow, 1974).

9. Sh. Sh. Bashkirov, A. L. Beljanin, and E. K. Sadykov, Phys. Status Solidi B **93**, 437 (1979).

10. M. N. Hack and M. Hammermesh, Nuovo Cimento **19**, 546 (1961).

11. H. Gabriel, Phys. Rev. **184**, 359 (1969).

12. F. G. Vagizov, Hyperfine Interact. **61**, 1359 (1990).

13. I. Tittonen, M. Lippmaa, E. Ikonen, *et al.*, Phys. Rev. Lett. **69**, 2815 (1992).

14. A. M. Afanas'ev, P. A. Aleksandrov, and S. S. Yakimov, Preprint No. 3337/9, IAÉ (Inst. of Atomic Energy, Moscow, 1980), p. 24.

15. A. V. Mitin, Phys. Lett. A **84**, 283 (1981).

*Translated by V. Rogovoǐ*

# Local Magnon Modes and the Dynamics of a Small-Radius Two-Dimensional Magnetic Soliton in an Easy-Axis Ferromagnet

## B. A. Ivanov[a] and D. D. Sheka[b]

*a Institute of Magnetism, Kiev, 04071 Ukraine*
*b Taras Shevchenko National University, Kiev, 01033 Ukraine*
*e-mail: denis_sheka@univ.kiev.ua*
Received May 23, 2005; in final form, August 10, 2005

The internal dynamics of a small-radius precession magnetic soliton is considered. A variational formulation of the problem on the soliton–magnon interaction is proposed and used to calculate the frequency of a truly local mode. It is shown that this mode, as well as the conventional translational mode, remains localized in the small soliton radius limit. The presence of the local mode is confirmed by the numerical solution of the scattering problem. © *2005 Pleiades Publishing, Inc.*

PACS numbers: 05.45.–a, 75.10.Hk, 75.30.Ds

It is well known that topological solitons play an important role in the physics of two-dimensional (2D) magnetism [1]. Solitons have a profound impact on the thermodynamics and response functions of a magnet. The interest in 2D topological magnetic solitons had mainly been initiated by Belavin and Polyakov [2], who constructed a static solution with finite energy for a purely isotropic ferromagnet and showed that, in such a magnet, a thermal excitation of solitons destroys the long-range order. The inclusion of a magnetic anisotropy, which is always present in actual magnets, violates the scale invariance of the problem and gives rise to the characteristic magnetic length $l_0 = \sqrt{A/K}$, where $A$ is the inhomogeneous exchange constant and $K$ is the anisotropy constant. In an anisotropic ferromagnet, static non-one-dimensional solitons with finite energy are unstable with respect to collapse [3]. However, in easy-axis ferromagnets, the conservation of the total $z$ projection of magnetization

$$N = \frac{S}{a^2}\int d^2x(1 - \cos\theta)$$

leads to the presence of stable dynamic solitons with a precession of the magnetization vector with frequency $\Omega$ about the easy axis of the ferromagnet [4, 5]. In terms of angular variables for the normalized magnetization $\mathbf{m} = \mathbf{S}/S = (\sin\theta\cos\phi; \sin\theta\sin\phi; \cos\theta)$, the structure of such a precession topological soliton is described by the formulas [5]

$$\theta_0 = \theta_0(r), \quad \phi_0 = \phi_0 + q\chi - \Omega t, \tag{1}$$

where $r$ and $\chi$ are the polar coordinates in the magnet plane, $\phi_0$ is an arbitrary angle, and the integer number $q$

determines the $\pi_2$ topological charge of the soliton (below, we assume that $q = 1$). The structure of a stationary soliton is determined by the solution to the differential problem

$$\frac{d^2\theta_0}{dr^2} + \frac{1}{r}\frac{d\theta_0}{dr} - \sin\theta_0\cos\theta_0\left(\frac{1}{l_0^2} + \frac{1}{r^2}\right) + \frac{\Omega}{\omega_0}\sin\theta_0 = 0,$$
$$\theta_0(0) = \pi, \quad \theta_0(\infty) = 0. \tag{2}$$

Here, $\omega_0 = \gamma H_a$ is the gap in the spectrum of linear magnons characterized by the dispersion law $\omega(\mathbf{k}) = \omega_0(1 + l_0^2\mathbf{k}^2)$, $\gamma$ is the gyromagnetic ratio, $H_a$ is the anisotropy field, and $l_0$ is the magnetic length introduced above. In the isotropic case ($l_0 \longrightarrow \infty$), this equation determines the static ($\Omega = 0$) Belavin–Polyakov solution $\tan\theta_0/2 = R/r$, where the arbitrary parameter $R$ has the meaning of the soliton radius. A solution to problem (2) can easily be constructed by the numerical method. Approximately, this solution is described by the simple function [6]

$$\tan\frac{\theta_0}{2} = \frac{R}{r}\exp\left(-\frac{r - R}{r_0}\right), \quad r_0 = l_0\sqrt{\frac{\omega_0}{\omega_0 - \Omega}}, \tag{3}$$

which actually determines the Belavin–Polyakov solution with the cutoff radius $r_0$. For an anisotropic ferromagnet, the energy of the soliton, its precession frequency $\Omega$, and its characteristic radius are determined by the number $N \simeq S(R/a)^2$. Since the magnetic length is $l_0 \gg a$, where $a$ is the lattice constant, the macroscopic approximation and the semiclassical description

$N \gg 1$ are also applicable to solitons with small radii $R \ll l_0$, which are discussed in this paper.

The properties of 2D precession solitons are well understood [1]. However, the laws governing the translational dynamics of solitons, i.e., the motion of a soliton as a whole, remain poorly investigated. The same problem exists for other 2D nonlinear states with nontrivial topology, such as, for example, magnetic vortices. The use of a combination of direct numerical modeling with analytical methods showed that the dynamics of vortices is non-Newtonian: the coordinate of the center of a vortex $\mathbf{X}(t)$ satisfies an equation that contains higher-than-second derivatives of $\mathbf{X}$ with respect to $t$ [7] and coefficients depending on the size and shape of the ferromagnet sample in which the vortex moves. For localized solitons (1), the possibility of describing their dynamics on the basis of Newtonian equations with a finite effective mass is open to question. For example, in [8], it is stated that only the inertialess dynamics of a localized soliton "frozen into" the external spin flux is possible.

At first glance, the problem can easily be solved on the basis of the adiabatic perturbation theory for solitons [9]. This theory was used to describe the dynamics of one-dimensional solitons under the effect of arbitrary perturbations slowly varying in space and time. However, the applicability of this approach to 2D topological solitons is limited by the fact that, because of the nontrivial topology of magnetization distribution in the soliton, the dynamics of the soliton as an object possesses gyroscopic properties with the gyroscopic constant $G = 4\pi q\hbar S/a^2$ [1]. Therefore, one can expect that the simplest effective equation of motion written for the coordinate $\mathbf{X}$ of the soliton center and taking into account the inertial terms has the form

$$m_* \frac{d^2\mathbf{X}}{dt^2} = \mathbf{F}_g + \mathbf{F}_{ext}, \quad \mathbf{F}_g = G\left[\mathbf{e}_z \times \frac{d\mathbf{X}}{dt}\right], \quad (4)$$

where $m_*$ is the effective mass of the soliton and $\mathbf{F}_{ext}$ is the external force acting on the soliton (e.g., from the boundary). Even for a free soliton ($\mathbf{F}_{ext} = 0$), this equation involves a "rapid" motion with the frequency $\omega_L = G/m_*$ (an analogue of the Larmor precession of a charged particle in magnetic field); hence, the condition of the slowness of the magnetization variation is not satisfied and the adiabatic perturbation theory [9] is inapplicable.

In this paper, we analyze the soliton dynamics by using a different approach: it was used in studying magnetic vortices and was based on considering the soliton–magnon scattering [10]. Its main idea is as follows: one considers the full set of magnon eigenmodes in the presence of a soliton, selects the eigenmodes that may be associated with the displacement of the soliton as a whole, and then compares the frequencies of these modes with the eigenmodes of Eq. (4). Thus, we verify the Newtonian equation and calculate the effective soli-

ton mass $m_*$, which remains finite for any soliton radius but increases as the soliton radius $R$ decreases.

To study the interaction of magnons with a soliton, we use the Landau–Lifshitz equations

$$l_0^2 \nabla^2 \theta - \sin\theta\cos\theta[1 + l_0^2(\nabla\phi)^2] = \frac{\sin\theta}{\omega_0}\frac{\partial\phi}{\partial t},$$

$$l_0^2 \nabla \cdot (\sin^2\theta\nabla\phi) = -\frac{\sin\theta}{\omega_0}\frac{\partial\theta}{\partial t}. \quad (5)$$

For analyzing the soliton–magnon interaction, we consider small oscillations of magnetization $(\theta, \phi)$ on the background of a stationary soliton $(\theta_0, \phi_0)$. These oscillations can be described by the complex "wave function" $\psi = \theta - \theta_0 + i\sin\theta_0(\phi - \phi_0)$. Linearized equations for $\psi$ have the form of the so-called generalized Schrödinger equation [6, 11]

$$\frac{i}{\omega_0 l_0^2}\partial_t\psi = H\psi + W\psi^*, \quad H = (-i\nabla - \mathbf{A})^2 + U. \quad (6)$$

The specific feature of this equation is the presence of the term involving $W$, which relates the solutions with positive and negative frequencies. One should also notice the appearance of the term that has the structure of the effective magnetic field with a vector potential $\mathbf{A}(\rho) = \mathbf{e}_\chi q\cos\theta_0/r$ proportional to the topological charge $q$. This term is caused by the gyroscopic properties of the medium and is related to the topological properties of the soliton.

The potentials involved in Eq. (6) have the form

$$U = \frac{\cos\theta_0}{l_0^2}\left[\cos\theta_0 - \frac{\Omega}{\omega_0}\right] - \frac{\sin\theta_0^2}{2}\left(\frac{1}{l_0^2} + \frac{q^2}{r^2}\right) - \frac{\theta_0'^2}{2},$$

$$W = \frac{\sin\theta_0^2}{2}\left(\frac{1}{l_0^2} + \frac{q^2}{r^2}\right) - \frac{\theta_0'^2}{2}.$$

To solve Eq. (6), we use the expansion in partial waves [10, 6, 11]:

$$\psi = \sum_{\omega, m}(u_m e^{i\Phi_m} + i v_m e^{i\Phi_m}), \quad \Phi_m = m\chi - \omega_m t + \eta_m. \quad (7)$$

This method allows us to reduce the generalized Schrödinger equation (6) to the spectral problem

$$\mathscr{H}|\mathbf{m}) = \omega_m|\mathbf{m}), \quad \mathscr{H} = \left\|\begin{array}{cc} H_+ & -W \\ W & -H_- \end{array}\right\|,$$

$$|\mathbf{m}) = \left\|\begin{array}{c} u_m \\ v_m \end{array}\right\|. \quad (8)$$

Here, $H_\pm = -\nabla_r^2 + U + (|\mathbf{A}| \pm m/r)^2$ are 2D radial Schrödinger operators that have no negative eigenvalues and the integer $m$ has the meaning of the azimuthal

quantum number. Note that spectral problem (8) for the matrix Hamiltonian $\mathcal{H}$ fundamentally differs from the standard set of coupled Schrödinger equations: the operator $\mathcal{H}$ is Hermitian only in the Hilbert space with indefinite metric [11]:

$$(\mathbf{m}|\mathbf{m}) = \int_0^\infty (u^2 - v^2) r \, dr.$$

In this case, for all of the eigenvalues $\omega_m$, the operator $H_-$ has a resolvent and, hence, $v_m = (H_- + \omega_m)^{-1} W u_m$ is a slave variable of the spectral problem.

In the absence of the soliton, the magnon amplitudes are $u_m = J_{|m|}(kr)$ and $v_m = 0$. The interaction with the soliton leads to the scattering of magnons. Then, away from the soliton, the magnon modes have the form

$$u_m \propto J_m(kr) + \sigma_m(k) Y_m(kr). \tag{9}$$

Here, $J_n(x)$ and $Y_n(x)$ are the Bessel and Neumann functions of order $n$, $k$ is the wave number, $\sigma_m(k) = -\tan\delta_m(k)$ is the scattering amplitude, and $\delta_m(k)$ is the scattering phase. In the presence of the soliton, the formation of localized (bound) states is also possible. Distribution (7) includes all types of perturbations of the stationary soliton, including two local zero modes, namely, the rotational mode ($m = 0$) and the zero translational mode ($m = 1$). They appear due to the presence of two arbitrary parameters in solution (1): the position of the soliton center and the angle $\varphi_0$. For these modes, we can write a general formula in terms of $u$ and $v$:

$$u_m^0 = r^{1-m}\left[\theta_0' - \frac{\sin\theta_0}{r}\right], \quad v_m^0 = r^{1-m}\left[\theta_0' + \frac{\sin\theta_0}{r}\right]. \tag{10}$$

Perturbations associated with $\varphi_0$ do not cause any displacement of the soliton, and the symmetry related to the displacement of the soliton center determines the presence of the zero translational mode. For us, it is important that the full set of modes of spectral problem (8) also includes nonzero modes associated with the soliton displacement. The coordinate of the soliton can be written in the form $\mathbf{X}(t) = (S/Na^2)\int(1 - \cos\theta)\,\mathbf{r}\,d^2x$ [12]. This allows us to determine the perturbations that lead to a finite velocity of the soliton $d\mathbf{X}(t)/dt$. For the case of small perturbations, with the use of Eqs. (5), we obtain

$$\frac{d\mathbf{X}}{dt} = \frac{Sl_0^2\omega_0}{Na^2}\int d^2x \cos\theta_0[(\sin\theta_0\nabla\phi_0 + i\nabla\theta_0)\psi + \text{c.c.}].$$

Since $(\nabla\theta_0, \nabla\phi_0) \propto (\sin\chi, \cos\chi)$ and the other terms under the integral depend on $r$ alone, only the modes with $m = \pm 1$ possess the property of interest. Thus, the dynamics of $\mathbf{X}(t)$ can only be associated with the modes characterized by $|m| = 1$. In addition, the motion of the soliton as a particlelike object without the excitation of magnon modes in the whole volume of the system is only possible when the corresponding mode is localized.

The magnon modes localized by the soliton were studied in [13, 6]. In [6], with the use of the two-parameter shooting method, we showed that a soliton with a relatively large radius possesses a set of local modes with $|m| \leq m_{\max}(R)$. As the soliton radius decreases, the modes sequentially leave the gap region (the discrete spectrum region), pass to the continuous spectrum, and transform into quasilocal modes. For example, when $R \lesssim 2.8l_0$, all of the modes with $|m| > 2$ cease being localized, and when $R \lesssim 1.5l_0$, the system contains only one local nonzero mode with $m = -1$, which can be called the nonzero translational mode. As $R$ decreases, the frequency of this mode $\omega_{m=-1}$ asymptotically approaches the boundary of the continuous spectrum while the exponential decrease in the magnetization perturbation away from the soliton becomes slower, $r_0 \gg l_0$. The wave function becomes delocalized, and the numerical analysis based on the two-parameter shooting method becomes difficult and unreliable (in [6], it was actually possible to consider only solitons with $R \gtrsim 0.3l_0$). Therefore, the question of what should occur with a further decrease in the soliton radius remains open: whether the soliton will possess a nonzero translational mode in the case of small-radius solitons for the so-called magnetic skyrmions or this mode will pass to the magnon continuum by transforming into a quasilocal mode. As we noted above, this question is of fundamental significance in connection with the problem of applicability of Newtonian equations to the soliton dynamics.

The problem of the presence of a local mode can be solved independently by analyzing the scattering data. As was noted above, the local mode problem based on the two-parameter shooting method cannot be solved numerically for the limiting case of small soliton radius, but the problem of magnon scattering by a soliton can be numerically integrated for solitons as small as one likes with the use of the one-parameter shooting method [6]. The scattering data make it possible to derive a conclusion concerning the presence or absence of the local mode on the basis of the Levinson theorem, according to which the number of bound states and the total phase shift in the scattering data for a partial mode are related to each other. In the case of analyzing the soliton–magnon scattering, the problem is complicated by the fact that the effective potentials have singularities at zero (of the type of $\nu^2/r^2$) and at infinity ($\mu^2/r^2$), where the numbers $\nu$ and $\mu$ are not equal to $m$. Recently we generalized the Levinson theorem for such singular potentials [14] and showed that the total shift of the scattering phase (Eq. (9)) is determined by the expression

$$\delta_m(0) - \delta_m(\infty) = \pi\left[N_m^b + \frac{|\nu| - |\mu|}{2}\right].$$

In our case, $\nu = q - m$ and $\mu = q + m$ and the total phase shift can be represented as

$$\delta_m(0) - \delta_m(\infty) = \pi[N_m^{\mathrm{b}} - \mathrm{sgn}\, m].  \quad (11)$$

When the number of local modes changes by one, the total phase shift undergoes a jump by $\pi$, which can be used to determine the instant of disappearance of the local mode. The scattering data for the mode with $m = -1$ are shown in the figure. To illustrate the operation of the method, we present the scattering data for the mode with $m = -2$ in the same figure. In particular, as was shown in [6], a soliton with a sufficiently large radius has a local mode with $m = -2$. In this case, according to Eq. (11), the total phase shift is equal to $2\pi$. In the figure, this situation corresponds to the curve marked with full triangles. As the soliton radius decreases, the local mode leaves the discrete spectrum region; hence, the number of bound states decreases by one and the total phase shift becomes equal to $\pi$ (see the curves marked with empty triangles and empty circles). A numerical calculation performed for the mode $m = -1$ shows that, for any soliton radius, the total phase shift is equal to $2\pi$ (the curves with full circles and empty squares). A comparison of this result with Eq. (11) confirms the above conclusion that the nonzero local mode with $m = -1$ is always present for solitons of any radius.

To calculate the frequency of the nonzero translational mode, it is convenient to reformulate the spectral problem as a variational problem for the functional (Lagrangian)

$$\mathscr{L} = \omega_0 l_0^2 (\mathbf{m} | \mathcal{H} | \mathbf{m}) - \omega_m (\mathbf{m} | \mathbf{m}).  \quad (12)$$

For a small-radius soliton, all higher modes with $|m| > 1$ cease being local. Among the remaining three modes with $m = -1$, 0, and $+1$, two are nonzero. One of the main points in using the variational approach is the adequate choice of the trial function. For this purpose, we use the closeness of the structure of soliton solution (3) to the Belavin–Polyakov solution in a wide range of coordinate values $r \ll r_0$, $r \geq R$. For the Belavin–Polyakov soliton, all three modes with $m = -1$, 0, $+1$ have nonzero frequencies and are determined by Eqs. (10) [15]. For small-radius solitons, the trial functions for the mode $m = -1$ are most naturally chosen in the form of combinations of the functions $u_{\pm 1}^0$ and $v_{\pm 1}^0$ given by Eqs. (10):

$$u_{-1}^\omega = u_1^{\omega = 0} + ar^2 \theta_0' - br \sin \theta_0,$$
$$v_{-1}^\omega = u_1^{\omega = 0} + ar^2 \theta_0' + br \sin \theta_0.  \quad (13)$$
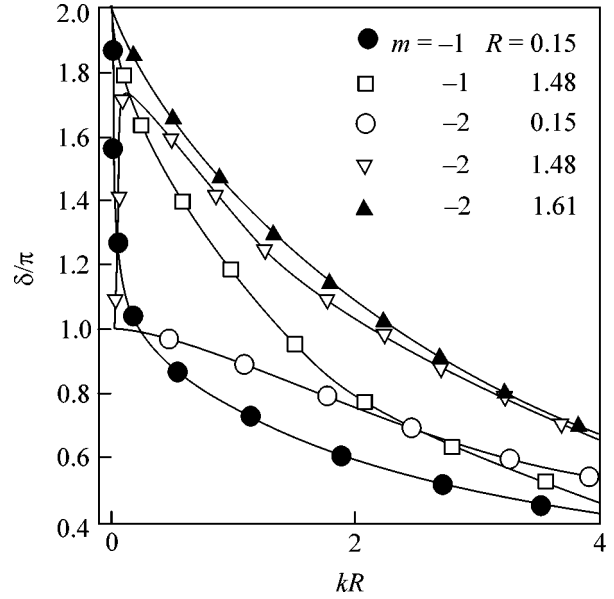
Phase shift for the modes with $m = -1$ and $-2$ and for various values of the soliton radius.

Effective Lagrangian (12) with these trial functions takes the form

$$L = (a + b)^2 \left\{ \langle \sin^2 \theta_0 \rangle - \frac{\omega}{2\omega_0} \langle 1 - \cos \theta_0 \rangle^2 \right\}$$
$$+ \frac{4ab\omega}{\omega_0 l_0^2} \langle r^2(1 - \cos \theta_0) \rangle + 2a^2 \langle r^2 \theta_0'^2 - \sin^2 \theta_0 \rangle,$$

where $\langle f(r) \rangle = \int_0^\infty f(r)\, r dr$. The conditions $\partial L / \partial a = 0$ and $\partial L / \partial b = 0$ lead to the following expression for the eigenfrequency of the nonzero translational mode:

$$\omega_{m=-1} = \frac{2\omega_0 l_0^2 F}{4\langle r^2(1 - \cos \theta_0) \rangle + l_0^2 F \langle 1 - \cos \theta_0 \rangle^2},  \quad (14)$$

where $F = \langle \sin^2 \theta_0 \rangle \langle r^2 \theta_0'^2 - \sin^2 \theta_0 \rangle$.

For the small-radius soliton of interest, the core structure is close to the structure of the Belavin–Polyakov soliton and, for $r \ll r_0$, the relation $r^2 \theta_0'^2 = \sin^2 \theta_0$ is satisfied. Therefore, the quantity $F$ is determined by the region lying away from the center, $r \geq r_0$:

$$F \approx \frac{\omega_0 - \Omega}{\omega_0 l_0^2} \langle \sin^2 \theta_0 \rangle \langle r^2 \sin^2 \theta_0 \rangle.$$

This quantity is always small. Now, estimating the average values using approximate solution (3), we obtain an

expression for the eigenfrequency (14):

$$\omega_{m=-1} \approx (\omega_0 - \Omega)\left[1 - \frac{2R^2(\omega_0 - \Omega)}{\omega_0 l_0^2}\ln\frac{\omega_0}{\omega_0 - \Omega}\right]. \quad (15)$$

Hence, one can see that, when the soliton radius decreases, the mode with $m = -1$ remains local but, as $R \longrightarrow 0$, its frequency asymptotically approaches the boundary of the continuum.

Thus, based on the analysis of the scattering problem for the generalized Schrödinger equation describing magnons on the background of a soliton, we proved the existence of a local translational magnon mode with nonzero frequency and azimuthal number $m = -1$. We analytically determined the frequency of this mode, which asymptotically tends to the spectrum boundary $\omega_0$ as the soliton radius decreases $R \ll l_0$. In terms of the soliton coordinate, this mode corresponds to the Larmor precession of the soliton center with a small amplitude. The inclusion of this mode and the mode with $m = +1$, which acquires a nonzero frequency in the presence of fixed boundary conditions for a circular magnet of radius $L$ (this leads to the appearance of the restoring force $F_{ext} = -\kappa\mathbf{r}$, where $\kappa \propto \exp(-L/r_0)$), unambiguously fits the Newtonian soliton dynamics described by Eq. (4). In this case, a slow motion of the soliton occurs with the mode frequency $\omega_{m=1}$, which, for small values of $\kappa$, can be represented as $\kappa/G$ and contains no inertial mass, as well as Larmor precession with the nonzero mode frequency $\omega_{m=-1} = G/m_*$. The calculation performed for the frequency $\omega_{m=-1}$ allows us to determine the effective soliton mass

$$m_* = \frac{G}{\omega_{m=-1}} \approx \frac{4\pi\hbar S}{a^2(\omega_0 - \omega)}. \quad (16)$$

As the soliton radius decreases, $\omega \longrightarrow \omega_0$ and the soliton mass infinitely increases. Hence, the soliton loses its mobility with decreasing radius.

## REFERENCES

1. A. M. Kosevich, B. A. Ivanov, and A. S. Kovalev, *Nonlinear Waves of Magnetization: Dynamical and Topological Solitons* (Naukova Dumka, Kiev, 1983) [in Russian]; Phys. Rep. **194**, 117 (1990); V. G. Bar'yakhtar and B. A. Ivanov, Sov. Sci. Rev., Sect. A **16**, 3 (1993).

2. A. A. Belavin and A. M. Polyakov, Pis'ma Zh. Éksp. Teor. Fiz. **22**, 503 (1975) [JETP Lett. **22**, 245 (1975)].

3. R. H. Hobard, Proc. Phys. Soc. **82**, 201 (1963); G. H. Derrick, J. Math. Phys. **5**, 1252 (1964).

4. B. A. Ivanov and A. M. Kosevich, Pis'ma Zh. Éksp. Teor. Fiz. **24**, 495 (1976) [JETP Lett. **24**, 454 (1976)].

5. A. S. Kovalev, A. M. Kosevich, and K. V. Maslov, Pis'ma Zh. Éksp. Teor. Fiz. **30**, 321 (1979) [JETP Lett. **30**, 296 (1979)].

6. D. D. Sheka, B. A. Ivanov, and F. G. Mertens, Phys. Rev. B **64**, 024 432 (2001).

7. F. G. Mertens and A. R. Bishop, in *Nonlinear Science at the Dawn of the 21st Century*, Ed. by P. L. Christiansen, M. P. Soerensen, and A. C. Scott (Springer, Berlin, 2000).

8. N. Papanicolaou and T. N. Tomaras, Nucl. Phys. B **360**, 425 (1991); N. Papanicolaou and W. J. Zakrzewski, Physica D (Amsterdam) **80**, 225 (1995); B. Piette and W. J. Zakrzewski, Physica D (Amsterdam) **119**, 314 (1998).

9. K. Lonngren and A. Scott, *Solitons in Action* (Academic, New York, 1978).

10. B. A. Ivanov, H. J. Schnitzer, F. G. Mertens, and G. M. Wysin, Phys. Rev. B **58**, 8464 (1998).

11. D. D. Sheka, I. A. Yastremsky, B. A. Ivanov, *et al.*, Phys. Rev. B **69**, 054 429 (2004).

12. D. D. Sheka, C. Schuster, B. A. Ivanov, and F. G. Mertens, cond-mat/0505542 (2005).

13. F. K. Abdullaev, R. M. Galimzyanov, and A. S. Kirakosyan, Phys. Rev. B **60**, 6552 (1999).

14. D. Sheka, B. Ivanov, and F. G. Mertens, Phys. Rev. A **68**, 012 707 (2003).

15. B. A. Ivanov, Pis'ma Zh. Éksp. Teor. Fiz. **61**, 898 (1995) [JETP Lett. **61**, 917 (1995)].

*Translated by E. Golyamina*

# EPR Identification of the Triplet Ground State and Photoinduced Population Inversion for a Si–C Divacancy in Silicon Carbide

**P. G. Baranov[a], I. V. Il'in[a], E. N. Mokhov[a], M. V. Muzafarova[a], S. B. Orlinskii[b], and J. Schmidt[b]**

[a] *Ioffe Physicotechnical Institute, Russian Academy of Sciences, St. Petersburg, 194021 Russia*
*e-mail: Pavel.Baranov@mail.ioffe.ru*
[b] *Huygens Laboratory, Department of Physics, Leiden University, Leiden, The Netherlands*
Received August 17, 2005

It is shown that intrinsic defects responsible for the semi-insulating properties of SiC represent Si–C divacancies in a neutral state $(V_{Si}–V_C)^0$, which have the triplet ground state. The energy level scheme and the mechanism of creating the photoinduced population inversion of the triplet sublevels of the divacancy ground state are determined. It is concluded that there is a singlet excited state through which spin polarization is accomplished, and this fact opens the possibility of detecting magnetic resonance on single divacancies. © 2005 Pleiades Publishing, Inc.

PACS numbers: 61.72.Ji, 61.72.Bb, 76.30.–v

There is a demand for replacing vanadium impurities responsible for the semi-insulating properties of silicon carbide (SiC) with intrinsic defects to create semi-insulating substrates required for manufacturing device structures. A similar problem was solved when the semi-insulating properties of GaAs were optimized by means of replacing chromium impurities by intrinsic *EL2* defects. So-called *P6* and *P7* defects were detected in semi-insulating SiC crystals by the electron paramagnetic resonance (EPR) technique (these defects were observed in SiC crystals in [1]), and the suggestion was made that these defects are responsible for the semi-insulating properties of SiC [2]. The EPR spectra of *P6* and *P7* centers were observed in [1] only upon optical illumination; therefore, it was suggested that these centers belong to a triplet excited state of a Si–C divacancy $(V_{Si}–V_C)$. Recently, based on optically detected EPR studies, the structure of *P6* and *P7* centers has been reinterpreted and a model has been proposed in the form of a $C_{Si}–V_C$ pair in which $C_{Si}$ represents a carbon atom at a silicon position, that is, an antisite defect, and the EPR spectra correspond to a triplet excited state of the defect [3]. In fact, the latter interpretation implies a triplet excited state of a silicon vacancy that encompasses one of four carbon atoms located in the nearest environment of the vacancy with a carbon vacancy remaining nearby. The main point of this interpretation was the statement that the EPR spectrum belongs to a triplet excited state, because it is difficult to imagine that this structure could form directly in the crystal after annealing at 700–1000°C and would not exist immediately after irradiation with neutrons.

Before our work, the EPR spectra of *P6* and *P7* centers had been observed only upon optical illumination, which has led to a wrong interpretation of their ground state and, as a consequence, to an erroneous model of their structure. A similar mistake was made in the interpretation of the triplet state of the known N–V defect in diamond [4] and the neutral $V_{Si}^0$ vacancy in SiC [5]. It was considered that EPR spectra belong to the triplet excited states of the corresponding defects, because these spectra were observed only upon optical illumination. In fact, the reason for the observation of EPR spectra was optical alignment in the triplet ground state through a metastable singlet state and deviation of the population of triplet levels from the Boltzmann distribution, as a result of which the EPR signal was sharply enhanced. This problem was solved when the concentration of defects was increased and it became possible to observe the EPR spectra of the N–V defect in diamond [6] and $V_{Si}^0$ in SiC [7] without optical illumination at low temperatures, which unambiguously pointed to the existence of the triplet ground state.

The aim of this work is to prove the existence of the triplet ground state for *P6* (*P7*) centers, to elucidate the mechanism of creating the population inversion of spin sublevels in the ground state and, as a result, to argue that the structure of the center represents a $V_{Si}–V_C$ divacancy in the neutral state.

The EPR experiments were performed at low temperatures (1.2–4 K) in total darkness, which excluded the possibility of thermal or optical population of the excited state. The EPR spectra were detected in the
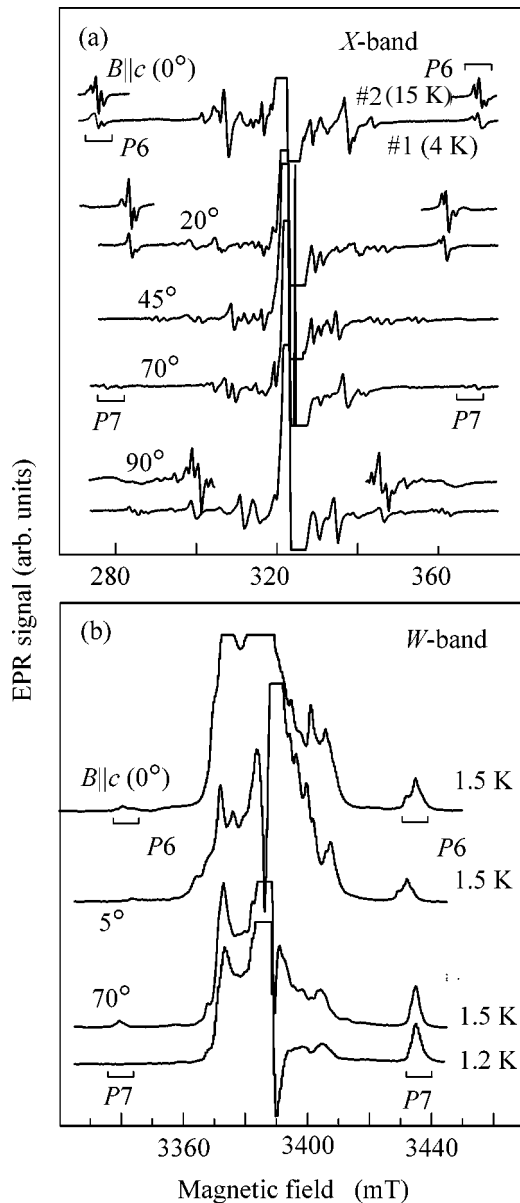
**Fig. 1.** EPR spectra of the *P6* and *P7* centers in a 6H-SiC crystal measured in samples 1 and 2 for several orientations in darkness (a) in the *X* range at 4 K (sample 1) and 15 K (sample 2) and (b) by the ESE technique in the *W* range at 1.2 and 1.5 K in sample 1.

*X* range (9.3 GHz) on a cw radiospectrometer in the temperature range 3.5–300 K and also in the *W* range (95 GHz) on a pulse electron spin echo (ESE) spectrometer at temperatures 1.2–2 K. The results of studying four 6H-SiC samples exposed to various doses of irradiation with fast neutrons. Samples 1 and 2 were irradiated with neutrons with a dose of $10^{20}$ cm$^{-2}$, and samples 3 and 4 were irradiated with neutrons with a dose of $10^{18}$ cm$^{-2}$. Sample 4 was grown with a changed isotope composition of $^{13}$C (13% $^{13}$C at the natural concentration of 1.1%, the exact concentration of $^{13}$C was determined by the hyperfine (HF) structure observed in

the EPR spectrum of a silicon vacancy). After neutron irradiation, all samples were subjected to annealing at a temperature of 700°C for 20 min.

Figure 1a presents EPR spectra measured for samples 1 (4 K) and 2 (15 K) (particular lines for *P6* centers are given, the relative intensities of EPR lines for *P7* centers in this sample are considerably lower) in the *X* range in darkness for several crystal orientations in the magnetic field. The EPR spectra are described by the standard spin Hamiltonian for the electronic spin *S* = 1 with parameters coinciding within the experimental error with the corresponding values reported in [1] for *P6* and *P7* centers. The orientations *B* ∥ *c* (θ = 0°) and θ = 70° correspond to the symmetry axes of *P6* and *P7* centers, respectively, and the EPR spectra of *P6* and *P7* centers marked with brackets exhibit a maximum hyperfine structure splitting in these orientations. The signals for each center consist of three pairs of lines corresponding to different positions in the lattice of the 6H-SiC polytype. Figure 1b demonstrates ESE signals measured in sample 1 at a high frequency (95 GHz) and at very low temperatures (1.2–1.5 K) in total darkness.

The intensities of the low- and high-field fine-structure components measured in the EPR spectra by ESE at temperatures of 1.2 and 1.5 K sharply differ from each other because of a strong difference in the populations of triplet sublevels at low temperatures and large Zeeman splittings. The ratio of intensities of these components gives direct information on the temperature of the sample and allows the sign of the fine-structure splitting *D* to be determined ($D > 0$).
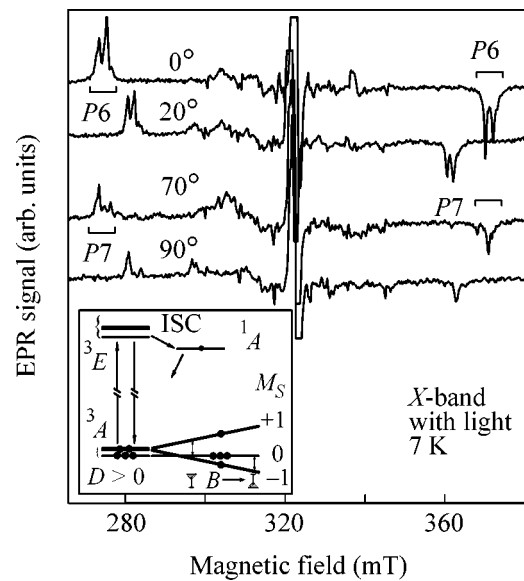
Figure 2 presents the EPR spectra of *P6* and *P7* centers measured in sample 3 under continuous optical illumination in the visible range. In this case, the distribution of populations of the triplet sublevels deviates from the Boltzmann distribution. As a result, emission rather than absorption was detected for the high-field transition because of the creation of the population inversion for the triplet sublevels. In crystals exposed to high doses of neutron irradiation, the EPR signal of *P6* (*P7*) centers is observed directly without photoexcitation, because the concentration of defects is high and the spin–lattice relaxation time *T1* is shorter. For low concentrations of defects, the EPR signal is saturated because of long *T1* [1], which also hinders its observation.

The detection of the EPR spectra of *P6* (*P7*) centers at low temperatures in darkness proves that the ground state of these centers is triplet ($S = 1$) rather than singlet as was argued in [1, 3]. One of the arguments presented in [3] in favor of the presence of $C_{Si}$ in the structure of *P6* centers was an observation of the HF interaction with one carbon atom of 48 MHz. We do not consider this result a weighty argument. Firstly, the EPR spectra in [3] were measured only for one orientation, *B* ∥ *c*, and a small inaccuracy in the orientation would lead to a change in the ratio of intensities of EPR signals. Thus, it seems that the observed structure corresponds to

interaction with three C atoms, which corresponds to the value of HF interaction with three C atoms for a neutral silicon vacancy [8]. Secondly, the value 48 MHz seems to be very small for the HF interaction in $C_{Si}$ (approximately 1% spin density on C under the suggestion that this is an isotropic HF interaction constant). In 6H-SiC crystals containing 13% $^{13}$C (sample 3), we detected centers with $S = 1/2$ for which we observed HF interaction with one C atom with constants $A_{\parallel} = 230$ MHz and $A_{\perp} = 87$ MHz. This approximately corresponds to the spin-density distribution 44% on the carbon $2p$ orbital and 3.6% on the carbon $2s$ orbital. Such values, being the maximum observed HF interaction with carbon in SiC, are evidently typical for a single C atom in an antisite defect or for an interstitial C atom. The results of studying this center will be presented in a subsequent publication. It should be added that the energies and structure of the phononless lines, whose relation to $P6$ ($P7$) centers was proved in [3], are close to the corresponding characteristics for a neutral silicon vacancy. This also gives evidence in favor of the presence of a neutral silicon vacancy in the structure of $P6$ ($P7$) centers. Thus, the model suggested by the authors of [3] as a $C_{Si}$–$V_C$ pair, which is currently used in numerous publications (see, for example, [2]) does not comply with new experimental data and should be reconsidered.

We believe that the $P6$ ($P7$) centers represent the most natural defect in the form of a silicon–carbon divacancy in the neutral state $(V_{Si}–V_C)^0$. The divacancy axis in the $P6$ center is oriented along a bond parallel to crystal axis $c$, and the divacancy axis in the $P7$ center is oriented along a bond that is not aligned with axis $c$.

To explain photokinetic processes in a $(V_{Si}–V_C)^0$ divacancy in silicon carbide based on the available experimental data, an energy level scheme is proposed that includes the levels of the $^3A$ ground state, $^3E$ excited state, and the metastable $^1A$ singlet state (inset in Fig. 2); that is, the conclusion is drawn that there exists a singlet excited state through which spin polarization is accomplished. Luminescence and optical absorption are due to transitions between spin sublevels of the $^3E$ and $^3A$ states. Here, it may be suggested (as well as in the N–V defect in diamond [9]) that nonradiative transitions between the $^3E$ and $^1A$ states (so-called intersystem crossing, ISC) are strictly spin-dependent and that the rate of the transition between the sublevel $M_S = 0$ of the $^3E$ state and the $^1A$ state is much lower as compared with transitions from sublevels with $M_S = \pm1$. On the contrary, the rates of nonradiative transitions $^1A \longrightarrow {}^3A$ are approximately similar for all sublevels. As a result, the level with $M_S = 0$ in the $^3A$ ground state is filled predominantly; that is, population inversion is created and only transitions between the levels with $M_S = 0$ in the ground and $^3E$ excited states contribute to photoluminescence and photoabsorption. The existence of a deep analogy in the properties of the $(V_{Si}–V_C)^0$ divacancy in silicon carbide and the N–V defect in dia-



**Fig. 2.** EPR spectra of the $P6$ and $P7$ centers in a 6H-SiC crystal measured in sample 3 for several orientations under optical illumination. The inset presents the energy level scheme and the optical alignment process for the triplet sublevels of the ground state of a neutral $(V_{Si}–V_C)^0$ divacancy.

mond, for which magnetic resonance on a single defect was first detected [9], allows the divacancy in silicon carbide to be considered a potential defect for the spectroscopy of individual quantum objects.

## REFERENCES

1. V. S. Vainer and V. A. Il'in, Sov. Phys. Solid State **23**, 2126 (1981).
2. W. E. Carlos, E. R. Glaser, and D. V. Shanabrook, Physica B (Amsterdam) **340–342**, 151 (2003).
3. Th. Lingner *et al.*, Phys. Rev. B **64**, 245 212 (2001).
4. J. H. N. Loubser and J. A. van Wyk, Rep. Prog. Phys. **41**, 1201 (1978).
5. E. Sörman, N. T. Son, W. M. Chen, *et al.*, Phys. Rev. B **61**, 2613 (2000).
6. D. A. Redman, S. Brown, R. H. Sands, and S. R. Rand, Phys. Rev. Lett. **67**, 3420 (1991).
7. S. B. Orlinski, J. Schmidt, E. N. Mokhov, and P. G. Baranov, Phys. Rev. B **67**, 125207 (2003).
8. Mt. Wagner, N. Q. Thinh, N. T. Son, *et al.*, Phys. Rev. B **66**, 155214 (2002).
9. A. Gruber, A. Drabenstedt, C. Tietz, *et al.*, Science **276**, 2012 (1997); A. P. Nizovtsev, S. Ya. Kilin, F. Jelezko, *et al.*, Physica B (Amsterdam) **340–342**, 106 (2003).

*Translated by A. Bagatur'yants*

# Nature of Low–Temperature Phase Transitions in CaMn$_7$O$_{12}$

## O. Volkova[a], Yu. Arango[b], N. Tristan[b], V. Kataev[b], E. Gudilin[a], D. Meier[c], T. Lorenz[c], B. Büchner[b], and A. Vasil'ev[a]

*[a] Moscow State University, Vorob'evy gory, Moscow, 119992 Russia*
*[b] Leibniz Institute for Solid State and Materials Research, D-01171 Dresden, Germany*
*[c] Institute of Physics II, University of Cologne, D-50937 Cologne, Germany*
Received August 17, 2005

New data on the specific heat, thermal expansion, and magnetization of the CaMn$_7$O$_{12}$ phase require a revision of the current concepts of the sequence of phase transitions in this compound. It is found that a spin-glass phase transition occurs in CaMn$_7$O$_{12}$ at $T_M = 49$ K, whereas the transition at $T_S = 89$ K exhibits the features of a first-order phase transition and thereby is apparently of structural origin. In the range $T_M < T < T_S$, the CaMn$_7$O$_{12}$ compound exhibits negative thermal expansion, which is also indicative of structural changes. © 2005 Pleiades Publishing, Inc.

PACS numbers: 65.40.–b, 75.47.Lx

Among the materials with colossal magnetoresistance, the Ca(Cu$_x$Mn$_{3-x}$)Mn$_4$O$_{12}$ solid solution exhibited one of the highest characteristics in weak magnetic fields over a wide temperature range [1, 2]. This compound belongs to the family of distorted double perovskites with the general formula AC$_3$B$_4$O$_{12}$, where position C is occupied by Jahn–Teller cations (Cu$^{2+}$, Mn$^{3+}$), position A can be occupied by a cation of sufficiently great radius (Na$^+$, Ca$^{2+}$, or a trivalent rare-earth metal cation), and position B is occupied by cations in an octahedral oxygen environment to form the metal–oxygen structure skeleton [3]. In terms of magnetoresistance, these materials are competitive with common perovskites La$_{1-x}$A$_x$MnO$_3$ (A = Sr [4–6], Ba [7], or Ca [8, 9]), pyrochlores A$_2$Mn$_2$O$_7$ (A = Tl [10], In, or Y [11]), and spinels Fe$_{1-x}$A$_x$Cr$_2$S$_4$ (A = Cu [12]). It is of importance that high Curie temperatures are reached in all of these materials. In this case, the magnetic ordering occurs under the action of a double-exchange mechanism with the partial replacement of La$^{3+}$ in perovskites and Fe$^{2+}$ in spinels by cations with lower oxidation numbers, i.e., by the electron doping of the metal–oxygen skeleton and the appearance of mixed-valence cations in metal–oxygen chains. The variable-valence cations of transition metals are absent from pyrochlores and fully substituted double perovskites, and high Curie temperatures are reached because of exchange interactions [13].

CaMn$_7$O$_{12}$ (or CaMn$_3$Mn$_4$O$_{12}$) is the base compound in the family of distorted double perovskites AC$_3$B$_4$O$_{12}$ [14]. This compound exhibits cubic symmetry at high temperatures and undergoes a transition to a rhombohedral phase, space group $R\bar{3}$, at $T_{CO} = 450$ K as the temperature decreases [15]. The driving force of this transition is the ordering of charges in the octahedral position B, which contains the mixed-valence Mn$^{3+}$ and Mn$^{4+}$ ions in a ratio of 3 : 1. Only Mn$^{3+}$ ions occupy the pseudosquare position C.

Data on the magnetic properties of CaMn$_7$O$_{12}$ are contradictory. In publications on the magnetic properties of CaMn$_7$O$_{12}$, it was noted that this compound turned into an antiferromagnetically ordered state at 21 [2], 45 [16], or 85 K [17]. Based on neutron-diffraction and synchrotron studies, Przenioslo *et al.* [18–22] stated that two modulated magnetic α and β phases coexisted in CaMn$_7$O$_{12}$ over the range 2–49 K, whereas a ferrimagnetic α phase and a modulated β phase coexisted over the range 49–90 K. However, the parameters of these phases were not found.

This study was stimulated by contradictory opinions on the determination of the physical properties of CaMn$_7$O$_{12}$, which is the parent compound for an important family of Ca(Cu$_x$Mn$_{3-x}$)Mn$_4$O$_{12}$ materials with colossal magnetoresistance.

The ceramic samples of CaMn$_7$O$_{12}$ were prepared from CaCO$_3$ and Mn$_2$O$_3$ using solid-phase synthesis in a flow of oxygen at $T = 950°$C by the annealing of a homogenized mixture for 72 h. The phase composition was monitored by x-ray diffraction analysis. The specific heat of the samples was measured with a Termis quasiadiabatic relaxation calorimeter over the range 5–250 K. The magnetization was measured with a Quantum Design SQUID magnetometer over the range 5–250 K. The thermal expansion was measured by dilatometry over the range 5–150 K. The *g*-factor value for the test compound was determined by electron paramagnetic resonance spectroscopy at room temperature.

All of the physical quantities studied in this work exhibited clearly pronounced anomalies at 49 and 89 K.

Figure 1 shows the temperature dependence of magnetization $M$ in $CaMn_7O_{12}$ measured under zero-field cooling (ZFC) and field-cooling (FC) conditions. The behavior characteristic of a spin glass was observed below $T_M = 49$ K; i.e., the $M(T)$ functions in FC and ZFC modes exhibited a hysteresis. At $T > 49$ K, these functions coincided with each other and exhibited an anomalous kink at $T_S = 89$ K. At $T > 89$ K, the magnetization behavior obeyed the Curie–Weiss law with the effective magnetic moment $\mu_{eff} = 15.1\mu_B$ and the Weiss temperature $\theta = -85$ K. At the experimental spectroscopic splitting factor $g = 2.133$, the calculated effective magnetic moment of this compound was $14.9\mu_B$.

Figure 2 shows the temperature dependence of specific heat $C$ in $CaMn_7O_{12}$. At $T_M$ and $T_S$, this function exhibits singularities characteristic of second-order phase transitions.

Figure 3 shows the temperature dependence of the thermal expansion $\Delta L/L$ in $CaMn_7O_{12}$. The sample volume increased with temperature; however, a sharp kink was observed at $T_M$ and the sample contracted in the range from $T_M$ to $T_S$. A jump of thermal expansion can also be seen at $T_S$. The above special features are more clearly pronounced in Fig. 4, which demonstrates the temperature dependence of the thermal expansion coefficient $\alpha$. A singularity at $T_M$ is characteristic of a second-order phase transition, whereas an anomaly at $T_S$ exhibits features characteristic of both first-order and second-order phase transitions.

In the neutron-diffraction studies [18, 19], the appearance of new scattering peaks at two temperatures, $T_M$ and $T_S$, was interpreted as the formation of two different magnetic structures. It was noted that the spacing of the ferrimagnetic structure formed at $T_S$ coincided with the unit cell spacing and did not depend on temperature, whereas the spacing of a modulated magnetic structure formed at $T_M$ depended on temperature. Qualitatively, the half widths of additional peaks that appeared at $T_M$ and $T_S$ as functions of temperature were also different.

The experimental data allowed us to hypothesize different natures of phase transitions at $T_M$ and $T_S$. Thus, the appearance of a spin-glass state, which is characteristic of disordered magnetic systems, can be seen only at $T < T_M$. A weak anomaly in the specific heat and a jump in the thermal expansion coefficient at $T_M$, which are characteristic of a second-order phase transition, suggest that a magnetic ordering occurs in $CaMn_7O_{12}$ at this temperature.

The absence of spin-glass effects over the range $T_M < T < T_S$, a great anomaly in the $C(T)$ function, and a jump of the thermal expansion $\Delta L/L$ at $T_S$ indicate a structural origin of this phase transition. In the absence of detailed structural information on the phase transition in $CaMn_7O_{12}$ at this temperature, the origin of this phase transition is open to speculation. In the unit cell
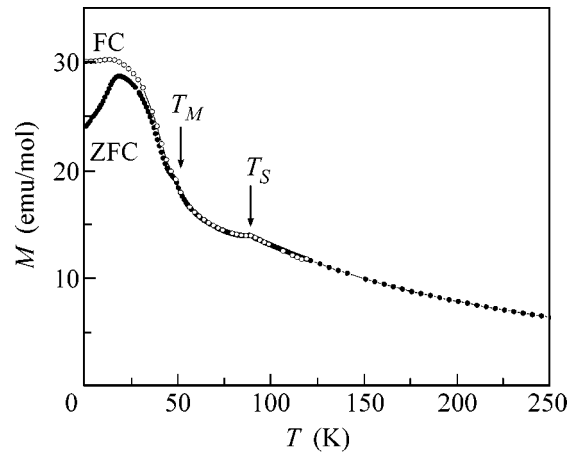
**Fig. 1.** Temperature dependence of the magnetization of $CaMn_7O_{12}$ under (●) zero-field cooling (ZFC) and (○) field-cooling (FC) conditions at $H = 0.01$ T.



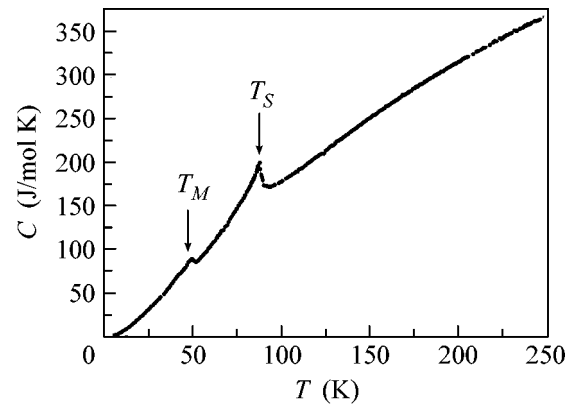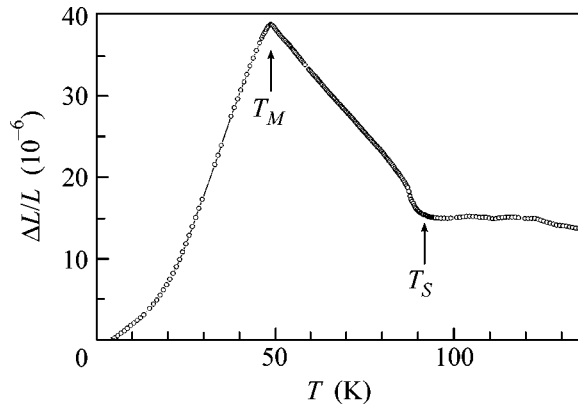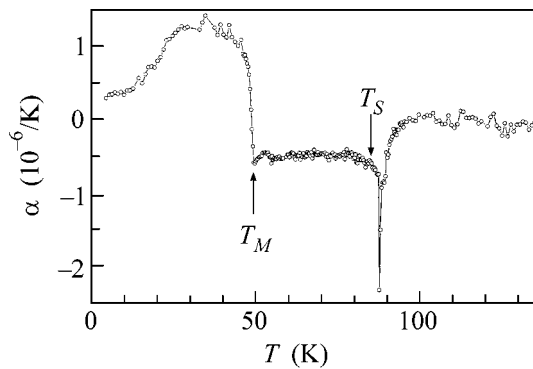**Fig. 2.** Temperature dependence of the specific heat of $CaMn_7O_{12}$.



**Fig. 3.** Temperature dependence of the thermal expansion of $CaMn_7O_{12}$.

**Fig. 4.** Temperature dependence of the thermal expansion coefficient of $CaMn_7O_{12}$.

of this compound, the Jahn–Teller cations $Mn^{3+}$ occur at two nonequivalent crystallographic positions. The *d*-orbital splitting schemes of manganese in pseudosquare and octahedral positions differ from each other; however, they do not contain partially occupied degenerate levels. Because of this, the Jahn–Teller effect cannot be considered as the driving force of this transition. However, the admixing of the wave functions of higher energy levels to the main wave functions of *d* electrons can serve as the driving force. This can result in a sort of orbital ordering in $CaMn_7O_{12}$.

Thus, the set of the experimental data on the thermodynamic properties of $CaMn_7O_{12}$ suggests that this compound undergoes phase transitions of a different nature at $T_M = 49$ K and $T_S = 89$ K. All of the special features of the transition at 49 K are consistent with the hypothesis on its magnetic origin. To reveal the nature of the phase transition at 89 K, either data on the elastic scattering of neutrons should be newly interpreted or new measurements in a single-crystal sample should be performed.

## REFERENCES

1. Z. Zeng, M. Greenblatt, M. A. Subramanian, and M. Croft, Phys. Rev. Lett. **82**, 3164 (1999).
2. Z. Zeng, M. Greenblatt, J. E. Sustrom IV, *et al.*, J. Solid State Chem. **147**, 185 (1999).
3. A. Collomb, D. Samaras, J. L. Buevoz, *et al.*, J. Magn. Magn. Mater. **40**, 75 (1983).
4. T. Okuda, A. Asamitsu, Y. Tomioka, *et al.*, Phys. Rev. Lett. **81**, 3203 (1998).
5. B. Woodfield, M. Wilson, and J. Byers, Phys. Rev. Lett. **78**, 3201 (1997).
6. J. Coey, M. Viret, L. Ranno, and K. Ounadjela, Phys. Rev. Lett. **75**, 3910 (1995).
7. J. Hamilton, E. Keatley, H. Ju. A. Raychaudhuri, *et al.*, Phys. Rev. B **54**, 14 926 (1996).
8. L. Ghivelder, I. Castillo, N. Alford, *et al.*, J. Magn. Magn. Mater. **189**, 274 (1998).
9. V. Smolyaninova, J. Hamilton, R. Green, *et al.*, Phys. Rev. Lett. **55**, 5640 (1997).
10. P. Velasco, J. A. Alonso, M. T. Casais, *et al.*, J. Phys.: Condens. Matter **16**, 8725 (2004).
11. Y. Shimakawa, Y. Kubo, N. Hamada, *et al.*, Phys. Rev. B **59**, 1249 (1999).
12. Z. Chen, S. Tan, Z. Yang, and Y. Zhang, Phys. Rev. B **59**, 11 172 (1999).
13. M. A. Subramanian, B. H. Toby, A. P. Ramirez, *et al.*, Science **273**, 81 (1996).
14. B. Bochu, J. L. Buevoz, J. Chenavas, *et al.*, Solid State Commun. **36**, 133 (1980).
15. A. Deschanvres, B. Raveau, and F. Tollemer, Bull. Soc. Chim. Fr., 4077 (1967).
16. I. O. Troyanchuk, A. Chernyi, and Y. G. Zonov, Phys. Solid State **31**, 283 (1989).
17. I. O. Troyanchuk, L. S. Lobanovsky, N. V. Kasper, *et al.*, Phys. Rev. B **58**, 14 903 (1998).
18. R. Przenioslo, I. Sosnowska, E. Suard, *et al.*, Physica B (Amsterdam) **344**, 358 (2004).
19. R. Przenioslo, I. Sosnowska, D. Hohlwein, *et al.*, Solid State Commun. **111**, 687 (1999).
20. R. Przenioslo, I. Sosnowska, M. Zoltek, *et al.*, Physica B (Amsterdam) **241–243**, 730 (1998).
21. R. Przenioslo, I. Sosnowska, E. Suard, and T. Hansen, Appl. Phys. A **74**, S1731 (2002).
22. R. Przenioslo, I. Sosnowska, P. Strunz, *et al.*, Physica B (Amsterdam) **276–278**, 547 (2000).

*Translated by V. Makhlyarchuk*

# Pressure-Induced Antiferromagnetism
# in La$_{0.75}$Ca$_{0.25}$MnO$_3$ Manganite

**D. P. Kozlenko[a], S. E. Kichanov[a,\*], V. I. Voronin[b], B. N. Savenko[a], V. P. Glazkov[c],**
**E. A. Kiseleva[d], and N. V. Proskurnina[b]**

*[a] Joint Institute for Nuclear Research, Dubna, Moscow region, 141980 Russia*
*\* e-mail: ekich@nf.jinr.ru*
*[b] Institute of Metal Physics, Ural Division, Russian Academy of Sciences, Yekaterinburg, 620219 Russia*
*[c] Russian Research Centre Kurchatov Institute, Moscow, 123182 Russia*
*[d] Ural State University, Yekaterinburg, 620083 Russia*
Received August 17, 2005

The crystal and magnetic structures of La$_{0.75}$Ca$_{0.25}$MnO$_3$ manganite are studied under high pressures up to 4.5 GPa in the temperature range 12–300 K by the neutron diffraction method. At normal pressure and temperature $T_C$ = 240 K, a ferromagnetic state is formed in La$_{0.75}$Ca$_{0.25}$MnO$_3$. At high pressures $P \geq 1.5$ GPa and at temperatures $T < T_N \approx 150$ K, a new A-type antiferromagnetic state appears. A further increase in pressure leads to an increase in the volume fraction of the antiferromagnetic phase, which coexists with the initial ferromagnetic phase. The effect of high pressure causes a considerable increase in $T_C$ with the slope $dT_C/dP \approx 12$ K/GPa. Calculations performed in the framework of the double exchange model with allowance for the electron–phonon interaction make it possible to explain this pressure dependence of $T_C$ on the basis of experimental data. © 2005 Pleiades Publishing, Inc.

PACS numbers: 61.12.Ld, 62.50.+p, 75.25.+z

## INTRODUCTION

Perovskitelike A$_{1-x}$A$'_x$MnO$_3$ manganites (where A and A' are rare-earth and alkaline-earth elements) exhibit a wide variety of physical properties depending on the type of the elements A and A' and on the doping level $x$. A strong correlation of magnetic, electronic, and transport properties of manganites leads to their high sensitivity to external actions, such as temperature variation or application of magnetic field or high pressure. A good example is the colossal magnetoresistance effect observed in manganites [1].

The magnetic properties of manganites are determined by the balance of two competing interactions: the double exchange, which is related to the kinetic energy gain due to the transport of delocalized $e_g$ electrons in Mn$^{3+}$–O$^{2-}$–Mn$^{4+}$ chains and contributes to the ferromagnetic ordering of Mn magnetic moments, and the antiferromagnetic superexchange between the Mn magnetic moments, which are formed by localized $t_{2g}$ electrons [1–4]. For concentrations $0.2 < x < 0.5$, the double exchange is usually the dominant type of interaction, and this leads to the transition from paramagnetic insulator state to ferromagnetic metal at the Curie temperature approximately equal to the insulator–metal transition temperature: $T_C = T_{IM}$ [1].

In manganites with orthorhombic crystal structure, a strong effect on the transport and magnetic properties is also produced by the electron–phonon coupling associated with the static cooperative Jahn–Teller distortion of oxygen octahedra. It leads to the formation of polarons and to an additional localization of charge carriers. Recently, in the La$_{0.75}$Ca$_{0.25}$MnO$_3$ compound, an anomalous behavior under high pressures was observed for the temperature $T_{IM}$ [5] and the frequency of the phonon oscillation mode of oxygen octahedra with the $B_{2g}(1)$ symmetry [6]. In the pressure range $P < 5$ GPa, $T_{IM}$ was found to increase with an average slope $dT_{IM}/dP \approx 15$ K/GPa; under higher pressures, the latter quantity decreased down to $dT_{IM}/dP \approx 2$ K/GPa [5]. In the pressure range $P < 7.5$ GPa, an increase in the mode frequency $\omega_{B_{2g}(1)}$ was observed with the slope $d\omega_{B_{2g}(1)}/dP \approx 1$ meV/GPa, and, as the pressure increased further, this value remained almost constant with only a slight dependence on pressure [6]. The study of the crystal structure of La$_{0.75}$Ca$_{0.25}$MnO$_3$ revealed a change in the orthorhombic distortion of the unit cell and in the Jahn–Teller distortion of oxygen octahedra at $P \sim 6$ GPa [7].

The aforementioned facts suggest a possibility for the existence of a new high-pressure phase of La$_{0.75}$Ca$_{0.25}$MnO$_3$ with properties different from those of the normal-pressure modification. The changes observed in the properties of La$_{0.75}$Ca$_{0.25}$MnO$_3$ under high pressures may be related to changes in not only the crystal structure but also in the magnetic one. However,
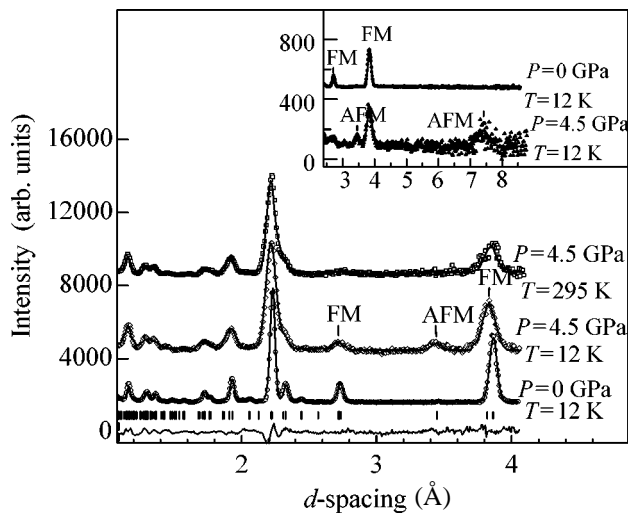
**Fig. 1.** Diffraction spectra of $La_{0.75}Ca_{0.25}MnO_3$ that are measured at $P = 0$ and 4.5 GPa and at $T = 295$ and 12 K (the scattering angles are $2\theta = 90°$ and 45.5°; see the inset) and are processed by the Rietveld method. The plot shows the experimental points, the calculated profile, and the difference curve (for $P = 4.5$ GPa and $T = 295$ K). The vertical bars indicate the calculated positions of the structural diffraction peaks. The most intense antiferromagnetic peaks and the peaks with the ferromagnetic contribution are marked as AFM and FM, respectively.

the effect of high pressures ($P > 1$ GPa) on the magnetic structure of $La_{0.75}Ca_{0.25}MnO_3$ has never been studied. In this paper, we report on the study of the effect of high external pressure on the atomic and magnetic structures of $La_{0.75}Ca_{0.25}MnO_3$ manganite at low temperatures by the neutron diffraction method and investigate the relation between the observed structural changes and the changes in the magnetic and transport properties.

## EXPERIMENTAL PROCEDURE

A $La_{0.75}Ca_{0.25}MnO_3$ polycrystal sample was obtained using the standard ceramic technology. The initial reagents were $La_2O_3$ (lanthanum oxide), $CaCO_3$ (calcium carbonate), and $MnO_2$ (manganese oxide). Lanthanum oxide was preliminarily sintered at 1200°C for 2 h, calcium carbonate was baked at 500°C for 3 h, and manganese oxide, at 750°C for 24 h. The latter process involved the transition from $MnO_2$ to $Mn_2O_3$. A mixture of the oxides was taken in the necessary stoichiometric proportion and ground in an agate mortar with ethyl alcohol. The mixture was annealed in four steps with intermediate grinding with ethyl alcohol every 20 h: the first stage was annealing at 850°C for 20 h; the second stage, at 950°C for 20 h; the third stage, at 1100°C for 100 h; and the fourth stage, at 1200°C for 200 h. Then, the sample was quenched in cooling to room temperature.

The neutron diffraction studies were carried out with a DN-12 spectrometer [8] of an IBR-2 pulsed high-flux reactor (the Frank Laboratory of Neutron Physics, Dubna) by using high-pressure cells with sapphire anvils [9] under external pressures up to 4.5 GPa in the temperature range from 10 to 300 K. The diffraction spectra were measured for scattering angles $2\theta = 90°$ and 45.5°. For these scattering angles, the resolution of the spectrometer at the wavelength $\lambda = 2$ Å was $\Delta d/d = 0.02$ and 0.025, respectively. The characteristic time of a single spectrum measurement was 20 h. The volume of the sample was $V \sim 2.5$ mm³. The pressure in the chamber was measured by the ruby luminescence line shift with an accuracy of 0.05 GPa. The pressure on the sample was obtained by averaging over the pressure values determined at several points of the sample surface. The pressure gradient along the sample surface did not exceed 15%. To carry out measurements with a high-pressure cell at low temperatures, we used a special-purpose cryostat made on the basis of a closed-cycle helium fridge. The diffraction data were analyzed by the Rietveld method with the use of the MRIA [10] (crystal structure) and FullProf [11] (magnetic structure) programs.

## RESULTS AND DISCUSSION

Parts of diffraction spectra obtained for $La_{0.75}Ca_{0.25}MnO_3$ under different pressures and at different temperatures are shown in Fig. 1. In the whole range of pressures 0–4.5 GPa and temperatures 12–295 K under study, the atomic structure of the compound retains its initial orthorhombic symmetry of the *Pnma* space group. The structural parameters of $La_{0.75}Ca_{0.25}MnO_3$ calculated from the diffraction data under different pressures are presented in the table. Their values at normal conditions agree well with the results of previous studies [12].

At normal pressure and $T < T_C = 240$ K, we observed the appearance of a magnetic contribution to the intensity of nuclear reflections: (101)/(020) at $d_{hkl} \approx 3.88$ Å and (200)/(002)/(121) at $d_{hkl} \approx 2.75$ Å (Fig. 1). This testifies to the appearance of the ferromagnetic state. The magnetic moments of Mn lie in the (*ac*) plane, and their calculated value of $3.29(5)\mu_B$ at $T = 12$ K is close to the value obtained in [12].

At $P = 1.5$ GPa, as the temperature decreased to $T < T_N \approx 150$ K, new magnetic reflections appeared at $d_{hkl} \approx 7.47$ Å and 3.44 Å (Fig. 1). The analysis of diffraction data showed that these reflections correspond to the appearance of the antiferromagnetic state with the A-type structure [1] and the propagation vector $q = (0\ 1\ 0)$. In such an antiferromagnetic structure, the magnetic moments of Mn lie in the (*ac*) planes; they are oriented parallel to each other within these planes and change to the opposite direction in the neighboring planes perpendicular to the *b* axis of the orthorhombic structure. As the pressure increased, an increase in the intensity of the antiferromagnetic reflections was observed along with a decrease in the ferromagnetic contribution to the

Structure parameters of $La_{0.75}Ca_{0.25}MnO_3$ at various pressures and $T = 295$ K. The La/Ca and O1 atoms are in the positions $4(c)(x, 1/4, z)$; Mn atoms, in $4(b)(0, 0, 1/2)$; and O2, in $8(d)(x, y, z)$ of the *Pnma* space group. The effective magnetic moments of the Mn ions are presented for the ferromagnetic and antiferromagnetic phases at $T = 12$ K

| $P$ (GPa) | 0 | 1.5 | 4.5 |
|---|---|---|---|
| $a$ (Å) | 5.481(6) | 5.467(7) | 5.429(4) |
| $b$ (Å) | 7.747(5) | 7.735(9) | 7.687(9) |
| $c$ (Å) | 5.494(4) | 5.483(4) | 5.482(6) |
| La/Ca: $x$ | 0.021(5) | 0.023(7) | 0.026(6) |
| $z$ | −0.003(5) | −0.002(7) | −0.002(9) |
| O1: $x$ | 0.492(3) | 0.496(5) | 0.498(7) |
| $z$ | 0.064(7) | 0.059(7) | 0.063(8) |
| O2: $x$ | 0.276(8) | 0.277(8) | 0.269(9) |
| $y$ | 0.033(4) | 0.032(5) | 0.029(7) |
| $z$ | 0.723(6) | 0.722(8) | 0.731(9) |
| $M_{FM}$ ($\mu_B$) | 3.29(5) | 3.0(1) | 2.6(1) |
| $M_{AFM}$ ($\mu_B$) | – | 1.1(1) | 1.7(1) |
| $R_p$ (%) | 7.05 | 8.91 | 8.28 |
| $R_{wp}$ (%) | 6.30 | 7.52 | 8.24 |

nuclear reflections. This testifies to an increase in the volume fraction of the antiferromagnetic phase. The volume fractions of the ferromagnetic and antiferromagnetic phases were calculated from the effective values of magnetic moments at $T = 12$ K (see table) and proved to be 88 and 12%, respectively, at $P = 1.5$ GPa, 70 and 30%, respectively, at $P = 4.5$ GPa.

The $La_{0.75}Ca_{0.25}MnO_3$ crystal structure is an orthorhombically distorted modification of a perfect cubic perovskite structure with parameters $a \approx c \approx a_p\sqrt{2}$ and $b \approx 2a_p$. Because of the broadening of diffraction peaks and the presence of a pressure gradient in the sample volume, the refinement of structural parameters by the Rietveld method showed a strong correlation between the unit cell parameters. Therefore, their ratio $a : b : c$ was calculated for different pressures on the basis of pressure dependences [7] determined with a higher resolution by the X-ray diffraction method and was fixed. The resulting pressure dependences of the parameters and volume of the unit cell are almost linear (Fig. 2). The calculated linear compressibilities $k_i = -(1/a_{i0})(da_i/dP)_T$ (where $a_i = a, b, c$) of the unit cell parameters at $T = 295$ K are as follows: $k_a = 0.0017$, $k_b = 0.0020$, and $k_c = 0.0014$ GPa$^{-1}$, which is close to the values obtained in [7].

The $MnO_6$ oxygen octahedra contain three pairs of nonequivalent Mn–O bonds: Mn–O1 directed along the $b$ axis and Mn–O2a and Mn–O2b lying in the ($ac$)
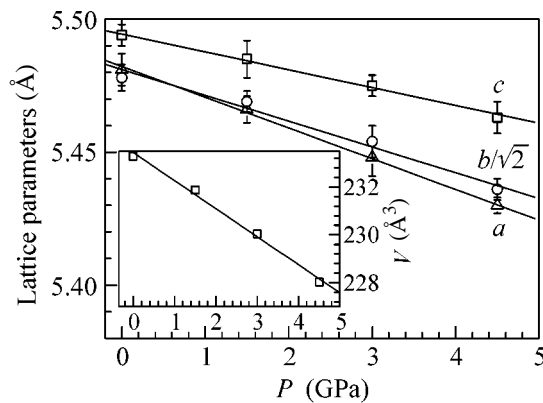


**Fig. 2.** Pressure dependences of the unit cell parameters of $La_{0.75}Ca_{0.25}MnO_3$ and their linear interpolation. The inset shows the pressure dependence of the unit cell volume of $La_{0.75}Ca_{0.25}MnO_3$.
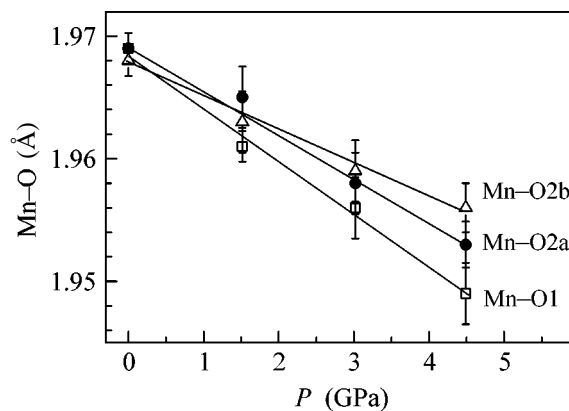


**Fig. 3.** Pressure dependences of the Mn–O bond lengths in $La_{0.75}Ca_{0.25}MnO_3$ and their linear interpolation.
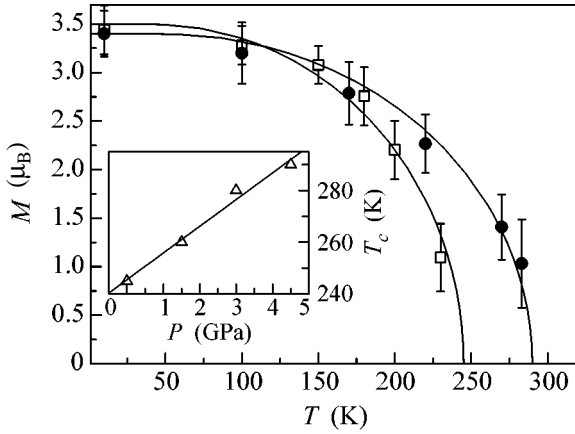
**Fig. 4.** Temperature dependences of the effective magnetic moment of the Mn ferromagnetic phase for $P$ = (open points) 0 and (closed points) 4.5 GPa and their interpolation by function (1). The inset shows the pressure dependence of the Curie temperature and its linear interpolation.

plane. As the pressure grows, the Mn–O bonds are anisotropically compressed (Fig. 3), which leads to a uniaxial compression of the oxygen octahedra along the $b$ axis. The coefficient of linear compressibility of bond lengths $k_i = -(1/l_{Mn–Oi0})(dl_{Mn–Oi}/dP)_T$ ($i$ = 1, 2a, 2b) at $T$ = 295 K is maximum for the Mn–O1 bond: $k_1$ = 0.0020 GPa$^{-1}$; the corresponding values for the Mn–O2a and Mn–O2b bonds are somewhat smaller: $k_{2a}$ = 0.0017 and $k_{2b}$ = 0.0015 GPa$^{-1}$. An increase in pressure from 0 to 4.5 GPa is accompanied by an increase in the valence angles of the MnO$_6$ oxygen octahedra: the Mn–O1–Mn angle increases from 159.2° to 160.50° and the Mn–O2–Mn angle, from 160.58° to 161.80°.

To determine the pressure dependence of the Curie temperature, the temperature dependences of the effective magnetic moment of the ferromagnetic phase measured at different pressures were interpolated by the function describing the temperature dependence of the magnetic moment of the ferromagnet in the molecular field approximation [13]:

$$\frac{M}{M_0} = B_S\left(\frac{3S}{S+1}\frac{M}{M_0}\frac{T_C}{T}\right), \qquad (1)$$

where $B_S$ is the Brillouin function, $S$ is the Mn ion spin ($S$ = 3/2), and $M_0$ is the magnetic moment at $T$ = 0. As the pressure increases, an almost linear increase in $T_C$ is observed with $dT_C/dP \approx$ 12 K/GPa (Fig. 4). This value is close to that calculated from the data given in [5] for the same pressure range: $dT_{IM}/dP \approx$ 15 K/GPa.

In the framework of the double exchange model, the magnetic and transport properties of manganites are determined by the charge carrier bandwidth $W$ and, in the approximation of a strong interatomic exchange interaction ($J_H \gg W$), we have $T_C \approx T_{IM} \propto W$ [14]. In the absence of the Jahn–Teller distortions of oxygen octa-

hedra, the charge carrier bandwidth is determined by the transfer integral of $e_g$ electrons in the Mn$^{3+}$–O$^{2-}$–Mn$^{4+}$ chains and depends on the mean Mn–O bond length $l$ and the Mn–O–Mn angle $\phi$ as $W = W_0 \sim \cos^2\phi/l^{3.5}$ [15, 16]. The calculated increase in the bandwidth that is only related to the variation of structure parameters in the high-pressure range 0–4.5 GPa is about 4%. This value corresponds to $(dT_C/dP)_0 \approx$ 2 K/GPa, which is much smaller than the experimental value. The presence of static cooperative Jahn–Teller distortions of oxygen octahedra leads to the formation of polarons and to an effective bandwidth variation [17]

$$W \sim W_0\exp(-\gamma E_{JT}/\hbar\omega). \qquad (2)$$

Here, $E_{JT}$ is the polaron bond energy, $\omega$ is the characteristic frequency of phonon modes corresponding to the oscillations of oxygen octahedra, and $0 < \gamma < 1$ is a parameter characterizing the strength of the electron–phonon coupling. To estimate the quantity $dT_C/dP$, we use the temperature dependences of electrical resistance $R$ of La$_{0.75}$Ca$_{0.25}$MnO$_3$ under different pressures [7]. These dependences allow us to calculate the activation energy $E_a \approx \frac{1}{2}E_{JT}$ [18] by using the expression $R = R_0T\exp(E_a/kT)$ and the pressure dependence of the frequency of the $B_{2g}(1)$ mode of oxygen octahedra oscillation from [6]. As the pressure increases from 0 to ~5 GPa, $E_{JT}$ decreases from 92 to 69 meV while $\hbar\omega_{B2g(1)}$ increases from 78 to 82 meV. Assuming that $\gamma$ = 1, from Eq. (2) we obtain the value $(dT_C/dP)_{calc} \approx$ 18 K/GPa, which is close to the experimental value $dT_C/dP \approx$ 12 K/GPa. To estimate $dT_C/dP$ with better accuracy, additional assumptions concerning the pressure behavior of the parameter $\gamma$ are necessary.

The appearance of the A-type antiferromagnetic phase in La$_{0.75}$Ca$_{0.25}$MnO$_3$ under high pressures is possibly caused by the uniaxial anisotropic compression of the oxygen octahedra along the $b$ axis of the orthorhombic structure. According to recent theoretical [19] and experimental [20] studies, the magnetic properties of manganites strongly depend on the magnitude of the pseudo-tetragonal distortion of oxygen octahedra. For La$_{0.75}$Ca$_{0.25}$MnO$_3$, this distortion can be estimated as $t \approx l_{Mn–O1}/l_{\langle Mn–O2\rangle} = 0.997$ at $P$ = 4.5 GPa and $T$ = 295 K. In the case of the pseudo-tetragonal distortion $t < 1$, a predominant filling of the $d(x^2 - z^2)e_g$ orbitals of Mn ions takes place along with a decrease in the exchange integral between the closest neighbors in the direction of uniaxial compression. These factors form favorable conditions for the formation of the antiferromagnetic state of A type [19]. The appearance of the A-type antiferromagnetic phase is accompanied by an additional uniaxial compression of the crystal lattice, which, in orthorhombic manganites with a *Pnma*-symmetry structure, usually manifests itself as a noticeable decrease in the parameter $b$ of the unit cell and some

slight increases in the parameters $a$ and $c$. From the analysis of the positions of the characteristic magnetic reflections (010) and (111), we obtain the estimates $a \approx c \approx 5.48$ Å and $b \approx 7.45$ Å for the A-type antiferromagnetic structure at $P = 4.5$ GPa and $T = 12$ K. These values are comparable with the unit cell parameters for $Nd_{1-x}Sr_xMnO_3$ manganites, in which the A-type antiferromagnetic phase was observed at normal pressure and low temperatures for $0.5 < x < 0.6$ [21].

The ferromagnetic metallic phase and the A-type antiferromagnetic phase of doped manganites at normal pressure have noticeably different transport properties and types of distortion of the oxygen octahedra [21, 22]. Therefore, the appearance of the A-type antiferromagnetic phase at high pressures may be a possible reason for the anomalous behavior of the pressure dependences of both the insulator–metal transition temperature $T_{IM}$ [5] and the frequency of the oxygen octahedron oscillation mode $\omega_{B_{2g}(1)}$ [6] in $La_{0.75}Ca_{0.25}MnO_3$.

## CONCLUSIONS

The results of this study show that the effect of high external pressure leads to the appearance of the A-type antiferromagnetic state in $La_{0.75}Ca_{0.25}MnO_3$ manganite and to a suppression of the initial ferromagnetic state, whose volume fraction decreases with growing pressure. A possible reason for this phenomenon may be the uniaxial anisotropic compression of the $MnO_6$ oxygen octahedra, which leads to a predominant filling of the $d(x^2 - z^2)e_g$ orbitals of Mn ions. The considerable increase in the Curie temperature of transition to the ferromagnetic state, which is observed in the experiment, may be explained in terms of the double exchange model with allowance for the electron–phonon coupling. This model yields adequate computational estimates of $T_C$ on the basis of experimental data.

## REFERENCES

1. E. Dagotto, T. Hotta, and A. Moreo, Phys. Rep. **344**, 1 (2001).
2. C. Zener, Phys. Rev. **82**, 403 (1951).
3. P. W. Anderson and H. Hasegawa, Phys. Rev. **100**, 675 (1955).
4. P.-G. De Gennes, Phys. Rev. **118**, 141 (1960).
5. P. Postorino, A. Congeduti, P. Dore, *et al.*, Phys. Rev. Lett. **91**, 175501 (2003).
6. A. Congeduti, P. Postorino, E. Caramagno, *et al.*, Phys. Rev. Lett. **86**, 1251 (2001).
7. C. Meneghini, D. Levy, S. Mobilio, *et al.*, Phys. Rev. B **65**, 012111 (2001).
8. V. L. Aksenov, A. M. Balagurov, V. P. Glazkov, *et al.*, Physica B (Amsterdam) **265**, 258 (1999).
9. V. P. Glazkov and I. N. Goncharenko, Fiz. Tekh. Vys. Davleniĭ **1**, 56 (1991).
10. V. B. Zlokazov and V. V. Chernyshev, J. Appl. Crystallogr. **25**, 447 (1992).
11. J. Rodriguez-Carvajal, Physica B (Amsterdam) **192**, 55 (1993).
12. P. G. Radaelli, G. Iannone, M. Marezio, *et al.*, Phys. Rev. B **56**, 8265 (1997).
13. A. B. Beznosov, V. A. Desnenko, E. L. Fertman, *et al.*, Phys. Rev. B **68**, 054109 (2003).
14. N. Furukawa, in *Physics of Manganites*, Ed. by T. A. Kaplan and S. D. Mahanti (Kluwer Academic/Plenum, New York, 1999), p. 1; N. Furukawa, cond-mat/9812066.
15. W. A. Harrison, *Electronic Structure and the Properties of Solids: The Physics of the Chemical Bond* (Freeman, San Francisco, 1980; Mir, Moscow, 1983).
16. V. Laukhin, J. Fontcuberta, J. L. Garcia-Munoz, *et al.*, Phys. Rev. B **56**, R10 009 (1997).
17. J. Fontcuberta, V. Laukhin, and X. Obradors, Phys. Rev. B **60**, 6266 (1999).
18. D. P. Kozlenko and B. N. Savenko, J. Phys.: Condens. Matter **16**, 9031 (2004).
19. Z. Fang, I. V. Solovyev, and K. Terakura, Phys. Rev. Lett. **84**, 3169 (2000).
20. Y. Konishi *et al.*, J. Phys. Soc. Jpn. **68**, 3790 (1999).
21. R. Kajimoto, H. Yoshizawa, H. Kawano, *et al.*, Phys. Rev. B **60**, 9506 (1999).
22. J. Hejtmánek, J. Pollert, E. Jirák, *et al.*, Phys. Rev. B **66**, 014426 (1999).

*Translated by E. Golyamina*

# Phase Transition in the Generalized
# Ising–Kosterlitz–Thouless Model

## P. A. Prudkovskiĭ

*Faculty of Physics, Moscow State University, Vorob'evy gory, Moscow, 119992 Russia*
*e-mail: pasha@qopt.phys.msu.su*
Received August 17, 2005

The features of the phase transition are considered in a model that is a combination of the Ising and Kosterlitz–Thouless models. It is shown that one or two successive phase transitions may occur in such a system, depending on the relation between parameters. An asymptotic formula is derived for the Ising-type phase transition temperature. © 2005 Pleiades Publishing, Inc.

PACS numbers: 77.80.Bh

The construction of the theory of renormalization group transformations by Wilson [1] has considerably extended the class of systems whose critical behavior can be described analytically. One such system is the 2D *XY* model, for which the features of phase transition were considered by Kosterlitz and Thouless [2, 3] just two years after the publication [1]. The Kosterlitz–Thouless model occupies a special place among systems exhibiting a second-order phase transition, since the long-range order in such a system exists only at zero temperature; at other temperatures (even below the Curie point), the phase correlator decreases with increasing distance [4]. The phase transition point can be detected from a sharp change in the correlation function decay law; however, this is a nontrivial problem from the experimental point of view (in particular, in the case of a numerical experiment [5–7]). For this reason, it is especially interesting to analyze the behavior of a system, in which an ordinary second-order phase transition may occur simultaneously with a phase transition following the Kosterlitz–Thouless scenario.

The system considered here emerges in the course of evolution of the model describing the formation of domain structures in KDP crystals [8]; however, this system is interesting in itself as an example of interaction between two phase transitions of different origins.

Let us consider a system whose energy is defined by the effective Hamiltonian

$$
\begin{aligned}
H_{\text{eff}}^{(1)} &= \frac{1}{2}\sum_{ij}[a(1 - s_{ij}s_{i+1j}) \\
&+ (1 + s_{ij}s_{i+1j})\{1 - \cos(\varphi_{ij} - \varphi_{i+1j})\}] \\
&+ \frac{1}{2}\sum_{ij}[a(1 - s_{ij}s_{ij+1}) \\
&+ (1 + s_{ij}s_{ij+1})\{1 - \cos(\varphi_{ij} - \varphi_{ij+1})\}],
\end{aligned}
\tag{1}
$$

where summation is carried out over all sites of the square lattice and "spin" $s_{ij} = \pm 1$ and "phase" $|\varphi_{ij}| \leq \pi$ are defined at each site $ij$. In other words, the interaction between phases $\varphi_{ij}$ takes place only when spins $s_{ij}$ coincide. Energy (1) of the system can be conditionally represented in the form of a deep two-well potential with a compass needle located at the bottom of one of the wells; the needles at adjacent sites interact only if they are located in identical wells (Fig. 1). Such a model is a combination of the Ising and the Kosterlitz–Thouless models [2, 3]; in the special case when $s_{ij} = $ const, the model is transformed into the classical *XY* model, while for $\varphi_{ij} = $ const it is transformed into the Ising model, in which the phase transition temperature is determined by the constant $a$ of spin interactions [9]:

$$
T_I = a/\ln(\sqrt{2} + 1).
\tag{2}
$$

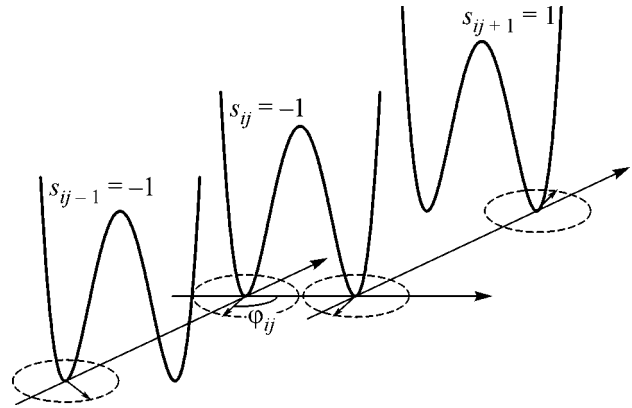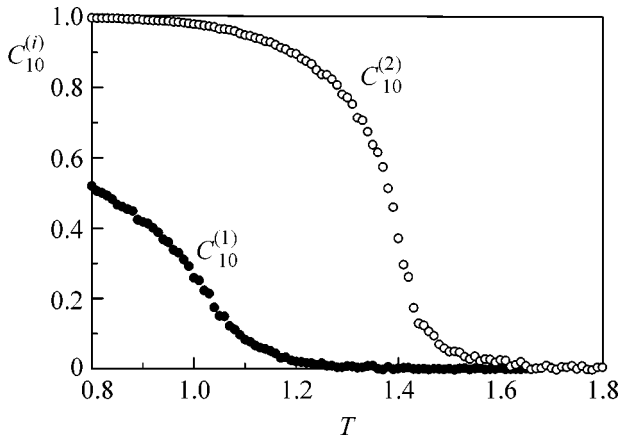The ground state of the system is a homogeneous state with constant values of spins and phases, which



**Fig. 1.** Schematic representation of effective potential (1).

**Fig. 2.** Temperature dependences of the tenth component of the "spin" and "phase" correlation functions given by Eqs. (7) for parameter $a = 2$, which make it possible to determine the phase transition temperatures of the Ising ($T_C = 1.49 \pm 0.04$) and Kosterlitz–Thouless ($T_{KT} = 1.19 \pm 0.04$) types in model (1).



**Fig. 3.** Temperature dependence of the average binding energy $F(T)$ given by Eq. (5) in the XY model: points are the results of numerical experiment and the solid curve is the approximation by formula (9) (with the parameters are given in the figure).

takes place at zero temperature. At a high temperature, the system passes to a completely chaotic state; the long-range order may be disturbed after one or two phase transitions depending on the relation of the critical temperatures in the Ising model (2) and in the XY model. Indeed, let us consider the decay of a homogeneous state upon a slow increase in temperature. As mentioned above, a peculiar feature of the phase transition in the 2D XY model is that no regular long-range order exists at any nonzero temperature and the correlation function decreases in accordance with the polynomial law with a temperature-dependent exponent [2–4]:

$$\langle \varphi_{ij}\varphi_{ij+k} \rangle \sim k^{-T/4\pi}. \tag{3}$$

Consequently, the state of system (1), which is homogeneous in spins $s_{ij}$, can be treated as a certain "phase" liquid whose internal energy increases with temperature. If we disregard the correlation between the spins and phases and average Hamiltonian (1) over phase variables, we find that the effective constant of spin interaction is a function of temperature,

$$H_{\text{eff}}^{(2)} = -\frac{1}{2}\sum_{ij}\{a+1-F(T)\}(s_{ij}+s_{i+1j}+s_{ij}s_{ij+1}), \tag{4}$$
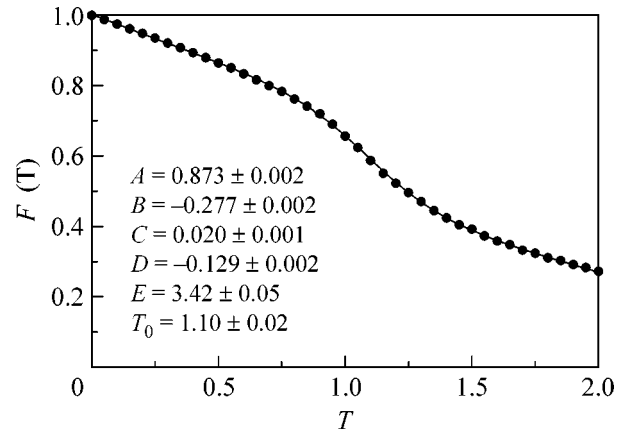
where $F(T)$ is the mean value of the binding energy in the Kosterlitz–Thouless model:

$$F(T) = \langle \cos(\varphi_{ij}-\varphi_{ij+1}) \rangle. \tag{5}$$

Thus, it turns out that an Ising-type transition occurs in system (1) at the temperature satisfying the equation

$$T_C = \{a+1-F(T_C)\}/\ln(\sqrt{2}+1). \tag{6}$$

If this temperature is higher than the Curie point $T_C > T_{KT}$ in the XY model, two phase transitions successively

occur in the system. For $T_C < T_{KT}$, only an Ising-type transition occurs in the system, since the rupture of coupling between spins immediately triggers an interaction between phases.

To verify the above scenario, a series of numerical experiments were performed, which made it possible to determine the dependence of the phase transition temperature $T_C$ on quantity $a$. Simulation was carried out on a $400 \times 400$ mesh by the Monte Carlo method using the Metropolis algorithm. The temperatures of phase transitions of the Ising and Kosterlitz–Thouless types were determined from the behavior of the *spin* and *phase* correlation functions (Fig. 2)

$$\begin{aligned} C_k^{(1)} &= \langle s_{ij}s_{ij+k} \rangle, \\ C_k^{(2)} &= \langle (s_{ij}s_{ij+k}+1)\cos(\varphi_{ij}-\varphi_{ij+k}) \rangle. \end{aligned} \tag{7}$$

Analogously, the $F(T)$ dependence was determined as a result of simulation of evolution of the conventional XY model with the effective Hamiltonian

$$H_{\text{eff}}^{(3)} = -\frac{1}{2}\sum_{ij}\{\cos(\varphi_j-\varphi_{i+1j})+\cos(\varphi_{ij}-\varphi_{ij+1})\}. \tag{8}$$

It turns out that this dependence is correctly approximated by the formula

$$F(T) \approx A + BT + CT^2 + D\tanh\{E(T-T_0)\}. \tag{9}$$

This is illustrated in Fig. 3, where $T_0 \approx T_{KT}$ is the approximate phase transition temperature.

Figure 4 shows the $T_C(a)$ dependences obtained as a result of the numerical experiment and from the solution of Eq. (6) taking into account approximation (9). The theoretical curve based on Eq. (6) correctly describes the results of numerical experiment for small
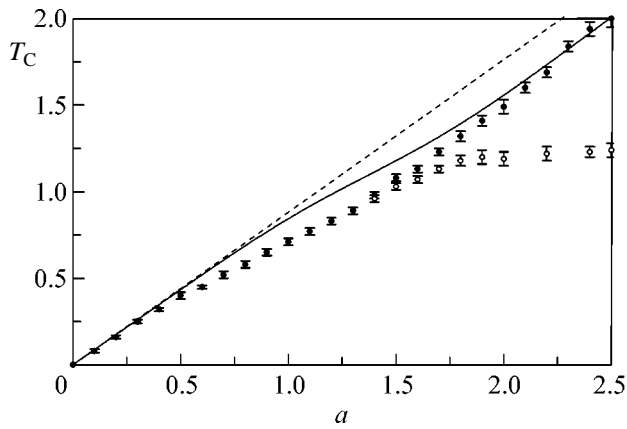
**Fig. 4.** Dependence of the phase-transition temperature on a in the generalized Ising–Kosterlitz–Thouless model. The closed points represent the results of numerical experiment, the solid curve describes theoretical dependence (6), and the dashed curve is the dependence of the phase-transition temperature on the interaction constant $a$ in the Ising model specified by Eq. (2). The open circles correspond to the phase-transition temperature in the Kosterlitz–Thouless model.

as well as for large values of $a$. However, the matching is much worse in the region of the triple point, at which the $T_C(a)$ dependence intersects the additional branch corresponding to a phase transition of the Kosterlitz–Thouless type. This is not surprising, since fluctuations of spin and phase variables in this region are strongly correlated and the averaging carried out in expression (4) is incorrect. The position of the triple point on the phase diagram is approximately determined by the value of $a$

for which $T_C(a) \approx T_{KT}$; however, the refinement of the position of this point requires precise measurement of the Curie temperature in the *XY* model from an analysis of critical dependences [5–7]. Apparently, the nature of the phase transition in the vicinity of the triple point is an individual interesting problem.

## REFERENCES

1. K. J. Wilson, Usp. Fiz. Nauk **141**, 193 (1983).
2. J. M. Kosterlitz and D. J. Thouless, J. Phys. C: Solid State Phys. **6**, 1181 (1973).
3. D. J. Thouless, J. Phys. C: Solid State Phys. **7**, 1046 (1974).
4. V. L. Berezinskiĭ, Zh. Éksp. Teor. Fiz. **59**, 907 (1970) [Sov. Phys. JETP **32**, 493 (1970)].
5. R. Gupta and C. F. Baillie, Phys. Rev. B **45**, 2883 (1992).
6. P. Olsson, Phys. Rev. B **52**, 4526 (1995).
7. W. Janke, Phys. Rev. B **55**, 3580 (1997).
8. A. A. Zhukov and P. A. Prudkovskiĭ, Vestn. Mosk. Univ., Ser. Fiz. **4**, 55 (2002).
9. L. D. Landau and E. M. Lifshitz, *Course of Theoretical Physics*, Vol. 5: *Statistical Physics*, 3rd ed. (Nauka, Moscow, 1976; Pergamon, Oxford, 1980), Part 1.

*Translated by N. Wadhwa*

# Spin-Dependent Recombination in GaAsN Solid Solutions

## V. K. Kalevich[a], E. L. Ivchenko[a], M. M. Afanasiev[a], A. Yu. Shiryaev[a], A. Yu. Egorov[a], V. M. Ustinov[a], B. Pal[b], and Y. Masumoto[b]

[a] *Ioffe Physicotechnical Institute, Russian Academy of Sciences, Politekhnicheskaya ul. 26, St. Petersburg, 194021 Russia*
*e-mail: kalevich@solid.ioffe.ru*
[b] *Institute of Physics, University of Tsukuba, Tsukuba 305-8571, Japan*
Received August 8, 2004; in final form, August 29, 2005

Room-temperature spin-dependent recombination in a series of $GaAs_{1-x}N_x$ solid solutions ($x = 2.1, 2.7, 3.4\%$) has been observed as manifested by a more than threefold decrease in intensity of the edge photoluminescence upon switching from circular to linear polarization of the exciting light or upon the application of a transverse magnetic field (~300 G). The interband absorption of the circularly polarized light is accompanied by the spin polarization of conduction electrons, which reaches 35% with an increase in the pumping level. The observed effects are explained in terms of the dynamic polarization of deep paramagnetic centers and the spin-dependent trapping of conduction electrons on these centers. The electron spin relaxation time, as estimated from the dependence of the edge photoluminescence depolarization in the transverse magnetic field (the Hanle effect) on the pumping intensity, is on the order of 1 ns. According to the adopted theory, the electron spin relaxation time in the presence of spin-dependent recombination is determined by a slow spin relaxation of localized electrons. The sign (positive) of the $g$ factor of localized electrons has been experimentally determined from the direction of the magnetic-field-induced rotation of their average spin observed in the three GaAsN crystals studied. © 2005 Pleiades Publishing, Inc.

PACS numbers: 71.20.Nr, 72.25.Fe, 78.55.Cr

In recent years, solid solutions of the Ga(In)AsN systems have received much attention due to their unusual properties and good prospects for use in optoelectronic devices for the near-IR spectral range. The interaction of the localized states of nitrogen atoms with the intrinsic electron states in the conduction band leads to an anomalous decrease in the bandgap width for compositions with low (several percent) nitrogen content [1, 2]. Since Ga(In)AsN solid solutions exhibit a complicated energy band structure, elucidation of the mechanisms involved in the energy relaxation and the recombination in these materials is important both from the standpoint of basic science and for the development of optoelectronic devices.

This paper reports on the phenomenon of spin-dependent recombination (SDR) in single crystals of GaAsN solid solutions at room temperature, which was manifested by a sharp decrease in intensity of the edge photoluminescence from the samples upon the switching from circular to linear polarization of the exciting light or upon the application of a transverse magnetic field (~300 G). In addition, the SDR at room temperature is manifested by a giant (~35%) spin polarization and by a spin memory (~1 ns) of the conduction electrons, which are observed upon the interband absorption of circularly polarized light. We have studied nitrogen-containing solid solutions of the $GaAs_{1-x}N_x$ system obtained in the form of undoped 0.1-μm-thick films grown by molecular beam epitaxy between GaAs

layers on semi-insulating (001)-oriented GaAs substrates [3]. The as-grown structures were annealed for 5 min at 700°C in a flow of arsenic in the growth chamber. The investigation was performed on three samples with different nitrogen contents $x = 2.1, 2.7$, and 3.4%.

Spin polarization of the conduction electrons, which was observed upon the interband absorption of circularly polarized light [4], was evaluated by measuring the degree of the circular polarization of photoluminescence, defined as $\rho = (I^+ - I^-)/(I^+ + I^-)$, where $I^+$ and $I^-$ are the intensities of the clockwise ($\sigma^+$) and anticlockwise ($\sigma^-$) polarized photoluminescence components. The values of $\rho$ and the total photoluminescence intensity $I = I^+ + I^-$ in a wavelength range up to 1.4 μm were determined using a high-sensitivity polarization analyzer [5] comprising a quartz polarization modulator, a lock-in two-channel photon counter, and a photomultiplier with an InGaAsP photocathode. The luminescence was excited by Ti:sapphire laser radiation incident along the normal to the sample surface. The photoluminescence was measured in the reflection mode along the structure growth axis. The measurements were performed at 300 K. Since the main experimental results were qualitatively the same for all samples, the data will be presented mostly for the $GaAs_{1-x}N_x$ solid solution with $x = 2.1\%$.

The typical spectral dependences of the intensity and the degree of circular polarization for the photoluminescence of a $GaAs_{0.979}N_{0.021}$ sample excited by cir-
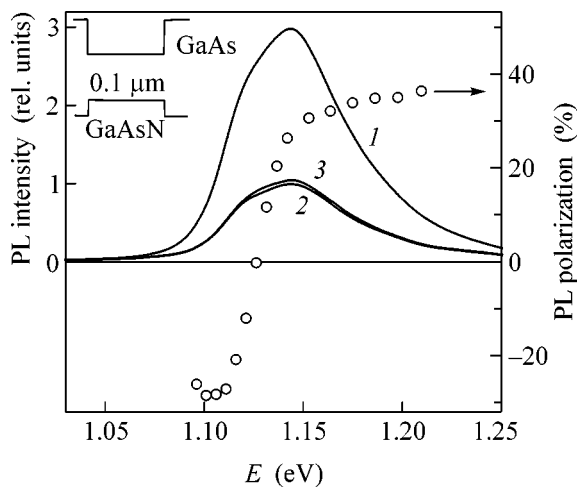
**Fig. 1.** Photoluminescence spectra of a $GaAs_{0.979}N_{0.021}$ film excited by the (*1*, *3*) circularly and (*2*) linearly polarized light; spectrum *3* was measured in the presence of a transverse magnetic field (300 G). Open circles show the degree of circular polarization of the photoluminescence. All spectra were measured at $T = 300$ K using the exciting light with $h\nu_{exc} = 1.305$ eV and $J = 150$ mW. The inset shows a schematic diagram of the sample structure.

cularly ($\sigma^+$ or $\sigma^-$) polarized light of sufficiently high intensity are presented in Fig. 1. An increase in the nitrogen content (in the samples with $x = 2.7$ and $3.4\%$) was accompanied by a shift of the photoluminescence band toward longer wavelengths. The observed photoluminescence spectrum is a superposition of two strongly overlapping bands, the relative shift of which increases with $x$ to reach 50 meV at $x = 3.4\%$ [3]. The low-energy photoluminescence component has a negative polarization (relative to that of the exciting beam), whereas the high-energy photoluminescence component has a positive polarization. Recently, we explained [3, 6] the presence of two photoluminescence components with the opposite signs of polarization in terms of the splitting of light- and heavy-hole subbands caused by the elastic straining of the GaAsN layer. Indeed, a smaller lattice parameter of GaAsN as compared to that of GaAs leads to an extension of the GaAsN layer in the interface plane, which is equivalent to a uniaxial compression of this layer along the growth axis. This uniaxial straining is accompanied by the splitting of light- and heavy-hole subbands, which increases with the nitrogen content ($x$). The polarization spectrum presented in Fig. 1 was measured with the simultaneous excitation of electrons in both valence subbands. In order to exclude the excitation of electrons in GaAs layers (playing the role of barriers with respect to GaAsN), the energy of exciting light quanta was selected below the bandgap width of GaAs. Therefore, the negative polarization of the low-energy photoluminescence component and the positive polarization of the high-

energy photoluminescence component are indicative of the fact that these bands are due to the recombination of electrons with light and heavy holes, respectively.

Figure 1 also shows the photoluminescence spectrum (curve *2*) of a sample excited by linearly ($\pi$) polarized light. The comparison of curves *1* and *2* shows that the switching from circular to linear polarization of the exciting light leads to a decrease in the photoluminescence intensity $I$ (by a factor of about 3 at the photoluminescence peak). Approximately the same decrease in $I$ was observed upon the application of a magnetic field (Fig. 1, curve *3*) with a strength of ~300 G, which was oriented perpendicularly to the direction of excitation (i.e., with the field vector occurring in the film plane). It should be noted that the change in the $I$ value observed upon the circular polarization switching from $\sigma^+$ to $\sigma^-$ was negligibly small as compared to the aforementioned effect.

Figure 2a shows the photoluminescence depolarization curves $\rho(B)$ for the $GaAs_{0.979}N_{0.021}$ film measured in a transverse magnetic field $\mathbf{B} \perp [001]$ for the heavy-hole photoluminescence subband excited at various intensities of the circularly ($\sigma$) polarized light. These dependences can be approximated by Lorentzian profiles (solid curves in Fig. 2a) of the type

$$\rho(B) = \rho^* + \frac{\rho_0}{1 + (B/B_{1/2})^2}, \qquad (1)$$

where $\rho^*$ is a constant component ($\approx 5\%$), $B_{1/2}$ is the FWHM (halfwidth) of the curve, and $\rho_0$ is the maximum field-induced change in $\rho$. The values of $B_{1/2}$ and $\rho_0$ are strongly dependent on the intensity $J$ of the circularly polarized exciting light. At the same time, the results of additional measurements showed that the width of the $\rho(B)$ curves measured using the same excitation intensity for the positive ($c$–$hh$ transition) and negative ($c$–$lh$ transition) photoluminescence polarizations were the same. This is evidence for the assumption that the polarization of holes is absent because of their rapid spin relaxation and, hence, the photoluminescence polarization is entirely due to the spin polarization of electrons.

Figure 2b shows the field dependences of the photoluminescence intensity $I(B)$, which are also well described by Lorentzian profiles (solid curves). The widths of these profiles coincide with those of the $\rho(B)$ curves obtained for the same excitation intensity.

The experimental results presented in Figs. 1 and 2 can be explained within the framework of the SDR theory formulated by Weisbuch and Lampel [7] in application to $Ga_{0.6}Al_{0.4}As$ solid solutions. This theory was successfully used [8, 9] for the analysis of recombination processes in GaAs and in GaAs/AlGaAs superlattices. According to this theory, each paramagnetic center can trap either one electron with uncompensated spin $\pm 1/2$ or two electrons in a singlet state with zero

total spin. In the case of normal excitation with circularly polarized light in the absence of a magnetic field, the electron spins are polarized in the direction of excitation ($z$ axis). Let $n_\pm$ and $N_\pm$ denote the densities of free electrons and paramagnetic centers with the electron spin projection $\pm1/2$ respectively, and let $N_{\uparrow\downarrow}$ be the concentration of paramagnetic centers with two electrons. In the SDR model under consideration, the contribution due to the interband recombination mechanism is ignored and the rate of the loss of free carriers via trapping on paramagnetic centers is described by the expressions $(dn_\pm/dt)_{rec} = -\gamma_e n_\pm N_\mp$ for electrons and $(dp/dt)_{rec} = -\gamma_h p N_{\uparrow\downarrow}$ for holes ($p$ is the density of holes, which are considered unpolarized, irrespective of the polarization of exciting light). In addition to the recombination constants $\gamma_e$ and $\gamma_h$, the system is characterized by the spin relaxation times of free ($\tau_s$) and coupled ($\tau_{sc}$) electrons. At room temperature, the latter relaxation constants obey the condition $\tau_s \ll \tau_{sc}$.

For a qualitative explanation of the observed behavior of the photoluminescence intensity and circular polarization as functions of the exciting light polarization and the external magnetic field, it is sufficient to consider the case of weak pumping, whereby the degree of spin polarization of coupled electrons ($P_c$) is relatively low [7, 9]:

$$I \propto 1 + aP_c P, \quad \rho = b(P_i + P_c). \quad (2)$$

Here, $P = (n_+ - n_-)/(n_+ + n_-)$ and $P_c = (N_+ - N_-)/(N_+ + N_-)$ are the degrees of spin polarization of the free and coupled electrons, respectively; $a$ and $b$ are positive coefficients; and $P_i$ is the initial degree of spin polarization of photoelectrons at the moment of their creation. Since linearly polarized exciting light does not produce optical orientation (i.e., polarization) of the electron spins, the ratio of photoluminescence intensities ($I_{circ}/I_{lin}$) for the optical pumping with circular and linear polarization is $1 + aP_c P$, where $P_c$ and $P$ refer to the circularly polarized exciting light. It should be noted that the product $P_c P$ is positive and independent of the sign of the circular polarization of exciting light, which implies that $I_{circ} > I_{lin}$.

In a transverse magnetic field ($\mathbf{B} \perp z$) such that $|g_e|\mu_B B\tau_s/\hbar \ll 1$, while the $|g_c|\mu_B B\tau_{sc}/\hbar$ is arbitrary ($g_e$ and $g_c$ are the $g$-factors of the free and coupled electron, respectively, and $\mu_B$ is the Bohr magneton), we may ignore the rotation of the spin of free electrons due to the Larmor precession. In this case, expressions (2) are also valid for $B \neq 0$, provided that $P_c$ is the degree of spin polarization of the coupled electrons along the $z$ axis: $P_c(B) = P_c(0)[1 + (\Omega_c T_{sc})^2]^{-1}$. Here, $\Omega_c = g_c\mu_B B/\hbar$, $T_{sc}^{-1} = \tau_{sc}^{-1} + \tau_c^{-1}$, and $\tau_c^{-1} = \gamma_h N_{\uparrow\downarrow}(p/N)$, since the depolarization of spins for the coupled electrons takes place both due to the spin relaxation (characterized by $\tau_{sc}$) and due to the trapping of holes (characterized by $\tau_c$) on
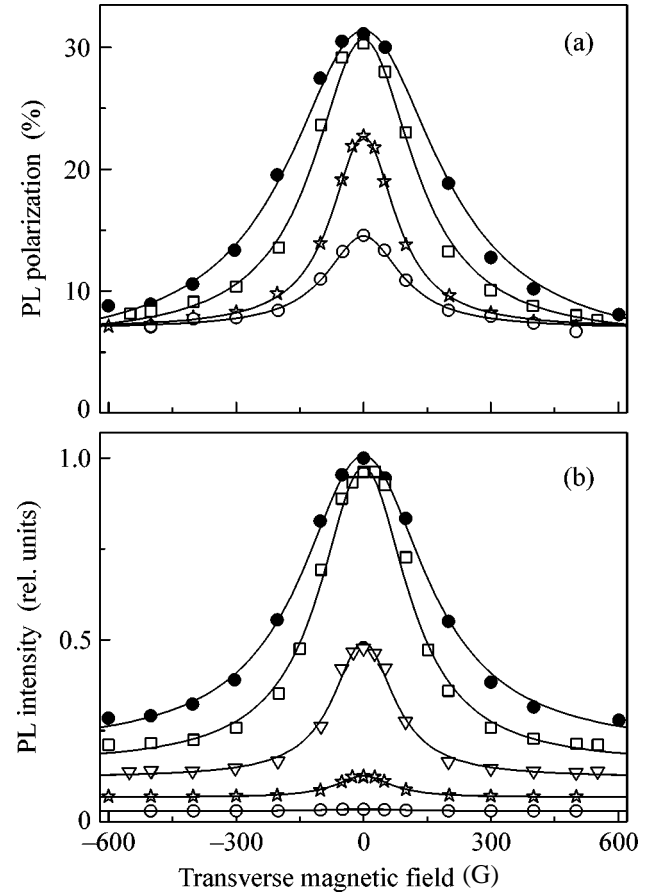


**Fig. 2.** (a) The degree of circular polarization and (b) the intensity of photoluminescence versus transverse magnetic field for a GaAs$_{0.979}$N$_{0.021}$ film excited at $T = 300$ K by circularly polarized light ($h\nu_{exc} = 1.311$ eV, $h\nu_{det} = 1.159$ eV) with intensities $J = (\bullet)$ 240, $(\square)$ 150, $(\triangledown)$ 100, $(\star)$ 50, and $(\circ)$ 25 mW. Symbols present the experimental data and the solid curves show the Lorentzian approximations $y(B) = y^* + y_0(1 + B^2/B_{1/2}^2)^{-1}$.

the centers with two coupled electrons. As the magnetic field strength is increased, the depolarization of coupled electrons tends to grow, the intensity $I_{circ}$ decreases to $I_{lin}$, and the polarization $\rho$ decreases to $bP_i \equiv \rho^*$.

In order to determine the photoluminescence intensity and polarization in the case of strong pumping, it is necessary to solve a nonlinear system of balance equations. The results of preliminary calculations showed that the SDR model [7] is applicable to the explanation of experimental data obtained in the entire range of $J$ values.

Now we will demonstrate that the system under consideration possesses, besides a short spin relaxation time $\tau_s$, a long characteristic time related to evolution of the spin of free electrons. To this end, let us consider equations for the rates of variation of the electron polar-

ization components, which follow from the balance equations for $n_\pm$ and $N_\pm$:

$$\frac{dP}{dt} = -\frac{P}{\tau_s} + \frac{P_c}{\tau_0}(1 - P^2) + \frac{G}{n}(P_i - P), \qquad (3)$$

$$\frac{dP_c}{dt} = -\frac{P_c}{T_{sc}} + \frac{n}{N}\frac{1}{\tau_0}P(1 - P_c^2), \qquad (4)$$

where $\tau_0^{-1} = \gamma_e N/2$. The second term in the right-hand part of Eq. (3), which is related to the SDR, plays the role of a spin generator. Indeed, the polarization kinetics $P(t)$ upon switching off the stationary optical pumping ($G = 0$) includes fast and slow components: the former decaying for a time on the order of $\tau_s$, and the latter, changing approximately as $P(t) \approx (\tau_s/\tau_0)P_c(t)$.

The fact that the maximum value (35%) of the photoluminescence polarization in Fig. 2a is quite close to the limit (50%) is indicative of a rather long spin memory of conduction electrons. At the same time, as was established above, the spin memory of the nonlinearly related spin subsystems of the free and localized electrons is determined by the large spin lifetime $T_{sc}$ of the localized electrons. The latter value can be readily determined using the Hanle effect, since $B_{1/2} = \hbar/g_c\mu_B T_{sc}$, which implies that $T_{sc}$ increases with decreasing $B_{1/2}$. The minimum halfwidth of the Hanle curve determined from Fig. 2a is $B_{1/2}^{\min} = 91 \pm 5$ G. Taking into account that $\tau_{sc}^{-1} < T_{sc}^{-1}$, we obtain an estimate from below for the product of spin relaxation time and $g$-factor: $g_c\tau_{sc} > g_c T_{sc}^{\min} = 1.3 \pm 0.2$ ns. The value of $g_c$ for GaAsN is unknown (we know of the investigation of $g$ in nitrogen-containing solid solutions based on GaAs [10] that was devoted to the measurement of the $g$ factor of free electrons in GaInAsN). We performed a special experiment with oblique light incidence onto the sample, whereby the photoluminescence was measured in the reflection mode at an angle relative to the exciting light beam, in the presence of a magnetic field oriented perpendicularly to the excitation and detection directions [11]. From the asymmetry of the Hanle effect observed under these conditions, it was established that $g_c > 0$. In the same way, $g_c$ was found to be positive in GaAs$_{1-x}$N$_x$ films with $x = 2.7$ and 3.4%. This sign of $g_c$ suggests that its value is close to the $g$-factor of free electron in vacuum ($g_c \approx 2$). From this, we infer that $\tau_{sc} > 0.6$ ns.

In conclusion, GaAsN solid solutions exhibit a strong room-temperature SDR. The giant lifetimes and the magnitude of polarization of the spin of conduction electrons observed under the conditions of optical pumping make nitrogen-containing GaAs-based compounds promising materials for spintronics. The circular polarization of photoluminescence and the half-width of the Hanle curve in the intrinsic semiconductor under consideration are strongly dependent on the intensity of exciting light. The obtained experimental data were interpreted in terms of the SDR model [7]. This model adequately explains the dependence of the photoluminescence lifetime, the spin lifetime, and the degree of the electron spin orientation on the pumping intensity. Despite a very short time of the spin relaxation of free electrons, the system of free and localized charge carriers is also characterized by slow spin relaxation with a characteristic time on the order of 1 ns. Using the Hanle effect, it was established that the $g$ factor of electrons localized on deep paramagnetic centers responsible for the SDR is positive.

## REFERENCES

1. M. Kondow, T. Kitatani, S. Nakatsuka, *et al.*, IEEE J. Sel. Top. Quantum Electron. **3**, 719 (1997).

2. W. Walukiewicz, Physica E (Amsterdam) **20**, 300 (2004).

3. A. Yu. Egorov, V. K. Kalevich, M. M. Afanasiev, *et al.*, J. Appl. Phys. **98**, 013539 (2005).

4. *Optical Orientation*, Ed. by F. Meier and B. P. Zacharchenya (North-Holland, Amsterdam, 1984; Nauka, Leningrad, 1989).

5. V. D. Kul'kov and V. K. Kalevich, Prib. Tekh. Éksp., No. 5, 196 (1980).

6. V. K. Kalevich, M. Ikezawa, A. Yu. Shiryaev, *et al.*, in *Proceedings of 11th International Symposium on Nanostructures: Physics and Technology* (St. Petersburg, Russia, 2003), p. 277.

7. C. Weisbuch and G. Lampel, Solid State Commun. **14**, 141 (1974).

8. R. C. Miller, W. T. Tsang, and W. A. Nordland, Jr., Phys. Rev. B **21**, 1569 (1980).

9. D. Paget, Phys. Rev. B **30**, 931 (1984).

10. C. Skierbiszewski, P. Pfeffer, and J. Lusakowski, Phys. Rev. B **71**, 205 203 (2005).

11. V. K. Kalevich, B. P. Zakharchenya, and O. M. Fedorova, Fiz. Tverd. Tela (St. Petersburg) **39**, 768 (1997) [Phys. Solid State **39**, 681 (1997)].

*Translated by P. Pozdeev*

# Generation of a Two-Photon KLM Quantum Channel¶

## S. A. Podoshvedov

*School of Computational Sciences, Korea Institute for Advanced Study, Seoul, 130-722 South Korea*
*e-mail: sap@kias.re.kr*
Received July 27, 2005

As demonstrated by E. Knill *et al.* [Nature **409**, 46 (2001)], quantum teleportation and quantum logic gates with a success probability close to one can be implemented using only linear optical elements, additional photons, and post-selection. To do this, it is desirable to have special quantum channels in sight before quantum teleportation performance. Here, we propose an experimental arrangement to generate a two-photon KLM state different from the well-known Bell states. This two-photon KLM state can be used to enhance the success probability of the quantum teleportation of a one-mode quantum qubit from 0.5 up to 2/3. © *2005 Pleiades Publishing, Inc.*

PACS numbers: 03.67.Lx

The theory of quantum computation promises to revolutionize the future of computer technology in factoring large integers [1] and combinational searches [2]. For quantum communication purposes, entangled states of light fields are of particular interest. Such states can also be used, for example, for quantum key distribution [3] and quantum teleportation [4]. The entangled states are useful for quantum processing, but they are hard to produce and the states tend to decohere fast. A spontaneous noncollinear parametric down-converter with type-II phase matching is considered to produce true two-photon entanglement (a maximally entangled Bell state or Einstein–Podolsky–Rosen (EPR) pair) along certain directions of propagation of the generated optical beams [5]. One should mention that such EPR states make it possible to observe, for example, the process of quantum teleportation with a probability of success of 50% [6]. The problem is that nonlinear interactions between individual photons are required to implement a quantum teleportation protocol that operates with 100% efficiency [7]. In order words, inherently nonlinear Bell state measurement must be performed for achievement of 100% teleportation [8].

Nevertheless, it was recently found that the success probability of quantum teleportation, as well as controlled sign gates, can be increased to close to one by increasing the number of ancillary optical modes, photons, and beam splitters [9]. To do this, special quantum channels, which we call KLM (E. Knill, R. Laflamme, G.J. Milburn) channels, must be prepared beforehand. The optical qubit interacts with the KLM quantum channel by passing through a network of beam splitters and phase shifters [9]. Depending on the measurement result in ancillary modes [10], quantum teleportation can be performed with a success probability of more

than 50% [9]. In the paper, we propose a method to generate a two-photon KLM state

$$|\Psi_{KLM}^{(1234)}\rangle = \frac{1}{\sqrt{3}}\{|1100\rangle + |1001\rangle + |0011\rangle\}_{1234}, \quad (1)$$

where, henceforth, the numbers in the subscripts of the used states are related to the optical modes of the photons [11]. For example, the state $|1100\rangle_{1234}$ in Eq. (1) is a tensor product of one-photon number states where the modes are occupied by two photons, while modes 1 and 2 have zero photons.

To generate two-photon KLM state (1), we are going to make use of an induced parametric down-converter with type-I phase matching (IPDCI) with one
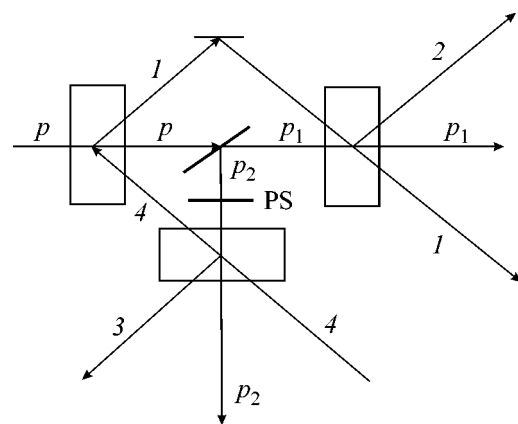


Experimental setup to produce a two-photon KLM state consisting of three coupled SPDCI. PS means phase shifter.

---

¶ The text was submitted by the author in English.

input signal photon to the noncollinear spontaneous parametric down-converter with type-I phase matching (SPDCI). For our purposes, we use the experimental setup shown in the figure. First, let us consider SPDCI in detail. We are going to describe the SPDCI as well as IPDCI by the simplified three-mode Hamiltonian [12]

$$H_1 = \frac{i\hbar r}{2}(\hat{a}_1^+\hat{a}_2^+\hat{a}_p - \hat{a}_p^+\hat{a}_2\hat{a}_1), \qquad (2)$$

where $\hat{a}_1$ and $\hat{a}_2$ are the modes of down-converted photons, the operator $\hat{a}_p$ is the mode of the powerful beam pumping simultaneously first and second down-converted crystals through the balanced beam splitter as shown in the figure, and the coupling coefficient $r$ is related to the nonlinear second-order susceptibility tensor $\chi^{(2)}$. The simplified three-mode Hamiltonian of the noncollinear SPDCI is applicable in the case of continuous wave pumping when we neglect the multifrequency structure of the pump and use narrowband filters to choose only modes satisfying the phase-matching condition. According to [12], the output function of the SPDCI with input state $|00\rangle_{12}|\alpha\rangle_p$ is given by

$$|\Psi_S^{(12)}\rangle = \sum_{n=0}^{\infty}(\alpha\beta)^n|n_1\rangle_1|n\rangle_2|\psi_{(00)}^{(n)}\rangle_p, \qquad (3a)$$

where the partial wave functions $|\psi_{(00)}^{(n)}\rangle_p$ in the pumping mode are given by

$$|\psi_{(00)}^{(n)}\rangle_p = \exp\left(-\frac{|\alpha|^2}{2}\right)\sum_{m=0}^{\infty}\frac{\alpha^m f_{n+1}^{(2(m+n))}(\beta)}{\beta^n\sqrt{(m+n)!}}|m\rangle_p, \quad (3b)$$

where the function $f_{n+1}^{(2(m+n))}(\beta)$ is responsible for the output wave amplitude [12], the subscript (00) in the definition of the functions $|\psi_{(00)}^{(n)}\rangle_p$ means the input states in the signal and idler modes were in vacuum, and the superscript in the designation of the output function $|\Psi_S^{(12)}\rangle$ of the SPDCI concerns the numbers of the generated modes. Here, the magnitude $\alpha$ is the amplitude of the coherent state input to the SPDCI and the coefficient $\beta$ is responsible for the "strength" of the SPDCI [12]. The output nonnormalized wave function of the SPDCI (3b) can be significantly simplified if we make use of the $\alpha\beta \ll 1$ approximation that takes place in practice and decompose the output wave amplitudes $f_{n+1}^{(2(m+n))}(\beta)$ (Eq. (3b)) into asymptotic series in small parameter $\beta \ll 1$ to take into account only the first term of the series $f_1^{(2n)}(\beta) \sim 1$, $f_2^{(2n)}(\beta) \sim \beta\sqrt{n}$, $f_3^{(2n)}(\beta) \sim \beta^2\sqrt{n(n-1)}$,

..., $f_m^{(2n)}(\beta) \approx \beta^{m-1}\sqrt{n(n-1)\ldots(n-m+2)}$, and so on for any $m \le n+1$ [12]

$$|\Psi_S^{(12)}\rangle = \sum_{n=0}^{\infty}(\alpha\beta)^n|n\rangle_1|n\rangle_2|\alpha\rangle_p. \qquad (3c)$$

Now let us consider IPDCI with one input signal photon and no photons in the idler mode, in other words, if the input conditions to Hamiltonian $H_1$ (Eq. (2)) are chosen, for example, as $|10\rangle_{12}|\alpha\rangle_p$. Following the same technique as in the case of SPDCI [12], we can write the wave function of the IPDCI as

$$|\Psi_I^{(12)}\rangle = \sum_{n=0}^{\infty}|\Psi_{(10)}^{(2n+1)}\rangle, \qquad (4a)$$

where

$$|\Psi_{(10)}^{(2n+1)}\rangle = \sum_{k=1}^{n+1}f_{k(10)}^{(2n+1)}(s;\beta)|k\rangle_1|k-1\rangle_2|n-k+1\rangle_p, (4b)$$

with the wave amplitudes $f_{k(10)}^{(2n+1)}(s;\beta)$ ($k = 1, \ldots, n+1$) satisfying the set of linear differential equations

$$\frac{df_{k(10)}^{(2n+1)}}{ds} = \beta(\sqrt{k(k-1)(n-k+2)}f_{k-1(10)}^{(2n+1)} \\ - \sqrt{k(k+1)(n-k+1)}f_{k+1(10)}^{(2n+1)}. \qquad (4c)$$

The following input conditions $f_{1(10)}^{(2n)}(s=0) = \exp(-|\alpha|^2/2)\alpha^n/\sqrt{n}!$ and $f_{k(10)}^{(2n)}(s=0) = 0$ for $k = 2, \ldots, n+1$ are imposed on Eq. (4c). Here, the symbol in the subscripts of the Eqs. (4a–4e) is introduced to distinguish the states (4a–4c) from the states (3a and 3b). The output wave function of the EPDCI $|\Psi_I^{(12)}\rangle$ (Eq. (4a)) can be rewritten as

$$|\Psi_I^{(12)}\rangle = \sum_{n=0}^{\infty}(\alpha\beta)^n|n\rangle_1|n\rangle_2|\psi_{10}^{(n)}\rangle_p, \qquad (4d)$$

where the partial wave functions $|\psi_{(10)}^{(n)}\rangle_p$ in the pumping mode are given by

$$|\psi_{(10)}^{(n)}\rangle_p = \exp\left(-\frac{|\alpha|^2}{2}\right)\sum_{m=0}^{\infty}\frac{\alpha^m f_{n+1(10)}^{(2(m+n)+1)}(\beta)}{\beta^n\sqrt{(m+n)!}}|m\rangle_p. \quad (4e)$$

The smallness of the parameter $\beta \ll 1$ allows one to decompose the wave amplitudes $f_{k(10)}^{(2(m+n)+1)}(\beta)$ into asymptotic series in the small parameter $\beta$ restricting the decomposition only to the first term in the case of $\beta \ll 1$. Then, we get $f_{n+1(10)}^{(2(n+m)+1)} \sim$

$\beta^n \sqrt{n+1} \sqrt{(n+m)(n+m-1)\ldots(m+1)}$ and the output wave function of the IPDCI with one input signal photon in the $\alpha\beta \ll 1$ approximation is given by

$$|\Psi_I^{(12)}\rangle = \sum_{n=0}^{\infty} (\alpha\beta)^n \sqrt{n+1}|n+1\rangle_1|n\rangle_2|\alpha\rangle_p. \qquad (4f)$$

Now we are ready to describe in more detail the experimental setup in the figure to produce the two-photon KLM state. First, SPDCI produces the outcomes given by Eqs. (3a–3c). We are going to make use of the $\alpha\beta \ll 1$ approximation valid in the practical case to deal with only the following nonnormalized wave function $|\tilde{\Psi}_{in}\rangle = \{|00\rangle + \alpha\beta|11\rangle\}_{12}|\alpha\rangle_p$ (input to system of two coupled IPDCI in figure) neglecting the higher order terms in the parameter $\alpha\beta \ll 1$ in the output wave function of the SPDCI (Eq. (3c)). The next step is related to the system of two down-converted crystals with identical responses pumped simultaneously by powerful pumping modes, as shown in the figure. According to the figure, the pumping mode in a coherent state with amplitude $\alpha$ ($|\alpha\rangle_p$) passes through a balanced beam splitter, transforming to the state $|\alpha/\sqrt{2}\rangle_{p_1}|i\alpha/\sqrt{2}\rangle_{p_2}$, where the subscripts $p_1$ and $p_2$ refer to the first and second output modes of the beam splitter, respectively. We apply a phase shifter to avoid a $\pi/2$ phase shift in the second pumping mode $\pi_2$. The phase-shifter is an optical element that acts on a single mode to cause a shift $\psi$ in the phase of the mode state. The underlying unitary evolution operator is $\hat{P}_{p_2} = \exp(-\phi\hat{a}_{p_2}^+\hat{a}_{p_2})$. Then, we have the relation $\hat{P}_{p_2}\hat{a}_{p_2}^+\hat{P}_{p_2}^+ = \exp(-i\phi)\hat{a}_{p_2}^+$, which enables one to remove the $\pi/2$ phase shift in the second pumping mode $p_2$ if we chose $\phi = \pi/2$. One of the modes generated by the SPDCI (namely, mode 1) is launched into the first down-converted crystal, while the other mode (namely, mode 2, which we label as 4 in the figure) is entered into the second down-converted crystal. Finally, the input state to the two down-converted crystals becomes $|\Psi_{in}\rangle = \{|0000\rangle + \alpha\beta|1001\rangle\}_{1234}|\alpha/\sqrt{2}\rangle_{p_1}|\alpha/\sqrt{2}\rangle_{p_2}$ after the beam splitter.

As a consequence of such an input to the down-converters, the outcome of the system is divided into two groups, namely, one part of the state $|\Psi_{in}\rangle$ originating from the input state $|0000\rangle_{1234}|\alpha/\sqrt{2}\rangle_{p_1}|\alpha/\sqrt{2}\rangle_{p_2}$ gives rise to the SPDCI process and the other part of the input state $|\Psi_{in}\rangle$, namely, $\alpha\beta|1001\rangle_{1234}|\alpha/\sqrt{2}\rangle_{p_1}|\alpha/\sqrt{2}\rangle_{p_2}$, is responsible for the IPDCI.

We make use of the three-mode simplified Hamiltonian $H_{12}$ for the system of two down-converted crystals with identical responses pumped simultaneously by powerful pump modes

$$H_{12} = H_1 + H_2$$
$$= \frac{i\hbar r'}{2}(\hat{a}_1^+\hat{a}_2^+\hat{a}_{p_1}^+ - \hat{a}_{p_1}^+\hat{a}_2\hat{a}_1 + \hat{a}_3^+\hat{a}_4^+\hat{a}_{p_1}^+ - \hat{a}_{p_1}^+\hat{a}_4\hat{a}_3), \qquad (5)$$

where the subscripts for quantum operators in (5) refer to the corresponding signal, idler (modes 1–4), and pump modes (modes $p_1$ and $p_2$); the coupling constant $r'$ is related to the system of coupled down converters; and the Hamiltonians $H_1$ and $H_2$ relate to the first and second down-converters in the figure, respectively. The Hamiltonian $H_{12}$ (5) gives rise to the following wave function:

$$|\Psi_{out}\rangle = |\Psi_S^{(12)}\rangle|\Psi_S^{(34)}\rangle + \alpha\beta|\Psi_I^{(12)}\rangle|\Psi_I^{(34)}\rangle, \qquad (6)$$

with the corresponding wave functions $|\Psi_S^{(12)}\rangle$ and $|\Psi_I^{(12)}\rangle$ (Eqs. (3a) and (3b), (4d) and (4f)) in the first and second output ports and the states $|\Psi_S^{(34)}\rangle$ and $|\Psi_I^{(34)}\rangle$ in the third and fourth output channels, respectively. The fact that the parameter $\alpha\beta$ in the practical case takes a value of much less than one ($\alpha\beta \ll 1$) makes it possible to rewrite the output wave function taking into account only vacuum states and terms proportional to the factor $\alpha\beta$ as

$$|\Psi_{out}\rangle = \{|0000\rangle + \alpha\beta'/\sqrt{2}(|1100\rangle + |0011\rangle)$$
$$+ \alpha\beta|1001\rangle\}_{1234}|\alpha/\sqrt{2}\rangle_{p_1}|\alpha/\sqrt{2}\rangle_{p_2}. \qquad (7)$$

Here, the parameter $\beta'$ is related to the coupling constant of the system of two SPDCI pumped simultaneously through the balanced beam splitter. Finally, we get superposition of the vacuum state with two-photon KLM state (1) (Eq. (7)) if we take $\beta' = \sqrt{2}\beta$. One should mention that the proposed experiment is based on the use of coupled IPDCI, which is inherently random. Consequently, we can determine whether a pair of photons has been generated only by postselection produced by detectors. The same random generation of the superposition of the vacuum and Bell states occurs in the majority of current experiments [5, 6], when the randomness of the generated pair is not essential. The scheme proposed in the figure can become the basis for generation of other types of KLM states, for example, the four-photon KLM state $|rt_2\rangle = \sum_{j=0}^{2}|\tilde{0}\rangle^j|\tilde{1}\rangle^{2-j}|\tilde{0}\rangle^{2-j}|\tilde{1}\rangle^j$ written in terms of the qubit encoding [9] by use of the quantum encoding technique. The state $|rt_2\rangle$ can be used to teleport a two-mode qubit with a success probability of 2/3 [9].

## REFERENCES

1. P. W. Shor, SIAM J. Comput. **26**, 1484 (1997).

2. L. K. Grover, Phys. Rev. Lett. **79**, 325 (1997).

3. A. Ekert, Phys. Rev. Lett. **67**, 661 (1991).

4. C. Bennett, G. Brassard, C. Crepeau, *et al.*, Phys. Rev. Lett. **70**, 1895 (1993).

5. P. G. Kwiat, K. Mattle, H. Weinfurter, *et al.*, Phys. Rev. Lett. **75**, 4337 (1995); P. G. Kwiat *et al.*, Phys. Rev. A **60**, R773 (1999).

6. D. Bouwmeester, J. W. Pan, K. Mattle, *et al.*, Nature **390**, 575 (1997); D. Boschi, S. Branca, F. De Martini, *et al.*, Phys. Rev. Lett. **80**, 1121 (1998).

7. L. Vaidman and N. Yoran, Phys. Rev. A **59**, 116 (1999); N. Lutkenhaus, J. Calsamiglia, and K. A. Suominen, Phys. Rev. A **59**, 3295 (1999).

8. Y. H. Kim, S. P. Kulik, and Y. H. Shih, Phys. Rev. Lett. **86**, 1370 (2001).

9. E. Knill, R. Laflamme, and G. J. Milburn, Nature **409**, 46 (2001).

10. D. Gottesman and I. L. Chuang, Nature **402**, 390 (1999).

11. M. Nielsen and I. L. Chuang, *Quantum Computation and Quantum Information* (Cambridge Univ. Press, Cambridge, 2000).

12. S. A. Podoshvedov, J. W. Noh, and K. S. Kim, Opt. Commun. **221**, 121 (2003); Opt. Commun. **232**, 357 (2004).